공학박사학위논문

개선된 전기동력 모델링을 이용한 eVTOL 시스템의 범용적 설계기법 제안

Generic System Design Methodology for eVTOL Aircraft using Enhanced Electric Propulsion Modeling

2023 년 2 월

서울대학교 대학원

항공우주공학과

이 동 욱

개선된 전기동력 모델링을 이용한 eVTOL 시스템의 범용적 설계기법 제안

Generic System Design Methodology for eVTOL Aircraft using Enhanced Electric Propulsion Modeling

지도교수 이 관 중

이 논문을 공학박사 학위논문으로 제출함

2022 년 11 월

서울대학교 대학원

항공우주공학과

이 동 욱

이동욱의 공학박사 학위논문을 인준함

2022 년 12 월

위 원 장 : ____________________

부위원장 : ____________________

위 원 : ____________________

위 원 : ____________________

위 원 : ____________________

Abstract

Generic System Design Methodology for eVTOL Aircraft using Enhanced Electric Propulsion Modeling

Donguk Lee
Department of Aerospace Engineering
The Graduate School
Seoul National University

In recent years, various technological advances in electrification, automation, and vertical takeoff and landing (VTOL) have matured enough to enable innovation in urban aviation, resulting in the emergence of a new air transportation system known as advanced air mobility (AAM). VTOL aircraft for AAM is powered by an electric propulsion system, which provides new design freedom for the configuration and flight mechanism. To design the eVTOL aircraft for AAM, therefore, it is necessary to have generality rather than being limited to a specific concept. In addition, since eVTOL aircraft for AAM services between the intracity and intercity, the noise generated by the rotary-wing system should be considered a performance indicator for the eVTOL aircraft design.

Meanwhile, due to the low specific energy of the current battery technology, the range of most full-EPS (FEPS) powered VTOL aircraft has been so far restricted to intracity operation. However, as the battery technology matures, VTOL aircraft for

AAM will likely use a FEPS powered only by batteries. This requires sophisticated EPS modeling techniques to consider the electrical characteristics of each electrical device in a more accurate manner.

To this end, this study proposes a generic design methodology that considers eVTOL AAM vehicles' characteristics. This design methodology comprises five modules (flight analysis, propulsion system sizing, mission analysis, weight estimation, and noise prediction) that can consider the diversity of configurations, flight mechanisms, EPS architectures, and performance assessment, including noise prediction. First, the comprehensive flight-analysis module is created by assembling component-analysis methods, including the shrouded rotor and distributed propulsor (DP). The proposed technique allows for analysis of the configurations and flight mechanisms of various types of VTOL aircraft—wingless, vectored-thrust, and lift+cruise. In addition, the scope of propulsion system sizing, mission analysis, and weight estimation has been expanded to include not only FEPS but also various Hybrid-EPSs (series, parallel, and series-parallel). Using the Farassat 1A formulation with compact loading models, it is possible to predict the thickness and load noise of eVTOL aircraft at the conceptual design stage.

Also, this study proposes novel enhancements to the EPS modeling approach for FEPS-powered VTOL aircraft conceptual design by considering the electrical characteristics of each electrical device in a more accurate manner. To this end, three modules for motor, inverter, and battery analysis are constructed using equivalent circuits and semi-empirical models. First, the motor analysis module is developed using equivalent circuit analysis with the operation control strategy for a permanent-magnet synchronous motor. Second, the inverter analysis module is built using average loss models for the switching and conduction losses. Third, the battery

analysis module is improved using the near-linear discharge model to consider the voltage drop during operation. Moreover, additional modules, such as those for calculating the battery stack in series and parallel, as well as regression models for the motor and inverter parameters and consideration of the drive system type (direct or indirect, including a reduction gear), are implemented.

In addition, three types of applications are performed to demonstrate the necessity and capability of the proposed numerical methods for eVTOL conceptual design. In the first application, a comparative study is performed to demonstrate performance variations after replacing a FEPS with a HEPS; it is shown that HEPS with an optimal hybridization ratio has overwhelming superiority regarding payload capacity and mission range over FEPS based on the current battery technology level. In the second application, it is confirmed that changes in the type of drive system (direct or indirect) and gear ratio significantly impacted EPSs' efficiency and size, which can only be considered in the enhanced EPS approach. Lastly, the final application is to investigate the influence of noise prediction on the design optimization of an eVTOL aircraft. It is identified that there is a tradeoff relationship between noise mitigation and gross weight minimization depending on the rotor's torque and rotational speed.

Keywords: Advanced Air Mobility, Electric Vertical Takeoff and Landing Aircraft, Electric Propulsion System Modeling, Conceptual Design, Design Optimization
Student Number: 2019-34016

Table of Contents

Nomenclature

Symbols

A	disk area, m^2
b	wingspan, m
C	total capacity, Ah
C_1–C_2	empirical coefficients for IC engine fuel flow rate
C_3	IC engine lapse rate
C_4–C_5	empirical coefficients for IC engine lapse rate
C_{l}	lift coefficient (2D)
C_{l_α}	slope of lift curve (2D)
C_{d}	drag coefficient (2D)
Cr	C-rate, 1/h
c	chord length, m
c	speed of sound, m/s
D	drag, N
D_{rod}	diameter of a supporting rod, m
DD	depth of discharge
E	required energy, kW·h
E_{off}	turn-off energy, mJ
E_{on}	turn-on energy, mJ
F	Prandtl's tip loss function
f_{e}	equivalent flat plate area, m^2
f_{sw}	switching frequency, kHz
G	change in the slope of the discharge curve due to current
H_{t}	thruster drag force in the disk plane, N
h	maximum thickness of the airfoil, m
I_{c}	indicator function for the battery charge
I_{cn}	nominal continuous collector current, A
$I_{d,q}$	d- and q-axis currents of the PMSM, A
I_{ref}	reference current (on-state current after commutation), A
I_{mot}	magnitude of PMSM current vector, A

I_{zz}	moment of inertia with respect to the z-axis, mm^4
K	primary dependence of voltage on discharged capacity
L	lift force, N
L	local force vector, N
L_A	A-weighted overall sound pressure level, dBA
$L_{d,q}$	d- and q-axis inductances of the PMSM, μH
LS	lift-sharing ratio
l_{rod}	length of a supporting rod, m
M	Mach number
M	modulation index
N_{b}	number of blades
$N_{\mathrm{cell,series}}$	number of battery cells in series
$N_{\mathrm{cell,parallel}}$	number of battery cells in parallel
N_{IGBT}	number of IGBTs
N_{p}	number of pole pairs in the PMSM
N_{t}	number of thrusters
P	power, kW
P_{c}	battery-charging power, kW
P_{cell}	output power of battery cell, kW
P_{cond}	conduction loss, kW
P_{Cu}	copper loss, kW
P_{eng}	engine power, kW
P_{Fe}	iron loss, kW
P_{HB}	power obtained from battery, kW
P_{HF}	power obtained from hydrocarbon fuel, kW
P_{loss}	power loss, kW
P_{IRP}	intermediate rated power, kW
P_{MCP}	maximum continuous power, kW
P_{mech}	mechanical power, kW
P_{total}	total required power for the aircraft, kW
$P_{\text{no-load}}$	no-load power, kW
P_{sw}	switching loss, kW
Pb	ratio of the package burden

Q	capacity discharged to the present, Ah
Q_{end}	capacity discharged until the end of the mission, Ah
R	radius, m
R	internal resistance, Ω
R_{ce}	IGBT differential resistance, Ω
R_{F}	diode differential resistance, Ω
r	nondimensional radial span position
r	distance between the observer and the source
S	wing area, m^2
S_{blown}	wing area blown by the propeller wake, m^2
T	thrust, N
T_{vj}	virtual junction temperature of the semiconductor, °C
t	time, h
V	velocity, m/s
V_{ce0}	IGBT threshold voltage, V
$V_{\mathrm{cell,0}}$	open-circuit cell voltage, V
V_{ces}	collector–emitter voltage, V
V_{DC}	DC link voltage, V
$V_{d,q}$	d- and q-axis voltages of the PMSM, V
V_{F0}	diode threshold voltage, V
V_{mot}	magnitude of PMSM voltage vector, V
V_{ref}	reference voltage (blocking-state voltage of the IGBT before commutation), V
V_{tip}	velocity at the thruster tip, m/s
v_{i}	induced velocity, m/s
W	aircraft load, kg
W	weight, kg
W_{empty}	aircraft empty weight, kg
W_{fuel}	fuel weight, kg
$\dot{W}_{\mathrm{fuel}}$	fuel flow rate to internal combustion engine, kg/h
W_{payload}	payload weight, kg
α	angle of attack, rad
β	velocity multiplier

β	phase angle, rad
γ_{g}	reduction gear ratio
δ_{alt}	ratio of atmospheric pressure at an altitude to standard day sea-level pressure
ξ	percentage of engine power supplied to accessory items
η	efficiency coefficient
η_{safe}	safety factor
θ	collective pitch angle, rad
θ_{alt}	ratio of ambient temperature at an altitude to standard day sea-level temperature
θ_{i}	incidence angle, rad
κ_{heat}	margin to account for the excess heat
$\mathit{\Lambda}$	sweep angle, rad
λ	inflow velocity ratio
λ_0	permanent magnet flux linkage, Vs
λ_{c}	climbing velocity ratio
λ_{relax}	relaxation factor
λ_{w}	taper ratio of the wing
ρ	air density, kg/m^3
σ	thruster solidity
σ_{allow}	allowable stress, Pa
σ_{d}	expansion ratio
σ_{max}	maximum stress, Pa
σ_{yield}	yield stress, Pa
τ	torque, Nm
τ_{em}	electromagnetic torque, Nm
τ_{mech}	mechanical torque, Nm
φ	power control ratio for the IC engine
φ	power factor angle, rad
ϕ	induced angle of attack
χ	technical factor
ω_{b}	base speed, rad/s
ω_{e}	electrical rotational speed, rad/s

ω_{mech}	mechanical rotational speed, rad/s

Subscripts

avail	available
bat	battery
c	cruise
cell	battery cell
comp	component
cr	continuous rated
CSTR	design constraint
eng	IC engine
g	reduction gear
gb	gearbox
ht	horizontal tail wing
inv	inverter
l	lift
max	maximum value
MG	motor-generator
mot	motor
rect	rectifier
req	required
ret	evaluation of the integrals at retarded time
RMS	root mean square
t	thruster
tm	motor-driven thruster
ts	shaft-driven thruster
vt	vertical tail wing
w	main wing
∞	free stream

Abbreviations

AAM	Advanced Air Mobility
AC	Alternating Current
ACARE	Advisory Council for Aeronautics Research in Europe
BEMT	Blade Element Momentum Theory
BET	Blade Element Theory
DC	Direct Current
DP	Distributed Propulsor
DOH	Degree of Hybridization
EPS	Electric Propulsion System
eVTOL	Electric-Vertical Takeoff and Landing
FEPS	Full-Electric Propulsion System
HEPS	Hybrid-Electric Propulsion System
IGBT	Insulated Gate Bipolar Transistor
LL	Lift Line Theory
OASPL	A-weighted Overall Sound Pressure Level
MTOW	Maximum Takeoff Gross Weight
MTPA	Maximum Torque Per Ampere
NDARC	NASA Design and Analysis of Rotorcraft
PMSM	Permanent Magnet Synchronous Motor
RISPECT+	Rotorcraft Initial Sizing and Performance Estimation Code and Toolkit+
TMS	Thermal Management System
VTOL	Vertical Takeoff and Landing

List of Figures

List of Tables

Chapter 1.

Introduction

1.1 Overview of eVTOL aircraft

The air transport industry has doubled in size every fifteen to twenty years since the introduction of jet engines, recording the fastest-growing transport sector [1]. Although a similar growth rate is expected in the future, this increase in aircraft traffic has made the aviation industry face challenges related to greenhouse gas emissions and noise pollution. Approximately 859 million tonnes of CO_2 were emitted by airlines in 2017. This represents 2 % of the global human emissions of around 40 billion tonnes [2]. With no intervention by 2050, emissions from the aviation industry are projected to increase by 300-700 % [3]. Accordingly, international aviation organizations aim to achieve carbon-neutral growth from 2020 and to reduce their emissions by 50 % compared to 2005 levels by 2050 [4]. ACARE (Advisory Council for Aeronautics Research in Europe) has set goals by 2050 of a 75% reduction in CO_2 emissions, a 90% reduction in NO_x emissions, and a 65% reduction in noise levels as compared to 2000 levels.[i] Also, NASA has set goals to address these issues, and its N+3 goal is to reduce fuel combustion by 60%, NO_x emissions by 80%, and noise by 71 dB compared to 2005 levels [5]. Other

[i]Data available online at https://www.acare4europe.org/acare-goals/ [retrieved 10 October 2022].

technology programs such as CLEEN in USA, GARDN in Canada, and Clean Sky 2 Joint Technology Initiative in EU have been established to achieve these and similar goals [1]. Therefore, to meet these programs' goals, the concept of an electric propulsion system (EPS) has been introduced to the aviation industry.

In addition to aircraft electrification, various mature technological advances in automation and vertical takeoff and landing (VTOL) have enabled innovation in urban aviation, including new aircraft designs, services, and business models [6, 7]. These new trends are driving the development of an air transportation system, namely, advanced air mobility (AAM),[ii] which aims to transport people and cargo between places previously unserved or underserved by aviation [8, 9]. As stated in an AAM market report,[iii] AAM vehicles for both intercity and intracity operations possess a very high market potential. The AAM market is projected to grow from US$2.6 billion in 2022 to US$28.3 billion by 2030 at a compound annual growth rate (CAGR) of 34.3 % from 2025 to 2030. Furthermore, Morgan Stanley's new report[iv] released following the COVID-19 pandemic analyzes that the substantial

---

[ii]Data available online at https://www.nasa.gov/aam/overview/ [retrieved 10 October 2022].

[iii]Data available online at https://www.marketsandmarkets.com/Market-Reports/urban-air-mobility-market-251142860.html [retrieved 10 October 2022].

[iv]Data available online at https://advisor.morganstanley.com/the-busot-group/documents/field/b/bu/busot-group/Electric%20Vehicles.pdf [retrieved 10 October 2022].

financial projections of the global AAM market will reach $9,042 billion by 2050, as shown in Fig. 1-1.

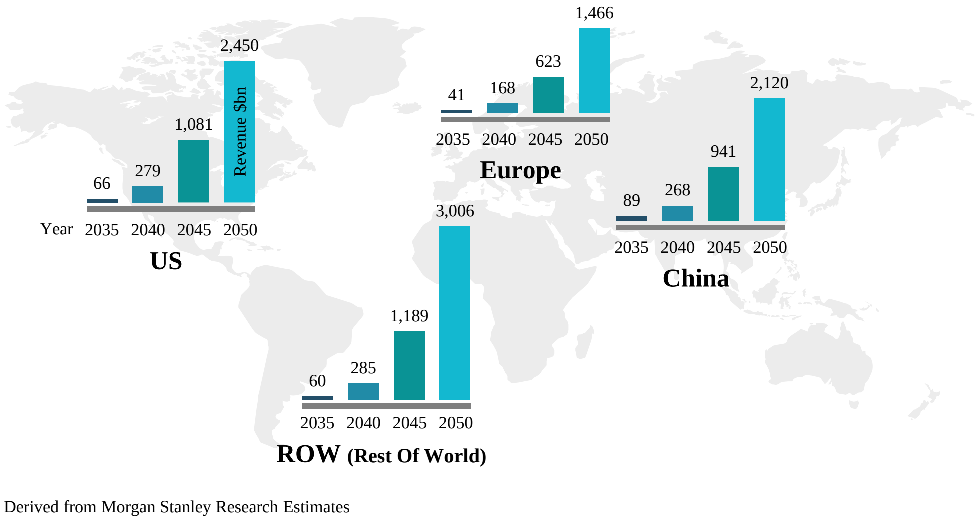

Fig. 1-1 AAM Global total addressable market summary.

It is for this reason that many aircraft manufacturers, as well as start-up companies, have given impetus to develop new eVTOL AAM vehicles.

According to the World eVTOL Aircraft Directory[v], more than 700 electric VTOL (eVTOL) aircraft concepts for AAM have been suggested to date. The eVTOL aircraft concepts for AAM are generally classified into three categories depending on the role of lift-generating and thrust-producing devices:

a) *Wingless type*: the lift and thrust are obtained only by a thruster without a wing or a tilt system.

[v]Data available online at https://evtol.news/aircraft/ [retrieved 10 October 2022].

b) *Lift+cruise type*: two types of thrusters are used that independently generate lift and thrust.

c) *Vectored-thrust type*: the lift and thrust are generated by identical thrusters with a tilt system.

Within the three categories of eVTOL aircraft concepts mentioned above, various configurations and flight mechanisms can be implemented with or without wings, tilting systems, and ducts (Fig. 1-2)

Fig. 1-2 eVTOL wheel of the aircraft [10].

Each concept has a different preferred use case since each concept possesses distinct advantages and disadvantages, as shown in Table 1-1.[vi]

Table 1-1 Comparison of technical characteristics for eVTOL aircraft.[vi]

Aircraft architecture	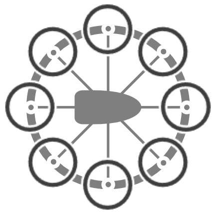 (Wingless)	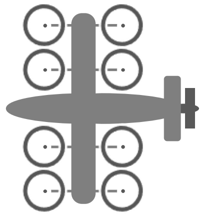 (Lift+cruise)	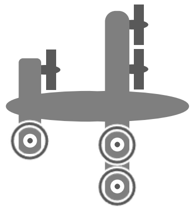 (Vectored-thrust)
Disk loading	Low	Medium	High
Down wash & noise	High	Medium	Low
Gust resistance & Stability	High	Medium	Low
Hovering efficiency	High	Medium	Low
Forward flight efficiency	Low	Medium	High
Preferred use case	Air taxis and intracity	All	Airport shuttles and intercity

As well as these, the preferred use cases of eVTOL aircraft can be classified according to the types of EPS. First, approximately 70% of eVTOL aircraft use a full-electric propulsion system (FEPS), which consists of electric motors, inverters,

[vi]Data available online at https://www.rolandberger.com/publications/publication_pdf/Roland_Berger_Urban_Air_Mobility.pdf [retrieved 10 October 2022].

and batteries. Because a FEPS draws energy solely from batteries, it has the potential to avoid greenhouse gas emissions and fossil fuel use during flight. Although the rate of increase in lithium-ion battery-pack specific energy is typically on the order of 5-8% per year [11], the current specific energy (SE) of a battery is around 120 Wh/kg (pack level), which is approximately 100 times lower than that of hydrocarbon fuel.[vii] Due to this limitation of the battery technology, most FEPS-powered VTOL aircraft focus on intracity air-taxi missions. Propulsion systems for eVTOL aircraft performing intercity missions are primarily based on the hybrid-electric propulsion system (HEPS), which combines electric and mechanical powertrains. The electric powertrain gives greater freedom in the configurational design, and the mechanical powertrain reduces the weight penalty of the battery by using hydrocarbon fuel with the battery. Moreover, if a hybrid-electric aircraft operates with an optimal hybridization ratio between the fuel and the battery, the energy consumption can be further reduced compared to those of solely fuel- or battery-driven aircraft [12–16]. Hence, HEPS-powered VTOL aircraft are not immune from emission issues, but they are considered an appropriate concept for intercity AAM transport.

Therefore, the characteristics of eVTOL aircraft developed so far are summarized as follows:

a) *Configuration*: EPS relieves the mechanical complexity between the drive

[vii]Data available online at https://www.airbus.com/newsroom/stories/airbus-pursues-hybrid-propulsion-solutions-for-future-air-vehicles.html [retrieved 25 October 2022].

system and thruster shaft, providing new design freedom for lift and thrust around the vehicle. This advantage allows for the implementation of various configurations with or without wings, types of thrusters, and distributed propulsors (DPs)—open/shrouded rotor and cruise/lift DP

b) *Flight mechanism*: The eVTOL aircraft operates in three different flight modes (VTOL, transition flight, and cruising) using various flight mechanisms, including thrust vectoring.

c) *EPS architecture*: The propulsion system can not only use FEPS but also use various HEPS types (series, parallel, or series–parallel) depending on the elements that constitute the drivetrain from the energy source to thrusters and how these elements are connected.

In addition, all of these eVTOL aircraft are subject to an inherent limit: noise pollution caused by the rotary-wing system. Constant exposure to this noise may affect numerous adverse effects on citizens [17]. For this reason, national agencies, such as the Federal Aviation Administration (FAA) and the International Civil Aviation Organization (ICAO), have also set stringent noise standards for VTOL aircraft for the local community [18]. Therefore, noise is also a design requirement that should not be overlooked in developing new eVTOL AAM vehicles, along with safety and eco-friendliness.

1.2 Electric devices modeling techniques

When battery technology becomes mature enough, the intercity mission that HEPS is responsible for will be covered by FEPS, thereby achieving zero emissions. As such, since FEPS has a very high potential, it is necessary to develop sophisticated modeling techniques for the components that make up FEPS— electric motors, inverters, and batteries. The FEPS-powered VTOL aircraft for AAM vehicles are operated as shown in Fig. 1-3, and the electrical characteristics of each of the electrical devices are as follows:

a) *Electric motor*: This component converts electrical energy into mechanical energy. Electric motors for drive systems in eVTOL aircraft should possess minimum weight while providing sufficient power for flight. Therefore, permanent-magnet synchronous motors (PMSMs) with their characteristically high efficiency and specific power, are considered the most feasible solution for implementation in eVTOL aircraft propulsion among the various types of motors [19–23]. The efficiency of a PMSM is determined by the voltage, current, and power factor angle (i.e., the phase angle between the current and voltage waveforms) for the mechanical load. Additionally, to reduce the weight and size of the electric motor, a reduction gear/gearbox may be used in the drive system [24, 25].

b) *Inverter*: This device converts the direct current (DC) supplied by the battery into alternating current (AC) and transfers it to the electric motor for propulsion. The power losses of an inverter can be divided into switching and conduction losses, which are determined by the switching transitions and output voltage-current characteristics, respectively.

c) *Battery pack*: This component comprises multiple battery cells connected in both series and parallel to achieve the desired operating voltage and capacity, respectively. An increase in the depth of discharge (DD) of a battery cell causes a voltage drop, accelerating the battery energy consumption by increasing the cell current.

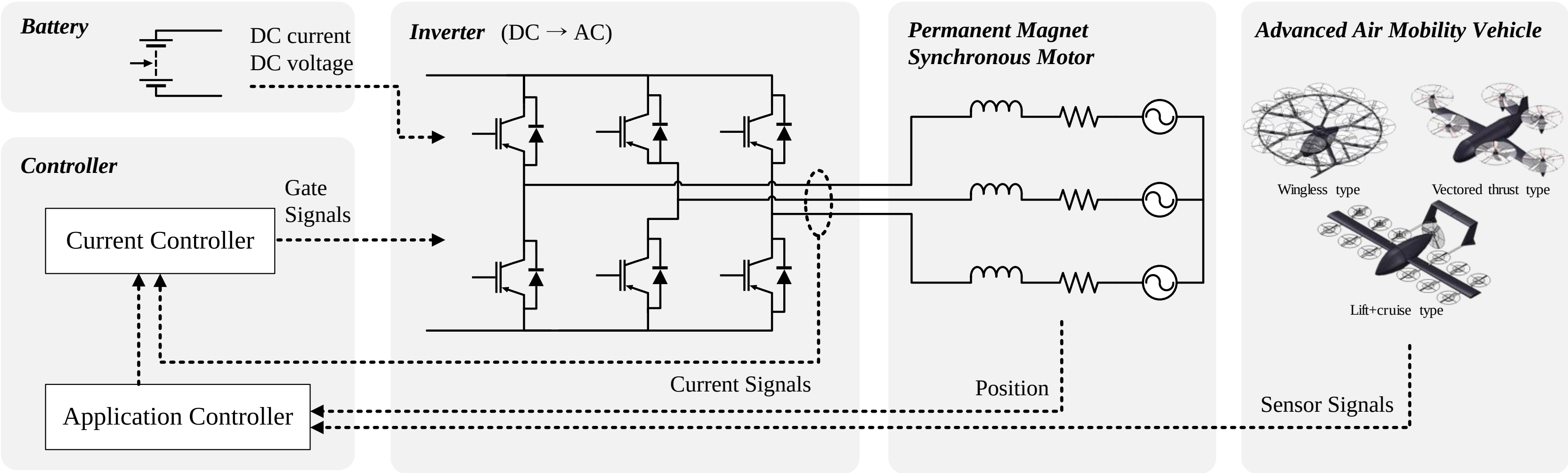

Fig. 1-3 Operation architecture of FEPS-powered VTOL aircraft.

1.3 Research questions

1.3.1 Is it possible to consider the diversity of eVTOL aircraft using conceptual design methods developed thus far?

To explore the successful design of new eVTOL AAM vehicles in advance, it is necessary to consider the distinct characteristics of the eVTOL AAM vehicle in the conceptual design phase—the diversity of configurations, flight mechanisms, and EPS architectures. There have been many studies [12–16, 26–37] on the conceptual design of electrified aircraft so far; however, the proposed conceptual design methods are insufficient to reflect the inherent characteristics of eVTOL AAM vehicles.

First, the studies made a lot of effort to implement EPS into fixed-wing aircraft, such that it became possible to analyze and design electrified fixed-wing aircraft driven by various HEPS as well as FEPS. Pornet et al. [12] reconstructed the thrust table using a hybridization factor and supplemented the fuel-flow table with an energy table to consider the parallel-HEPS. Friedrich et al. [26] constructed the conceptual design process for the hybrid-electric aircraft using the experimental derivation of the internal combustion (IC) engine and the electric motor parameters. Sgueglia et al. [13, 14] developed a version of the Fixed Aircraft Sizing Tool (FAST) [27] tailored to the hybrid-electric aircraft sizing and integrated sizing tool with OpenMDAO to conduct the multidisciplinary design optimization. Nakka et al. [28] suggested a hybrid-electric aircraft design methodology applied to the simultaneous formulation within the multidisciplinary dynamic system design optimization codesign method. Isikveren et al. [15, 29] suggested the design method for hybrid-electric aircraft using nomographs, which were 2-D plots that could represent all HEPS architectures. De Vries et al. [30–32] established a sizing method to incorporate FEPS and various types of HEPS, including series–parallel HEPS, into a single matrix form and integrate the aero-propulsion benefits of cruise DP to the wing analysis in the conceptual design phase. These studies made much effort to implement EPS into fixed-wing aircraft, such that it became possible to analyze and design electrified fixed-wing aircraft driven by various HEPS as well as FEPS. However, since their methods focused on fixed-wing aircraft, they were not applicable to the flight modes of rotary-wing aircraft (VTOL and transition flight).

Furthermore, other studies have been conducted to expand the electrification target to include VTOL aircraft, thereby allowing various configurations to be covered. Cakin et al. [33] modified the fixed-wing aircraft sizing method to consider the HEPS and lift DP. Hartmann et al. [34] designed four types of HEPS-powered aircraft—fixed-wing aircraft, tilt-wing aircraft, helicopters, and airships—using the sizing method considering HEPS components' efficiency. Finger et al. [16, 35–37] modernized the classical conceptual design method by adding a hybridization factor to the point-performance and mission-performance modules. With this factor, the suggested methodology could cover the various types of HEPS-powered aircraft, including vectored-thrust. Also, one engine inoperative constraint was considered in the proposed method. However, compared with the previous studies aforementioned [30–32], these studies were somewhat limited in implementing the various EPS architecture, including series-parallel HEPS, which uses the motor-generator for the battery charge/discharge.

In addition, most of the proposed conceptual design methods could not handle the noise prediction required to assess the environmental performance of eVTOL aircraft.

1.3.2 Do all disciplines considered in developed conceptual design methods have the same level of fidelity? If not, which disciplines should improve preferentially?

In the conceptual stage, the eVTOL aircraft are designed considering various disciplines, such as aerodynamics, EPS modeling, and weight estimation. Among these disciplines, the existing EPS modelings [12–16, 25–44] used in the concept design method have shown a limited ability to faithfully reflect the electrical characteristics—PMSM operation control strategy, the battery voltage drops, and variations in the EPS efficiency depending on the operating conditions—in the analysis and design of eVTOL aircraft. Because the level of modeling for these electrical characteristics governs the analysis accuracy and design feasibility, more sophisticated EPS modeling is essential in the conceptual design of FEPS-powered VTOL aircraft.

First, the EPS modeling techniques used in the methodologies mentioned in Chapter 1.1 literature survey [12–16, 26–37] assumed that the efficiency coefficients remain constant for each electrical device. However, because these methods do not handle EPS analysis from an electrical engineering perspective, it is impossible to consider changes in the efficiency of the involved electrical devices depending on the current and voltage required to perform a specific mission. Furthermore, they cannot consider the operation control strategies of a PMSM and the voltage drop during a given mission.

McDonald [38, 39] proposed a positive polynomial loss model that can capture the motor efficiency without requiring intricate electric machine modeling, provided that information on the motor efficiency map is available. Because it can be easily applied in the initial design stage, this polynomial loss model has been used in conceptual design studies of various eVTOL aircraft [25, 40, 41]. However, these studies relied on the efficiency maps of specific motors, rendering this approach inapplicable to scalable motor designs. Moreover, because this method cannot consider the electrical characteristics of the motor, it is unable to reproduce the inverter power losses that occur when the inverter supplies AC with varying voltage and frequency to the PMSM.

Mills and Datta [42] examined two modeling methodologies, namely, a simple equivalent DC model and a detailed three-phase AC model, for the analysis of PMSM–rotor coupling in an eVTOL aircraft. Malpica and Withrow-Maser [43] studied the handling qualities of quadrotor configurations for urban air mobility applications with the NDARC software, which uses a motor analysis module based on a detailed three-phase AC model. Because these methods include circuit analysis for motors and inverters, the electrical characteristics of these devices can be partially considered. However, the proposed motor analysis models used the motor constants (torque and back-EMF constant) to simplify the complex PMSMs and inverters into equivalent DC motors. In PMSMs, motor constants are not applicable because the internal power factor angle automatically adjusts the torque angle as the load changes [44]. Therefore, the suggested motor analysis models need to consider the PMSM phase angle based on operation control strategies.

1.4 Motivation and scope of the thesis

According to the previous studies reviewed so far, it appears worthwhile to develop a conceptual design method capable of considering the distinct characteristics of eVTOL AAM vehicles—the diversity of configurations, flight mechanisms, EPS architectures, and performance assessment, including noise prediction. Moreover, it was identified that EPS modeling needs to be enhanced so that electrical characteristics, such as PMSM operation control strategy, battery voltage drops, and variations in the EPS efficiency depending on the operating conditions, can be considered in the conceptual design stage.

The remaining parts of the thesis are organized as follows: After the introduction of Chapter 1, numerical methods for eVTOL conceptual design are described in Chapter 2. This chapter outlines a detailed description of the conceptual design method known as RISPECT+, which consists of five modules: flight analysis, propulsion system sizing, mission analysis, weight estimation, and noise prediction. In addition, this chapter proposes EPS modeling enhancements that enable the conceptual design of FEPS-powered eVTOL aircraft in a more accurate manner by considering electrical characteristics.

In Chapter 3, the validity of the numerical methods addressed in Chapter 2 is demonstrated by comparing experimental data and numerical computation results from previous studies.

In Chapter 4, three types of applications are performed to demonstrate the necessity and capability of the proposed numerical methods for eVTOL conceptual design. In the first application, a comparative study is carried out from two viewpoints regarding payload capacity and mission range to demonstrate performance variations after replacing a FEPS with a HEPS. In the second application, a comparative study is conducted from two perspectives, namely, mission analysis and eVTOL aircraft sizing, to identify the response to size changes of the motor and inverter while modifying the drive system type (direct or indirect) and gear ratio. Lastly, the final application is to investigate the influence of noise prediction on the design optimization of an eVTOL aircraft.

In Chapter 5, the numerical methods for eVTOL conceptual design developed in the thesis and their applications are summarized. Lastly, suggestions for future works are drawn.

Chapter 2.

Numerical Methods for eVTOL Conceptual Design

2.1 Introduction of the developed design methodology

To analyze and design eVTOL aircraft, the design methodology should consider the diversity of configurations, flight mechanisms, and powertrain architectures, as well as performance assessment, including noise prediction. This study, therefore, developed an enhanced conceptual design methodology based on the VTOL aircraft design program, Rotorcraft Initial Sizing and Performance Estimation Code and Toolkit (RISPECT) [45, 46]. The RISPECT system was developed for sizing and performance analysis of various VTOL aircraft types (e.g., compound helicopter and tiltrotor) equipped with IC engines. The RISPECT design algorithm consists of a propulsion-system sizing module to perform a given mission, a mission-analysis module to predict the fuel weight, and a weight-estimation module to obtain the empty weight.

The conceptual design methodology in this study was constructed based on RISPECT's design algorithm and consists of two steps: 1. eVTOL aircraft sizing, 2. Design optimization. Here, the five modules—flight analysis, propulsion system sizing, mission analysis, weight estimation, and noise analysis—were added to consider the characteristics of eVTOL aircraft. The design tool that was built based on this conceptual design methodology was named RISPECT+ [47–52]. The overall flow of the conceptual design methodology is illustrated in Fig. 2-1.

First, the sizing of the eVTOL aircraft is performed to find the maximum take-off weight (MTOW) and EPS specifications, where input data—design variables and parameters—are used. Design variables and parameters in the input data are defined as changing values and fixed values during the design optimization. They include not only the geometry information of the wing, fuselage, thruster, and rod supporting the thruster (e.g., EHang EHang216[viii] and Wisk Cora[ix]) but also the performance information such as maximum discharge C-rate in Table 2-1.

Table 2-1 Design variable and parameters

Components	Design variables and parameters
Wing	span, incidence angle, aspect ratio, taper ratio, sweepback angle, and airfoil
Fuselage	aspect ratio, fineness ratio, and drag coefficient
Thruster	radius, chord, twist, taper ratio, tip-speed, incidence angle, airfoil, number of blades, and number of thrusters
Supporting rod	length, diameter, material, thickness
Other	Maximum discharge and charge C-rate, SE of battery, DOH, SP of electric devices, indicator functions for the battery charge, power control ratios of IC engine, empirical coefficients of IC engine fuel-consumption, drag coefficients of components, technology factor of components weight,…

[viii]Data available online at https://www.ehang.com/ [retrieved 20 October 2022].

[ix]Data available online at https://wisk.aero/ [retrieved 20 October 2022].

The propulsion-system-sizing module calculates the continuous rated power of the powertrain for eVTOL aircraft based on the most extreme mission segments throughout a given mission. As part of the propulsion system sizing process, EPS modeling and flight analysis modules are used to determine the maximum output of the powertrain. The results of this module are passed to the weight estimation module to determine the weight of the propulsion system components. The mission analysis module calculates the consumption of the energy resources (e.g., battery and hydrocarbon fuel usage) and maximum power loss required to perform a given mission with the sized EPS. The results of this module are also transmitted to the weight estimation module for the thermal management system (TMS) and the energy resources. In other words, the powertrain weight is derived using the results from the propulsion-system-sizing and mission-analysis modules. Other components related to the aircraft structure and system are estimated using empirical formulas [52—58]. Next, the available payload weight is computed by subtracting the empty weight from the MTOW. Additionally, the difference between the available and required payload is used as the sizing module's termination condition. MTOW is updated using Eq. (2-1) until the termination condition is satisfied.

$$\begin{aligned} \mathrm{MTOW}^{\mathrm{new}} &= (1-\lambda_{\mathrm{relax}})\mathrm{MTOW}^{\mathrm{old}} \\ &+\lambda_{\mathrm{relax}}\left(W_{\mathrm{empty}}^{\mathrm{new}} + W_{\mathrm{bat}}^{\mathrm{new}} + W_{\mathrm{fuel}}^{\mathrm{new}} + W_{\mathrm{payload,req}}\right) \end{aligned} \tag{2-1}$$

where λ_{relax}, W_{empty}, W_{bat}, W_{fuel} and W_{payload} denote the relaxation factor to increase the convergence speed, empty weight, battery weight, fuel weight, and payload weight, respectively. Then, the noise generated when the eVTOL aircraft hovers at a specific altitude is predicted, and this is used as an assessment indicator of the sized eVTOL aircraft's performance.

As a final step, design optimization is conducted using the eVTOL aircraft sizing results and optimizer while changing the design variables. The optimal design satisfying the design constraints and termination conditions (maximum evaluation or convergence tolerance) is derived.

The five modules—flight analysis, propulsion system sizing, mission analysis, weight estimation, and noise analysis— are the essential parts of the proposed conceptual design methodology and are described in detail in the next chapter.

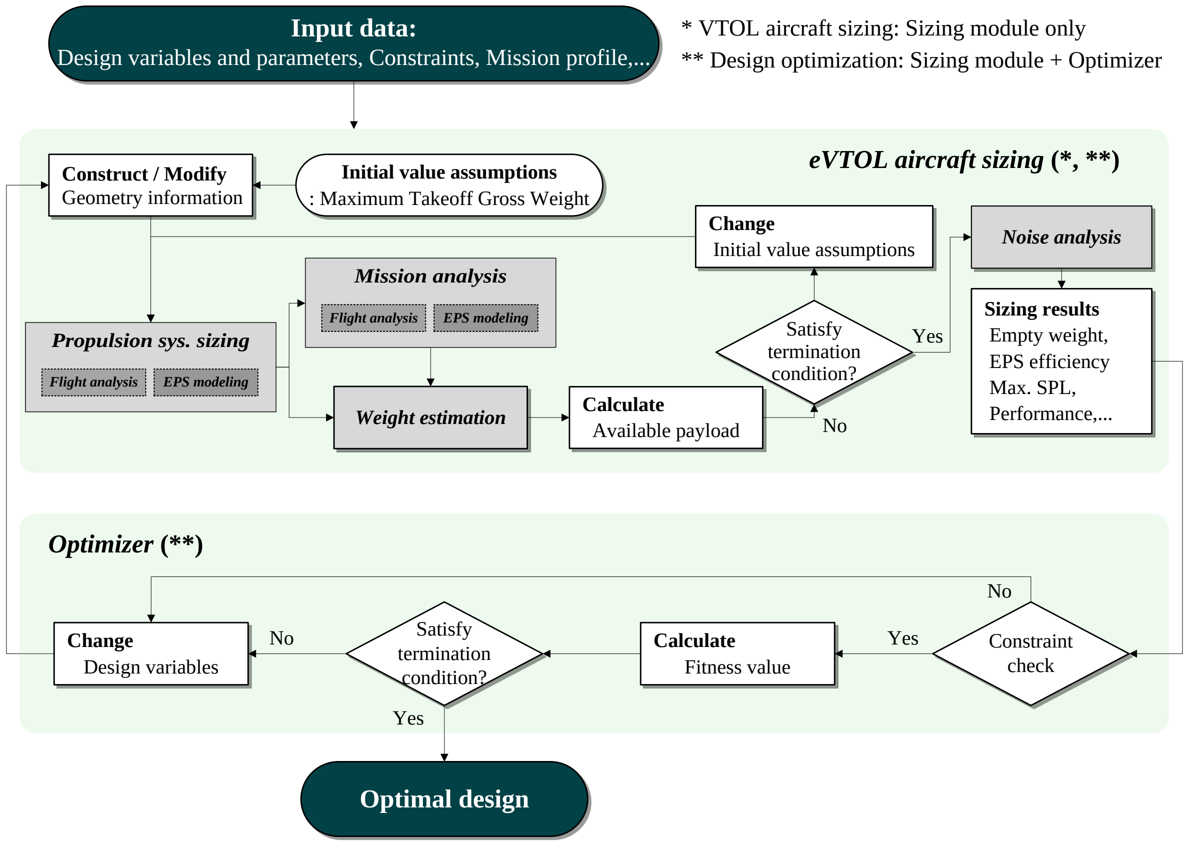

Fig. 2-1 Flowchart of the conceptual design methodology using RISPECT+.

Furthermore, the EPS modeling approaches presented in this study are divided into two categories based on their level of fidelity as follows:

a) *Approach 1 (low-fidelity)*: This is the most straightforward approach to analyzing and designing an EPS, involving little consideration of the electrical characteristics. It assumes that the efficiencies of the electrical devices are constant throughout a given mission and cannot reflect the specifications of each component when sizing the EPS.

b) *Approach 2 (high-fidelity)*: As part of this analysis process, an equivalent circuit and semi-empirical models are used to reflect electrical characteristics. Moreover, the design process integrates additional modules, such as calculating the number of battery cells and regression models for a scalable EPS.

In Chapter 2.2, the propulsion system sizing and mission analysis module uses EPS modeling from the perspective of Approach 1.

Chapter 2.3 describes modules with enhanced modeling capabilities that can consider electrical characteristics based on Approach 2. These modules include modified propulsion-system-sizing and mission-analysis modules, as well as analysis modules for the electric motor, inverter, and battery.

2.2 Modules integrated into developed design methodology

2.2.1 Flight-analysis module

To analyze these various concepts, such as wingless, vectored-thrust, and lift+cruise types, analysis methods for the various components are combined into one module for flight-analysis. The methods used in this study are selected to balance fidelity and computation time in the conceptual-design phase in the conceptual-design stage (e.g., blade-element momentum theory; BEMT, blade element theory; BET).

A flight-analysis module is divided into two stages, as shown in Fig. 2-2. Step 1 identifies the components that are needed for the analysis of the aircraft as a whole according to the role of the lift-generating and thrust-producing devices. Step 2 performs aero-propulsive analysis or structural analysis depending on the type of DP and calculates the control angle satisfying force equilibrium. It is still possible to achieve generality in flight-analysis algorithms even when analysis techniques with higher fidelity are used (e.g., vortex-lattice or finite-element methods).

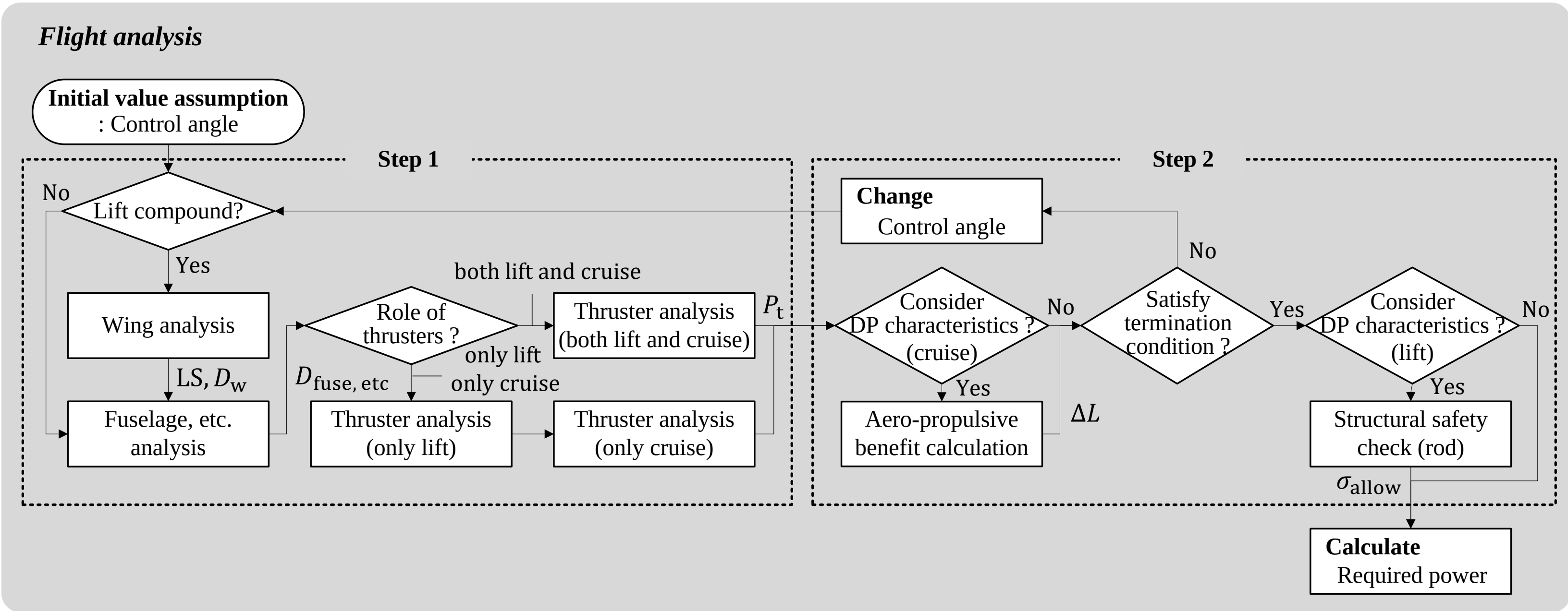

Fig. 2-2 Flight analysis flow chart.

Step 1:

<u>Aerodynamic analysis of components</u>

In the case of eVTOL aircraft with a wing, wing analysis [59] is conducted using the 2D airfoil data and Oswald's factor to obtain the lift-sharing ratio LS and drag, firstly. The lift-sharing ratio is defined as the ratio between the normal forces by the wing and the thruster. It is used to analyze thrusters, especially in transition flight, referred to as conversion flight [60], for the vectored-thrust or lift+cruise concepts. The value of LS is calculated by

$$\mathrm{LS} = 1 - \frac{L_{\mathrm{w}}}{W} \cong \frac{T_{\mathrm{t},z}}{W} \tag{2-2}$$

where W, L_{w}, and $T_{\mathrm{t},z}$ denote the aircraft load, wing lift, and z-axis thrust from the thrusters, respectively.

The aerodynamic analysis of the fuselage and other components (e.g., hub, landing gear, and supporting rod) calculates the drag force D using the concept of an equivalent flat-plate area, f_{e} [Eq. (2-3)]. The value of f_{e} is obtained through the results of a computational fluid-dynamics analysis or an empirical formula [53]. The drag is calculated using

$$D = f_{\mathrm{e}} \times \frac{1}{2}\rho V_{\infty}^{2} \tag{2-3}$$

where ρ and V_∞ denote the air density and freestream velocity, respectively. The interference drag due to thrusters' interaction is ignored since it affects the propulsive efficiency by less than 3% [61].

Depending on the role of the thrusters, their analysis is conducted differently. When using separate thrusters for lift and cruise, an aerodynamic analysis is performed on each thruster. Conversely, when the thrusters handle to lift and cruise simultaneously, an aerodynamic analysis is carried out based on the required thrust—normal force calculated as the forces' sum in the x and z axes [Eq. (2-4)].

$$T_\mathrm{t} = N_\mathrm{t} \times \sqrt{\left(T_{\mathrm{t},x}\right)^2 + \left(T_{\mathrm{t},z}\right)^2} = N_\mathrm{t} \times \sqrt{(D_\mathrm{total})^2 + (\mathrm{LS} \times W)^2} \tag{2-4}$$

where N_t, $T_{\mathrm{t},x}$, and D_total denote the number of thrusters, the x-axis thrust from the thrusters, and the sum of drag forces, respectively. The aerodynamic analysis of the thrusters calculates the shaft power P_t using the BET [62] in Eq. (2-5)

$$\begin{gathered} dP_\mathrm{t} = N_\mathrm{t} N_\mathrm{b} (dL_\mathrm{b} \cos\phi_\mathrm{b} - dD_\mathrm{b} \sin\phi_\mathrm{b}) \Omega y \\ P_\mathrm{t} = \rho A V_\mathrm{tip}^2 \times \frac{N_\mathrm{t}}{2} \int_0^1 \sigma r \sqrt{\lambda^2 + r^2} \left(C_{\mathrm{l,b}} \lambda + C_{\mathrm{d,b}} r\right) \mathrm{d}r \end{gathered} \tag{2-5}$$

where N_b is the number of blades, ϕ is the induced angle of attack, A is the disk area, V_tip is the velocity at the thruster tip, and σ is the solidity. In axial flow conditions, λ is calculated using the BEMT with a 3D stall-delay model [62–64]. If the inflow is much smaller than the tangential velocity of the blade element $(\lambda \ll r)$, λ is calculated by Eq. (2-6)

$$\lambda(r,\lambda_\mathrm{c}) = \sqrt{\left(\frac{\sigma C_{\mathrm{l}_{\alpha,\mathrm{b}}}}{16F} - \frac{\lambda_\mathrm{c}}{2}\right)^2 + \frac{\sigma C_{\mathrm{l}_\alpha}}{8F}\theta r} - \left(\frac{\sigma C_{\mathrm{l}\alpha,\mathrm{b}}}{16F} - \frac{\lambda_\mathrm{c}}{2}\right) \qquad \text{(open rotor)}$$

$$\lambda(r,\lambda_c) = -\frac{\sigma\sigma_\mathrm{d}^2}{4F}\left(C_{\mathrm{l}_{\alpha,\mathrm{b}}} + C_{\mathrm{d,b}}\right) + \sqrt{\left\{\frac{\sigma\sigma_\mathrm{d}^2}{4F}\left(C_{\mathrm{l}_{\alpha,\mathrm{b}}} + C_{\mathrm{d,b}}\right)\right\}^2 + \sigma_\mathrm{d}^2\lambda_\mathrm{c}^2 + \frac{\sigma\sigma_\mathrm{d}^2}{2F}C_{\mathrm{l}_{\alpha,\mathrm{b}}}\theta r} \qquad \text{(shrouded rotor)} \tag{2-6}$$

where C_{l_α} is the slope of the lift curve (2D), F is Prandtl's tip loss factor, θ is the collective pitch angle, λ_c is the climbing velocity ratio, and σ_d is the expansion ratio of the shroud. In non-axial flow conditions, the aerodynamic analysis of the open rotor type is performed based on the blade element theory with the inflow model [62]. On the other hand, the aerodynamic analysis of the shrouded rotor type is conducted with the BEMT and additional calculation of momentum drag [65]. Additional momentum drag is expressed as

$$\Delta D = -\frac{\rho A v_\mathrm{i}}{\sigma_\mathrm{d}\sqrt{\cos\alpha}}\left(V_\infty - v_i\sqrt{\cos\alpha}\tan\alpha\right) \tag{2-7}$$

where v_i and α are the induced velocity and angle of attack, respectively. By considering momentum drag using Eq. (2-7), it is possible to design AAM vehicles using shrouded rotors such as Lilium jet[x] and Ascendance Flight Technologies Atea.[xi]

Step 2:

Aero-propulsive effect from cruise DP

When DP is used in thrusters for cruise, the wake of the cruise DP acts as an additional inflow to the wing. Accordingly, the wake affects the effective angle of attack and velocity of the wing, as shown in Fig. 2-3 [66].

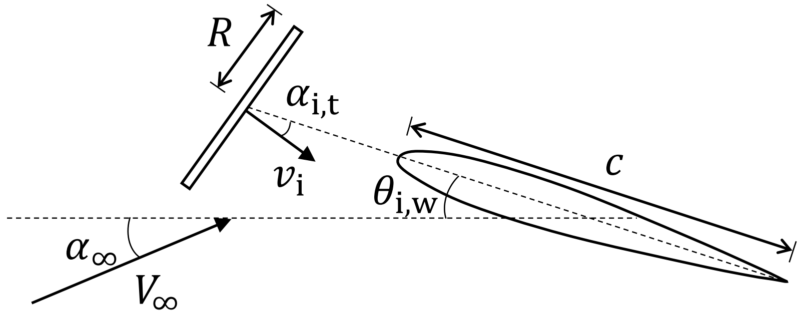

Fig. 2-3 Orientation of freestream velocity and cruise-DP disk with respect to the local airfoil section [66].

---

[x]Data available online at https://lilium.com/ [retrieved 2 October 2022].

[xi]Data available online at https://www.ascendance-ft.com/ [retrieved 22 October 2022].

It is possible to describe this phenomenon using the 2D wing analysis method and the induced velocity of the cruise thrusters, which is expressed [66]

$$\left(\frac{\Delta C_\mathrm{l}}{C_\mathrm{l}}\right)_\mathrm{w} = \left\{1 - \frac{\beta v_\mathrm{i} \sin(\theta_\mathrm{i,t})}{V_\infty \sin(\alpha_\infty + \theta_\mathrm{i,w})}\right\} \times \left\{\frac{\sqrt{V_\infty^2 + 2V_\infty \beta v_\mathrm{i}(\alpha_\infty + \theta_\mathrm{i,w} + \theta_\mathrm{i,t}) + (\beta v_\mathrm{i}^2)}}{V_\infty}\right\} - 1 \tag{2-8}$$

where ΔC_l, i_t, and θ_i represent the increment of lift coefficient by the aero-propulsive effect, the installation angle of the thruster, and the wing incidence angle, respectively. The effect of slipstream height, which cannot be considered via the theoretical approach, is implemented using a surrogate model β developed by Patterson [66]. The value of β depends on multiple parameters, including the induced velocity v_i and the clearance between the cruise DP and the wing, u. When the effects of cruise DP are expanded to a 3D wing, the wing area is submerged in the wake of the thrusters. Therefore, the calculated lift in the 2D wing is extended to the 3D wing using Eq. (2-9), and the increment of lift ΔL_w is calculated by considering the blown area generated by the wake of thrusters, S_blown.

$$\Delta L_\mathrm{w} = \frac{1}{2}\rho\left\{V_\infty^2 + 2V_\infty v_\mathrm{i} \cos(\alpha_\infty + \theta_\mathrm{i,w}) + v_\mathrm{i}^2\right\} \times \Delta C_\mathrm{l,w} \sum_{i=1}^{N} S_{\mathrm{blown},i} \tag{2-9}$$

Subsequently, the aero-propulsive effect is added to the wing lift L_w, and the lift-sharing ratio in Eq. (2-2) is updated using the wing lift with an aero-propulsive effect.

Force equilibrium of VTOL aircraft

Figure 2-4 depicts the forces acting on each eVTOL aircraft concept. To achieve force equilibrium, the wingless aircraft controls its fuselage attitude, while the vectored-thrust aircraft tilts the angle of its thrusters. This control angle, α_{fuse} (or α_{tilt}) affects the AOA of the components, which changes the forces calculated in the previous step (e.g., wing lift and equivalent flat-plate area of the component). For this reason, iterative calculations should be performed until the control angle converges. The control angle is calculated considering all forces by

$$\begin{aligned}\alpha_{\mathrm{fuse}}(\text{or } \alpha_{\mathrm{tilt}}) &= \tan^{-1}\left(\frac{T_{\mathrm{t},x}}{T_{\mathrm{t},z}}\right) \\ &= \tan^{-1}\left(\frac{D_{\mathrm{w}} + D_{\mathrm{fuse}} + D_{\mathrm{hub}} + \cdots + H_{\mathrm{t},x}}{W \times LS - H_{\mathrm{t},z}}\right)\end{aligned} \tag{2-10}$$

where H_{t} denotes the thruster drag force in the disk plane. In addition, the lift+cruise concept obtains the forces from independent thrusters, so the calculation of the control angle is omitted.

Furthermore, assuming that the thrusters are symmetrically positioned concerning the center of gravity, the static margin for longitudinal stability can be calculated as follows [54]:

$$\text{Static Margin} = l_{\mathrm{n}} - l_{\mathrm{c.g.}} = 0.25 + \frac{l_{\mathrm{h}} S_{\mathrm{ht}}}{\bar{c}_{\mathrm{w}} S_{\mathrm{w}}} \frac{C_{L_{\alpha,\mathrm{ht}}}}{C_{L_{\alpha,\mathrm{WB}}}} \left(1 - \frac{\partial \epsilon}{\partial \alpha}\right) - l_{\mathrm{c.g.}} \tag{2-11}$$

where l_{n} is the non-dimension length from the root chord to the neutral point, $l_{\mathrm{c.g.}}$ is the non-dimension length from the root chord and center of gravity, l_{h} is the length between the main wing and the tail wing, $\bar{c}$ is the mean chord length, $C_{L_{\alpha,\mathrm{WB}}}$ is the slope of the lift curve without the wing-body, and $\frac{\partial \epsilon}{\partial \alpha}$ is the rate of change of tail downwash.

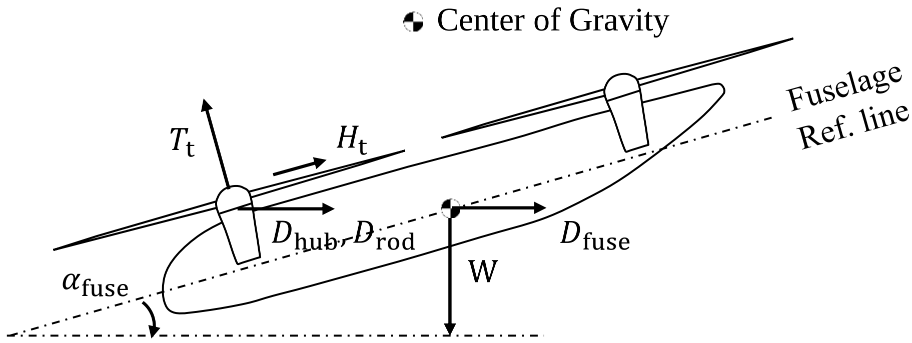

(a) Wingless concept

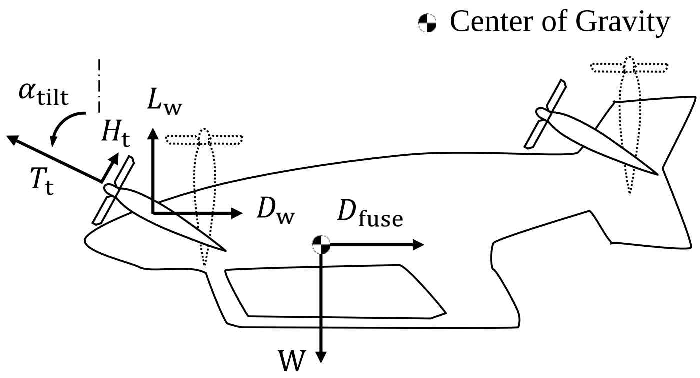

(b) Vectored-thrust concept

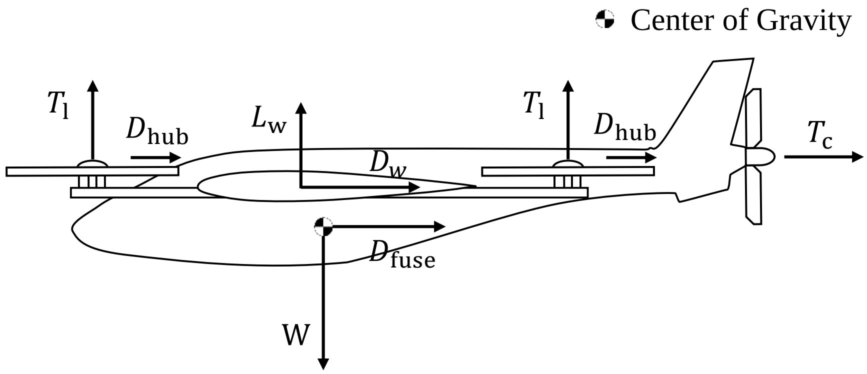

(c) Lift+cruise concept

Fig. 2-4 Forces acting on aircraft during cruise.

Structural safety check for lift DP

When DP is employed as thrusters for lift, bending stress is applied on the supporting rods, as shown in Fig. 2-5.

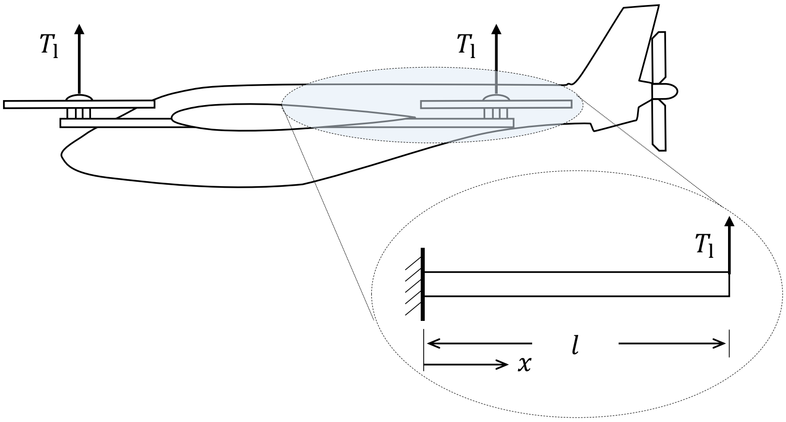

Fig. 2-5 Schematic of VTOL aircraft with lift-DP.

Since conventional aircraft do not have rods to support the lift DP, there is no empirical data regarding their weight and volume. Therefore, this study carried out a structural safety check to compensate for the lack of empirical data. The structural safety check is performed using Euler's 1D-beam theory. The maximum stress σ_{max} acting on the beam is expressed by Eq. (2-12) [67] under the assumption that the lift DP is located l away from the center of the wing and that the supporting rod is a cylinder.

$$\sigma_{\mathrm{max}} = \frac{T_{\mathrm{l}} D_{\mathrm{rod}} l_{\mathrm{rod}}}{2 I_{zz}} \tag{2-12}$$

Subsequently, by comparing the maximum stress and the allowable stress σ_{allow} calculated by Eq. (2-13), the structural safety of a given rod can be confirmed.

$$\sigma_{\mathrm{allow}} = \sigma_{\mathrm{yield}} / \eta_{\mathrm{safe}} \tag{2-13}$$

2.2.2 Propulsion-system-sizing module

For eVTOL AAM vehicles, FEPS is an optimal option that can reduce greenhouse gas emissions; however, due to the limitations of current battery technology, the vehicles performing intracity missions use HEPS as well as FEPS. A HEPS generally comprises thrusters, motors, a motor-generator (MG), inverters, rectifiers, a TMS, a gearbox, and an engine. The HEPS architecture is categorized into series HEPS, parallel HEPS, and series–parallel HEPS, according to power paths and the number of thrusters [30] (Fig. 2-6 (a)–(c)). A series HEPS serially transfers electric power generated by the IC engine and battery to the motor and is suitable for operating multiple thrusters like DP (Fig. 2-6 (a)). A parallel HEPS has two types of parallel power paths (mechanical and electric), which are mechanically coupled to the gearbox. This concept is suitable for a single thruster of one type (Fig. 2-6 (b)). In addition, the concept that combines the two types of HEPS architectures is called series–parallel HEPS (Fig. 2-6 (c)). This has the highest design freedom among the HEPS architectures and is, therefore, complex [30]. Hence, if the propulsion-system-sizing module can handle the series–parallel HEPS, it can handle any type of HEPS architecture and other electric propulsion systems, including turboelectric (Fig. 2-6 (d)) and FEPS (Fig. 2-6 (e)) concepts. Therefore, this study complemented the propulsion-system-sizing module, focusing on the series–parallel HEPS. The proposed propulsion-system-sizing module uses the flight-analysis module (Chapter 2.2.1) to consider all flight modes of eVTOL aircraft, including transition flight.

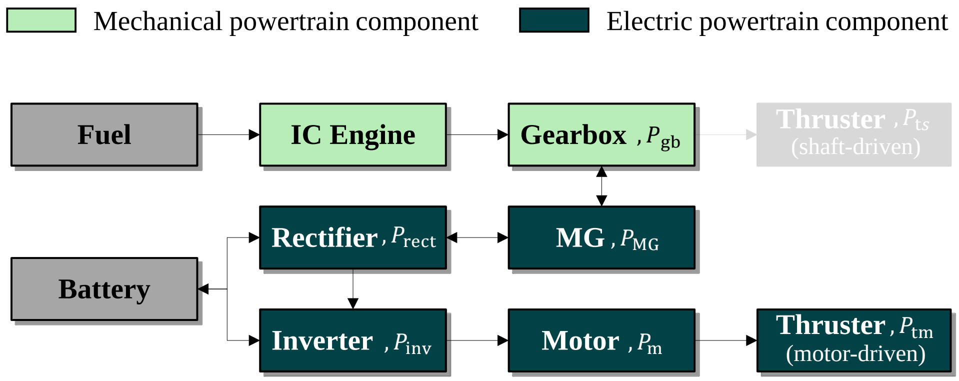

(a) Series HEPS (Only Motor-driven Thruster)

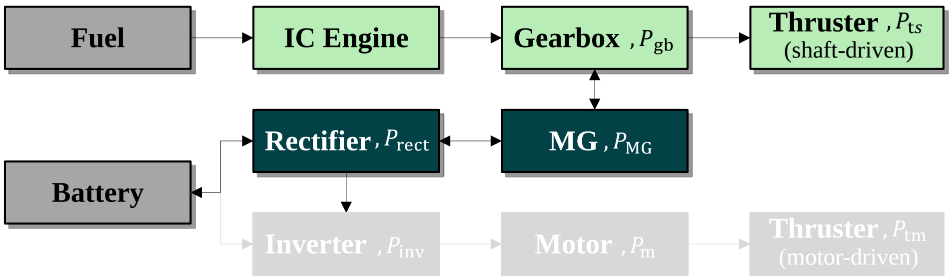

(b) Parallel HEPS (Only Shaft-driven Thruster)

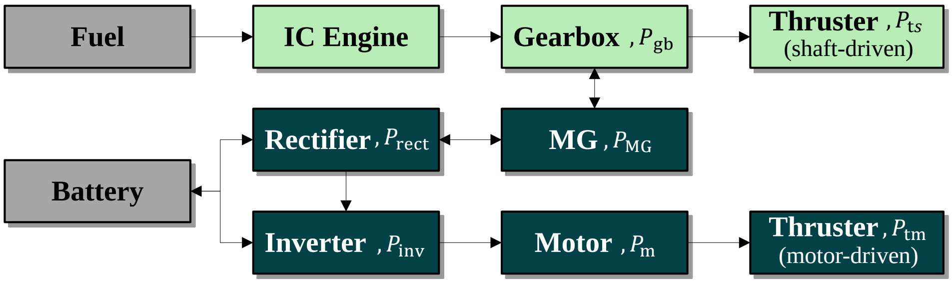

(c) Series–parallel HEPS (Shaft-driven Thruster + Motor-driven Thruster)

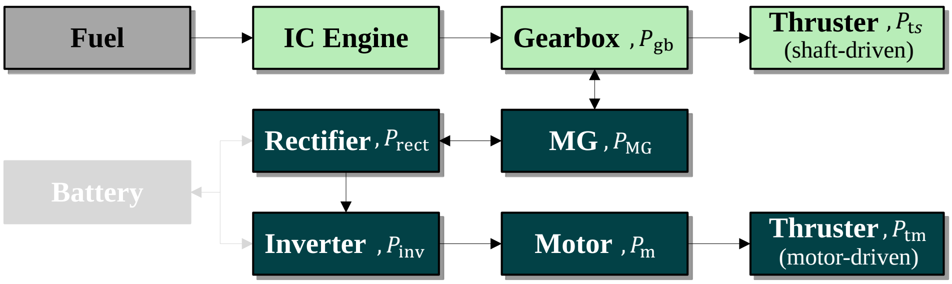

(d) Turboelectric (Shaft-driven Thruster + Motor-driven Thruster)

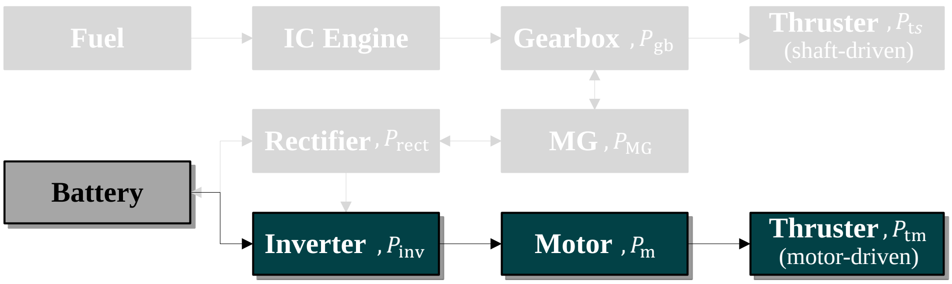

(e) FEPS (Motor-driven Thruster)

Fig. 2-6 Powertrain architectures (modified from de Vries et al. [30])

A propulsion-system-sizing module is composed of three steps (Fig. 2-7). Step 1 calculates the maximum power of the aircraft and thrusters. Step 2 hybridizes the propulsion system using the DOH; implements the power-split based on the maximum power derived from the hydrocarbon fuel and battery. Step 3 sizes the mechanical and electric powertrains based on the maximum power of the aircraft and its components. The following is a detailed description of the propulsion-system-sizing module.

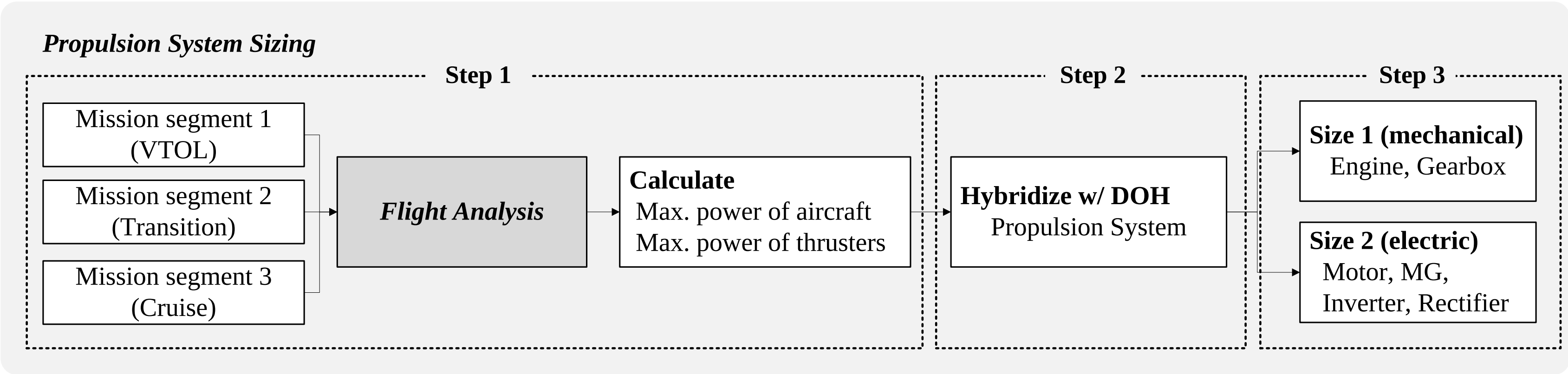

Fig. 2-7 Propulsion system sizing flow chart.

Step 1:

Calculation of maximum power

A flight analysis is performed for three flight modes of the eVTOL aircraft: VTOL, transition flight, and cruising. The analysis conditions are segments of a given mission profile, and the maximum power required for the aircraft and each thruster is derived based on the maximum power P_{max} determined by comparing the shaft power of thrusters [Eq. (2-14)]:

$$P_{\mathrm{max}} = \max(P_{\mathrm{t@VTOL}}, P_{\mathrm{t@Transition}}, P_{\mathrm{t@Cruise}}) \tag{2-14}$$

Note that P_{max} should be obtained by substituting $N_{\mathrm{t}} - 2$ for N_{t} in the flight analysis module if the designer wishes to consider one motor inoperative condition under a specific flight mode.

Step 2:

Hybridization of the propulsion system

To realize hybridization, the DOH is defined as the ratio of maximum power generated by the fuel $P_{\mathrm{HF,max}}$ to that generated by the battery $P_{\mathrm{HB,max}}$, such that [47–49]

$$\mathrm{DOH} = \frac{P_{\mathrm{HB,max}}}{P_{\mathrm{HB,max}} + P_{\mathrm{HF,max}}} = \frac{P_{\mathrm{HB,max}}}{P_{\mathrm{total,max}}} \tag{2-15}$$

If DOH is close to 1, the HEPS characteristics are similar to those of a FEPS since most of the power is derived from the battery. In the opposite case $(\mathrm{DOH} \approx 0)$, the HEPS resembles a turboelectric propulsion system with only hydrocarbon fuel. Additionally, in the case of $0 < \mathrm{DOH} < 1$, $P_{\mathrm{HF,max}}$ has a maximum power-peak-shaving effect that decreases by $P_{\mathrm{HB,max}}(= P_{\mathrm{total,max}} \times \mathrm{DOH})$. This operation of a HEPS can decrease the engine size by as much as $\mathrm{DOH} \times P_{\mathrm{total,max}}$. The optimal DOH that can maximize the advantages of the HEPS depends on the mission profile and aircraft performance. Therefore, DOH is set as a design variable when a designer wants to design with an arbitrary engine. In the case of designing based on existing engine data, DOH becomes an output parameter rather than a design variable.

Step 3:

Mechanical and electric powertrain sizing

The maximum continuous power (MCP) of the IC engine, P_{MCP}, is calculated on the basis of $P_{\mathrm{HF,max}}$ considering the DOH, using the semi-empirical formula Eq. (2-16) [56]. This can be applied to both turboshaft engines and reciprocating engines.

$$P_{\mathrm{MCP}} \cong \frac{P_{\mathrm{HF,max}}}{1-\xi} \times C_3 \tag{2-16}$$

Here, C_3 and ξ represent the engine coefficient to consider the engine lapse rate and the percentage of engine power supplied to accessory items, respectively. The engine lapse rate is calculated as

$$C_3 = \frac{\theta_{\mathrm{alt}}^{C_5}}{\delta_{\mathrm{alt}}^{C_4}} \tag{2-17}$$

where $\theta_{\mathrm{alt}}, \delta_{\mathrm{alt}}, C_4,$ and C_5 denote the ratio of atmospheric pressure at an altitude to standard day sea-level pressure, the ratio of ambient temperature at an altitude to standard day sea-level temperature, and two empirical coefficients for engine lapse rate, respectively.

The sizing for the gearbox, MG, rectifier, inverter, and the motor is performed using the efficiency coefficient η, DOH, and the maximum power required by each component. The maximum required power is calculated using the relationship between input and output power [Eq. (2-18)].

$$\sum P_{\mathrm{out,comp}} = \eta_{\mathrm{comp}} \times \sum P_{\mathrm{in,comp}} \tag{2-18}$$

When this is extended to the powertrain, the maximum power required by the components is calculated in the form of a matrix:

$$\begin{bmatrix} \eta_{\mathrm{m}} & 0 & 0 & 0 & 0 \\ -1 & \eta_{\mathrm{inv}} & 0 & 0 & 0 \\ 0 & 0 & \eta_{\mathrm{rect}} & 0 & 0 \\ 0 & 0 & 0 & \eta_{\mathrm{MG}} & 0 \\ 0 & 0 & 0 & 0 & \eta_{\mathrm{gb}} \end{bmatrix} \begin{bmatrix} P_{\mathrm{m,max}} \\ P_{\mathrm{inv,max}} \\ P_{\mathrm{rect,max}} \\ P_{\mathrm{MG,max}} \\ P_{\mathrm{gb,max}} \end{bmatrix} = \begin{bmatrix} P_{\mathrm{tm,max}} \\ 0 \\ \mathrm{A}^* \\ \mathrm{B}^* \\ \mathrm{C}^* \end{bmatrix} \tag{2-19}$$

where

$$\begin{aligned} \mathrm{A}^* &= \begin{cases} \dfrac{P_{\mathrm{tm,max}} - P_{\mathrm{HB,max}}}{\eta_{\mathrm{m}}\eta_{\mathrm{inv}}} & \text{for FEPS, turboelectric, and series HEPS} \\ \dfrac{P_{\mathrm{ts,max}} - P_{\mathrm{HF,max}}}{\eta_{\mathrm{gb}}\eta_{\mathrm{MG}}} & \text{for parallel HEPS} \\ \max\left[\dfrac{P_{\mathrm{tm,max}} - P_{\mathrm{HB,max}}}{\eta_{\mathrm{m}}\eta_{\mathrm{inv}}}, \dfrac{P_{\mathrm{ts,max}} - P_{\mathrm{HF,max}}}{\eta_{\mathrm{gb}}\eta_{\mathrm{MG}}}\right] & \text{for series–parallel HEPS} \end{cases} \\ \mathrm{B}^* &= \begin{cases} \dfrac{P_{\mathrm{tm,max}} - P_{\mathrm{HB,max}}}{\eta_{\mathrm{m}}\eta_{\mathrm{inv}}\eta_{\mathrm{rect}}} & \text{for FEPS, turboelectric, and series HEPS} \\ \dfrac{P_{\mathrm{ts,max}} - P_{\mathrm{HF,max}}}{\eta_{\mathrm{gb}}} & \text{for parallel HEPS} \\ \max\left[\dfrac{P_{\mathrm{tm,max}} - P_{\mathrm{HB,max}}}{\eta_{\mathrm{m}}\eta_{\mathrm{inv}}\eta_{\mathrm{rect}}}, \dfrac{P_{\mathrm{ts,max}} - P_{\mathrm{HF,max}}}{\eta_{\mathrm{gb}}}\right] & \text{for series–parallel HEPS} \end{cases} \end{aligned} \tag{2-20}$$

and

$$\mathrm{C}^* = \max\left[P_{\mathrm{MG,max}}, P_{\mathrm{ts,max}}, (P_{\mathrm{MG}} + P_{\mathrm{ts}})_{\mathrm{max}}\right] \tag{2-21}$$

The power paths flowing of the rectifier and MG are different according to the MG operation mode: generator or motor. This characteristic is expressed as A^* and B^* according to the HEPS architectures [Eq. (2-20)]. For series–parallel, MG's capability to function as both the generator and motor is considered in A^* and B^* by comparing both series and parallel cases. Additionally, the gearbox can be operated in series or parallel, as well as in series–parallel. When operating in series, P_{MG} is the only power transferred, and P_{ts} is the only power in parallel. In the case of series–parallel, P_{MG} and P_{ts} are transferred together. Therefore, for these operating conditions to be considered, the power acting on the gearbox is calculated using C^* [Eq. (2-21)]. In addition, this matrix can handle turboelectric or FEPS by substituting 0 for the value of an unused electric device; A^*, B^* or C^*.

The sizing results are used to estimate the weight of the propulsion system group, as described in Chapter 2.2.4.

2.2.3 Mission-analysis module

Among the powertrains of eVTOL aircraft, the HEPS can charge or discharge the battery depending on the operating condition. In this study, the mission-analysis module uses a new suggested criterion for battery charge and discharge and calculates the energy consumption required to perform a given mission. In addition, this module can be applicable to FEPS or turboelectric concepts.

The overall flow of the mission-analysis module is divided into two steps (Fig. 2-8). Step 1 decides whether the battery should be charged or discharged. Step 2 calculates the consumption of the energy resources (hydrocarbon fuel and battery), maximum total power loss, and use emissions during the mission. The following is a detailed description of the mission-analysis module.

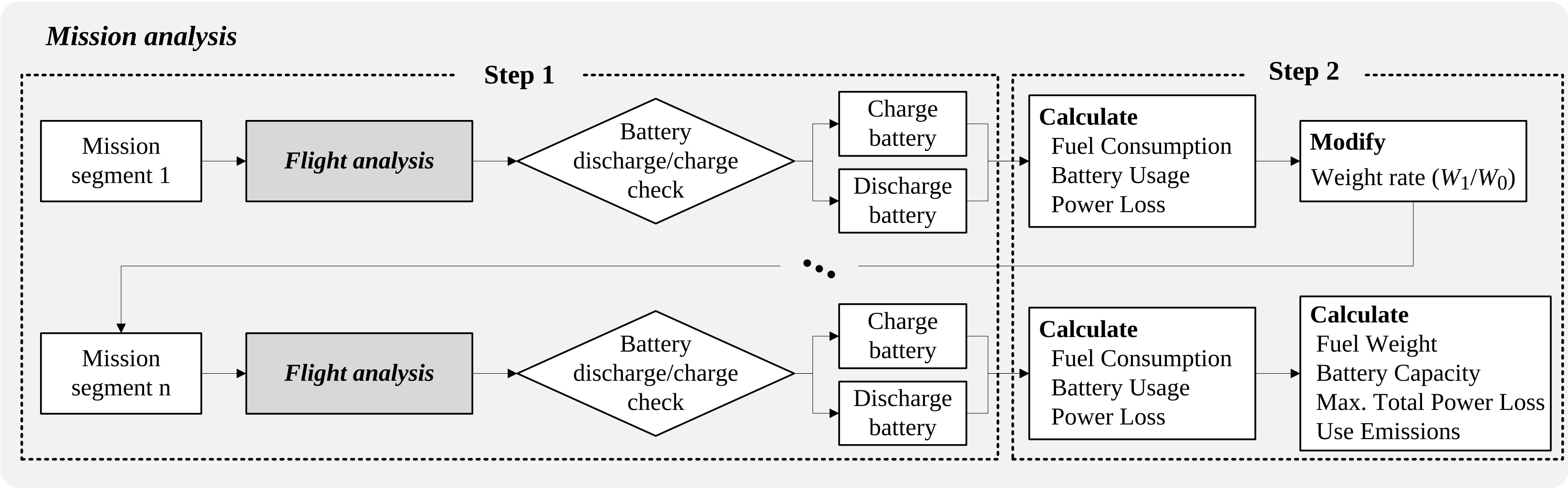

Fig. 2-8 Mission analysis flow chart.

Step 1:

<u>Criterion for battery charge/discharge decision</u>

The parameter used to decide between battery charge and discharge is ΔP, which is the difference between the power obtained from the fuel P_{HF} and the total power required to perform the mission P_{total}:

$$\Delta P = P_{\mathrm{total}} - P_{\mathrm{HF}} = P_{\mathrm{total}} - (\varphi \times P_{\mathrm{HF,max}}) \tag{2-22}$$

where the power obtained from the fuel is calculated using $P_{\mathrm{HF,max}}$ and the power control ratio for the IC engine φ. Since the drastic difference between φ in different mission segments (e.g., $\varphi_{\mathrm{take-off}} = 1$, $\varphi_{\mathrm{landing}} = 0$) may occur excessive power requirement than the mission capability of sized powertrain components, the designer should check the feasibility in the mission-analysis process.

a) *If* $\Delta P > 0$, the mission segment cannot be carried out with the engine alone. Accordingly, the battery is discharged to produce the additional power required.

b) *If* $\Delta P \leq 0$, the mission segment can be performed sufficiently with the engine alone. Furthermore, the engine enables battery charging by converting surplus mechanical power to electric power:

$$P_{\mathrm{c}} = I_{\mathrm{c}} \times (-\Delta P) \qquad \text{at} \quad P_{\mathrm{c}} \leq P_{\mathrm{c,limit}} \tag{2-23}$$

Here, an indicator function I_{c} is used to determine the battery charge's decision at the mission segment. I_{c} takes value 1 at the mission segment set to the battery charge and value 0 otherwise. Additionally, in order to consider the battery life cycle, the maximum power used for charging the battery is limited based on the charge C-rate $Cr_{\mathrm{CSTR,charge}}$ as a design constraint:

$$P_{\mathrm{c,limit}} = \mathrm{Capacity} \times Cr_{\mathrm{CSTR,charge}} \tag{2-24}$$

Note that the power output of the IC engine is set to $P_{\mathrm{c,limit}}$ by adjusting the φ obtained as the design variable in the corresponding mission segment. Subsequently, the fuel consumption and battery capacity required to carry out the mission are calculated by considering the battery charge/discharge criterion.

Step 2:

<u>Calculation consumption of the energy resources (hydrocarbon fuel and battery), maximum total power loss, and use emissions</u>

The amount of hydrocarbon fuel consumed during the mission is calculated using the engine fuel flow rate $\dot{W}_{fuel}$ and mission time:

$$\text{Fuel} = \sum_{i=1}^{n} \left(\dot{W}_{\text{fuel}} \times t\right)_i \tag{2-25}$$

where battery charge and discharge are considered in the calculation of $\dot{W}_{\text{fuel}}$. From Eqs. (2-22)—(2-24), when the battery is discharged ($\Delta P > 0$), the IC engine produces power as much as P_{HF}. In the opposite case, the battery is charged as much as P_{c} (maximum value: $P_{\text{c,limt}}$). Accordingly, the fuel-consumption rate is calculated by considering the battery charge and discharge, where the IC engines' semi-empirical formula is used [68]:

$$\begin{aligned} &\dot{W}_{\text{fuel}} \cong C_1 \delta_{\text{alt}} \sqrt{\theta_{\text{alt}}} P_{\text{IRP}} + C_2 \left[\frac{P_{\text{HF}}}{\eta(1-\xi)}\right] && \text{at } \Delta P > 0 \\ &\dot{W}_{\text{fuel}} \cong C_1 \delta_{\text{alt}} \sqrt{\theta_{\text{alt}}} P_{\text{IRP}} + C_2 \left[\frac{P_{\text{total}} + P_{\text{c}}}{\eta(1-\xi)}\right] && \text{at } \Delta P \leq 0 \end{aligned} \tag{2-26}$$

Here, C_1, C_2, and P_{IRP} denote the two empirical coefficients for engine fuel flow rate and the intermediate-rated power of the engine, respectively. These equations can be applied to all IC engines commonly used in HEPS (e.g., turboshaft[xii] and reciprocating [69] engines).

The battery capacity is calculated using a reduced-order battery model [70], which is a sizing method whereby the constraints on the battery discharge C-rate

[xii] Data available online at https://www.flyingmag.com/rolls-royce-hybrid-electric-propulsion-system/ [retrieved 30 July 2022].

$Cr_{\text{CSTR,discharge}}$ are coupled with the "energy in a box" method. First, the preliminary battery capacity is calculated by accumulating the battery usage for each mission element $E_{\text{bat},i}$:

$$\text{Capacity}_1 = \frac{\max\left(\sum_{i=1}^{1} E_{\text{bat},i}, \sum_{i=1}^{2} E_{\text{bat},i}, \dots, \sum_{i=1}^{n} E_{\text{bat},i}\right)}{DD_{\text{CSTR}}} \tag{2-27}$$

where the maximum DD (DD_{CSTR}) is used to consider battery life as a design constraint. This is usually assumed as 0.8. The battery usage considering charge and discharge is expressed as the product of ΔP and t [Eq. (2-28)], in which the power loss is considered as the efficiency coefficient for electric devices.

$$E_{\text{bat}} = \Delta P/\eta \times t \tag{2-28}$$

Then, the minimum battery capacity satisfying $Cr_{\text{CSTR,discharge}}$ is calculated:

$$\text{Capacity}_2 = \frac{\max(\Delta P_1, \Delta P_2, \dots, \Delta P_n)/\eta}{Cr_{\text{CSTR,discharge}}} \tag{2-29}$$

The final battery capacity is determined based on the bigger battery capacity calculated by Eqs. (2-27) and (2-29). Then, the battery weight is estimated by multiplying the calculated battery capacity and SE [11].

The sum of the maximum power losses of electrical devices obtained based on the mission analysis results is used for the TMS sizing:

$$P_{\mathrm{TMS,max}} = (1 + \kappa_{\mathrm{heat}}) \times \sum \max\{(1 - \eta_{\mathrm{comp},i}) \times P_{\mathrm{comp},i}\}_{i=1,2,\ldots,n} \tag{2-30}$$

where $(P_{\mathrm{TMS}})_{\mathrm{max}}$ is the maximum output power of the TMS and κ_{heat} is the margin to account for the excess heat. In addition, because the TMS is assumed to be liquid-cooled for improving heat rejection and design freedom, the cooling drag is not considered in this study.

In addition, the use emissions of the required energy sources obtained based on the mission analysis results are calculated considering the fuel consumed and the battery recharge as follows [71].

$$\mathrm{Emission_{use}} = \sum_{i=1}^{n} (P_{\mathrm{eng}} \times t)_i \times (\mathrm{Emission}_{\mathrm{c}}^{*} + \mathrm{Emission}_{\mathrm{f}}^{*}) + \mathrm{Capacity_{bat}} \times \mathrm{Emission}_{\mathrm{e}}^{*} \tag{2-31}$$

where $\mathrm{Emission}_{\mathrm{c}}^{*}$ is the emission generated by the fuel consumed during the use phase, $\mathrm{Emission}_{\mathrm{f}}^{*}$ is the emission generated by the production of this fuel consumed, and $\mathrm{Emission}_{\mathrm{e}}^{*}$ is the emission generated by the electric grid used to recharge the batteries. In this study, the sum of $\mathrm{Emission}_{\mathrm{c}}^{*}$ and $\mathrm{Emission}_{\mathrm{f}}^{*}$ is assumed to be 87.5 gCO_2/MJ [72], and the value of $\mathrm{Emission}_{\mathrm{e}}^{*}$ is set to 118 gCO_2/kWh[xiii]

[xiii]Data available online at https://www.eea.europa.eu/data-and-maps/daviz/co2-emission-intensity-12/#tab-googlechartid_chart_11 [retrieved 11 December 2022].

2.2.4 Weight-estimation module

The eVTOL aircraft can be configured with fixed-wing aircraft and rotorcraft components, as well as various combinations of mechanical and electric powertrains. To accurately estimate the component weights of eVTOL aircraft, weight-estimation methods are selectively combined from different sources [52–58]. This module classifies aircraft components into three groups (structure, propulsion, and system) and uses empirical formulas or coefficients.

a) *Structure group*: This group comprises thrusters, wings, fuselage, supporting rods, and landing gear. The weight estimation is performed using only empirical formulas [52, 54–56], where design variables such as the thruster radius and wingspan are used as inputs.

b) *Propulsion group*: This group includes components of mechanical and electric powertrains. The weight estimation is conducted using the corresponding empirical formulas and coefficients [52, 53, 55, 57], where the results of the propulsion-system-sizing and mission-analysis modules (Chapters 2.2.2 and 2.2.3) are used as inputs.

c) *System group*: The weight estimation is performed using the previous studies' [55, 58] systems weight.

The empirical formulas and coefficients used in the weight estimation module are detailed in Table 2-2.

Table 2-2. Component weight-estimation formula based on English units

Group	Component	Estimation formula
Structure	Thruster [52]	$W = 0.08094\chi\, N_\mathrm{t} T_{\mathrm{t,max}}^{1.0477} \left(T_{\mathrm{t,max}}/A_\mathrm{t}\right)^{-0.07821}$ (propeller, fan) $W = \chi W_\mathrm{blade} + \chi W_\mathrm{hub} + \chi W_\mathrm{spin}$ (rotor) · $W_{blade} = 0.0029\ N_r\ N_b^{0.5348}\ R_r^{1.7423}\ c_r^{0.773}\ V_{tip}^{0.8756}\ \nu_r^{2.5105}$ · $W_{hub} = 0.006112\ N_r\ N_b^{0.204}\ R_r^{0.604}\ V_{tip}^{0.528}\ \nu_{hub}^{1.002}\ \left(\frac{W_{blade}}{N_r}\right)^{0.871}$ · $W_\mathrm{spin} = 7.386\ (0.05\ R_\mathrm{r})^2$
	Wing [54, 55]	$W = \chi W_\text{main wing} + \chi W_\text{horizontal tail wing} + \chi W_\text{vertical tail wing}$ · $W_\text{main wing} = 0.009\ \chi\ S_\mathrm{w}^{0.72} \mathrm{AR}_\mathrm{w}^{0.47} (1.5\mathrm{MTOW})^{0.52} \left(\frac{2}{\mathrm{t/c}}\right)^{0.4} \left(\frac{100}{\cos(\Lambda_\mathrm{w})}\frac{t}{c}\right)^{-0.3}$ (w/ the tilt system) · $W_\text{main wing} = 0.032\ \chi\ S_\mathrm{w}^{0.76} \lambda_\mathrm{w}^{0.04}\ (1.5\mathrm{MTOW})^{0.49} \left(\frac{\mathrm{AR_w}}{\cos^2(\Lambda_\mathrm{w})}\right)^{0.6} \left(\frac{100}{\cos(\Lambda_\mathrm{w})}\frac{t}{c}\right)^{-0.3}$ (otherwise) · $W_\text{horizontal tail wing} = 0.7176\chi S_\mathrm{ht}^{1.2} AR_\mathrm{ht}^{0.32}$ · $W_\text{vertical tail wing} = 1.046\chi S_\mathrm{vt}^{0.94} AR_\mathrm{vt}^{0.53}$
	Fuselage [56]	$W = 0.02665\ \chi (N_z \mathrm{MTOW})^{0.943} \left(R_\mathrm{t} \times \frac{N_\mathrm{t}}{2}\right)^{0.654}$
	Supporting rod [52]	$W = N_\mathrm{rod} \rho_\mathrm{rod} \mathrm{Volume}$
	Landing gear [56]	$W = 0.44\ \mathrm{MTOW}^{0.63}$ (skid type) $W = 0.038\ \mathrm{MTOW}$ (wheel type)

Propulsion	Engine [52, 53]	$W = 10.02 N_{\mathrm{eng}} P_{\mathrm{MCP}}^{0.7122} \left(\frac{\mathrm{MTOW}}{N_{\mathrm{eng}}}\right)^{-0.1518} + W_{\mathrm{accessories}} + W_{\mathrm{exhaust\ system}}$
	Gearbox [55]	$W = 0.311(Q_{\mathrm{max}})^{0.8}$ (Vectored thrust) $W = 0.2079(Q_{\mathrm{max}})^{0.8207}$ (otherwise)
	Reduction gear [57]	$W = 72\chi\, N_{\mathrm{g}} P_{\mathrm{g,limit}}^{0.76} \omega_{\mathrm{t}}^{-0.76} \gamma_{\mathrm{g}}^{0.13}$
	Motor [52]	$W = P_{\mathrm{mot,max}}/SP_{\mathrm{mot}}$
	Inverter [52]	$W = P_{\mathrm{inv,max}}/SP_{\mathrm{inv}}$
	Rectifier [52]	$W = P_{\mathrm{rec,max}}/SP_{\mathrm{rec}}$
	Battery [52]	$W = (1 + Pb)\left(N_{\mathrm{cell,series}} N_{\mathrm{cell,parallel}} W_{\mathrm{cell}}\right)$ (case to know W_{cell}) $W = E_{\mathrm{bat}}/SE_{\mathrm{bat}}$ (otherwise)
	TMS [52]	$W = P_{\mathrm{TMS,max}}/SP_{\mathrm{TMS}}$
System	-	$W = 0.07\ W_{\mathrm{fuel}}$ (fuel system [55]) $W = 0.0239\ \mathrm{MTOW} + 195.71$ (etc. [58])

Here, χ is the technical factor, λ_{w} is the taper ratio of the wing, Λ_{w} is the sweep angle of the wing, $\frac{t}{c}$ is the ratio between the airfoil thickness and chord, S is the wing area, Pb is the ratio of the package burden, and w, ht, and vt denote the main wing, the horizontal tail wing, and the vertical tail wing, respectively.

2.2.5 Noise-analysis module

For the noise mitigation of eVTOL aircraft, quantitative criteria have been presented (e.g., the Uber Elevate white paper[xiv] suggests that AAM vehicles taking off and landing at vertiports should satisfy a noise level criteria: maximum A-weighted overall sound pressure level (OASPL) on the ground $L_{\mathrm{A,max}}$ is approximately 62 dBA at 500ft).

To predict the loading noise of eVTOL aircraft at the conceptual design stage, this study uses Farassat's loading noise formulation 1A with a chordwise-compact loading model [73, 74]. Using this model, a sectional loading for the rotor blade is used as the noise source instead of a pressure distribution over a blade surface. This sectional loading is applied to the 0.25-chord length of the airfoil. Therefore, the surface integral of Farassat's loading noise formulation 1A is changed to a line integral, as shown in Eq. (2-32). Here, flow field data are derived from aerodynamic analysis results resulting from BEMT in Chapter 2.2.1.

$$
\begin{aligned}
4\pi p_L'(x,t) = {} & \frac{1}{c}\int_{f=0}\left[\frac{\dot{L}_r}{r|1-M_r|^2}\right]_{\mathrm{ret}} dR \\
& + \int_{f=0}\left[\frac{L_r - L_M}{r|1-M_r|^2}\right]_{\mathrm{ret}} dR \\
& + \frac{1}{c}\int_{f=0}\left[\frac{L_r\left(r\dot{M}_r + cM_r - cM^2\right)}{r^2|1-M_r|^3}\right]_{\mathrm{ret}} dR
\end{aligned}
\tag{2-32}
$$

[xiv]Data available online at https://www.uber.com/elevate.pdf [retrieved 25 July 2022].

where x is the observer position, t is the observer time, c is the speed of sound, L is the local force vector, r is the distance between the observer and the source, M is the local Mach number vector, and dR is the length of a spanwise segment. The subscripts "r," "M" and "ret" denote dot products of the vector with the unit radiation vector, Mach number, and the evaluation of the integrals at retarded time, respectively.

In addition, the thickness noise is predicted using Farassat's 1A thickness noise formula with a dual compact loading model [75]. With the dual compact loading assumption, all chordwise noise sources along the blade surface are replaced by two loading vectors with loading values $\rho_0 c_0^2 h$ in opposite directions, where h is the maximum thickness of the airfoil (Fig. 2-9). The locations for the front and rear loading lines are assumed, based on the previous study [75], to be 0.133- and 0.867-chord lengths of the airfoil, respectively.

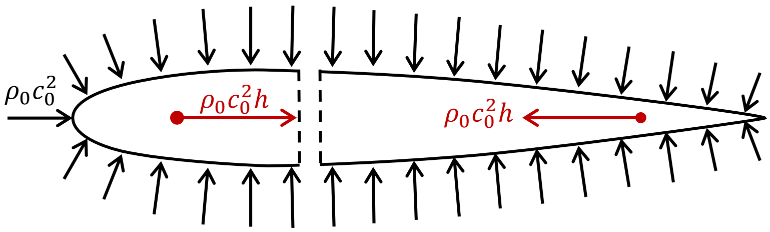

Fig. 2-9 Pressure distribution and integrated loading vector on the front and rear part of an airfoil

A schematic of the loading lines of chordwise-compact loading models is illustrated in Fig. 2-10.

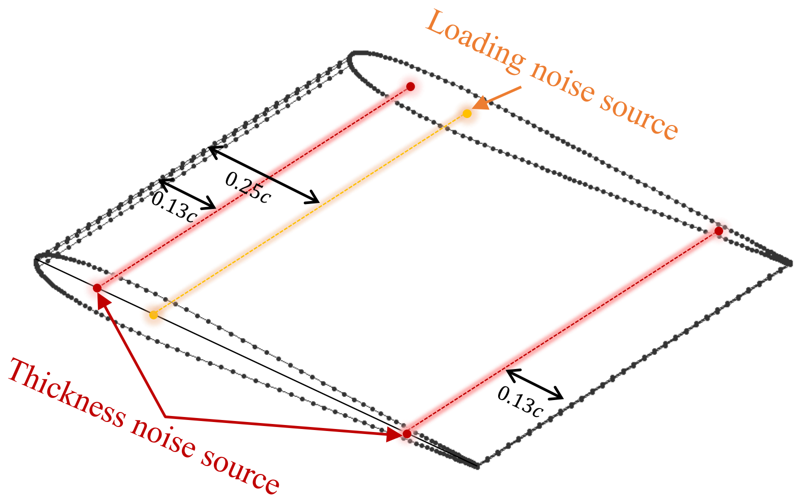

Fig. 2-10 Loading lines of chordwise-compact loading models

Therefore, noise prediction of eVTOL aircraft can be performed in a time-efficient manner by using Farassat's noise formulation 1A with chord-wise compact loading models. A further description of noise prediction can be found in Ref. [51].

2.3 Enhanced EPS modeling for analysis and design

This chapter proposes novel enhancements to the EPS modeling for FEPS-powered eVTOL aircraft conceptual design by taking a more accurate account of the electrical characteristics of each electrical device. To this end, the calculation for the battery stack in series and parallel, as well as regression models for the motor and inverter parameters and consideration of the drive system type (direct or indirect, including a reduction gear), are implemented in modified modules for propulsion-system-sizing and mission-analysis. Moreover, enhanced EPS analysis modules are newly suggested to consider the PMSM operation control strategy, the battery voltage drops, and changes in the EPS efficiency depending on the operating conditions. The proposed EPS analysis modules consist of motor analysis based on the PMSM equivalent circuit with the operation control strategy, inverter analysis with average power loss models, and battery analysis using a near-linear discharge model.

The overall flowcharts illustrating the proposed modules with enhanced EPS modeling are shown in Figures and described in detail in the following sub-chapters.

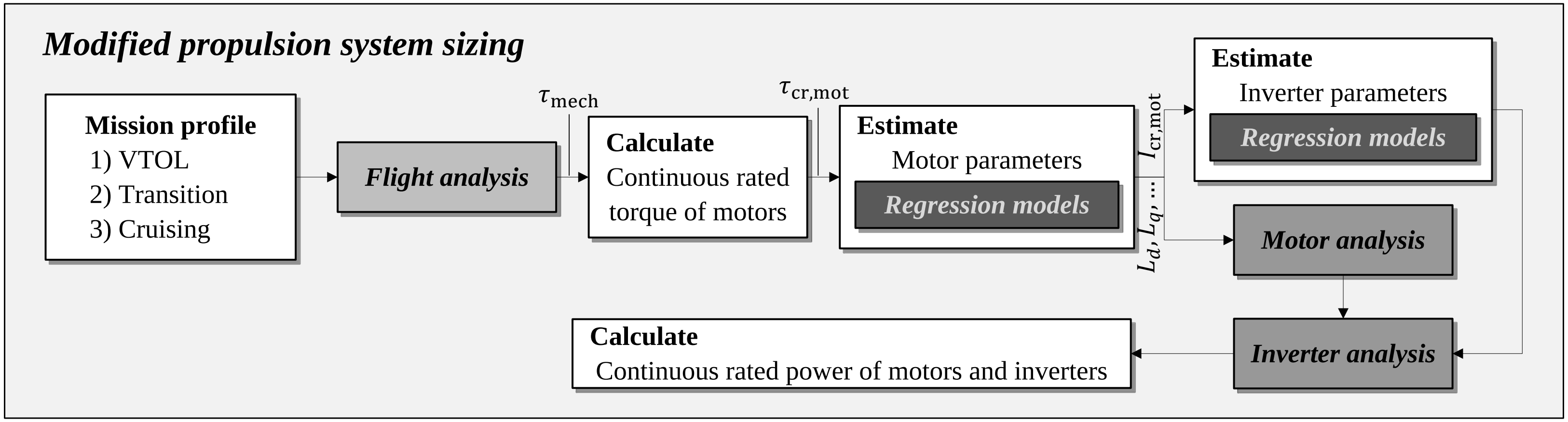

Fig. 2-11 Modified propulsion-system-sizing flow chart.

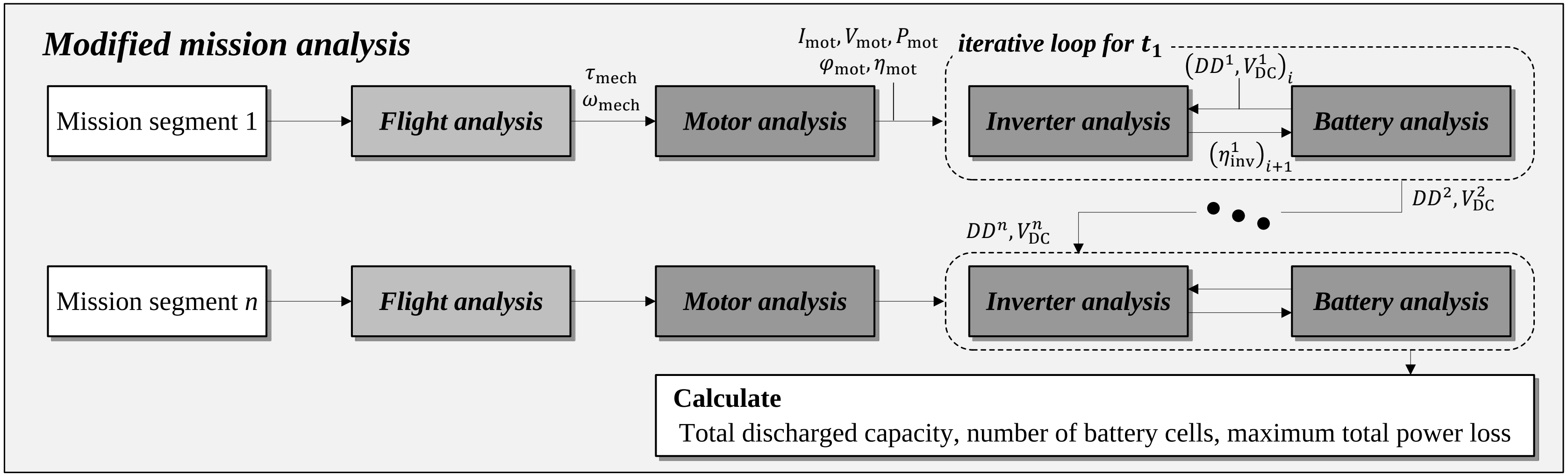

Fig. 2-12 Modified mission analysis flow chart.

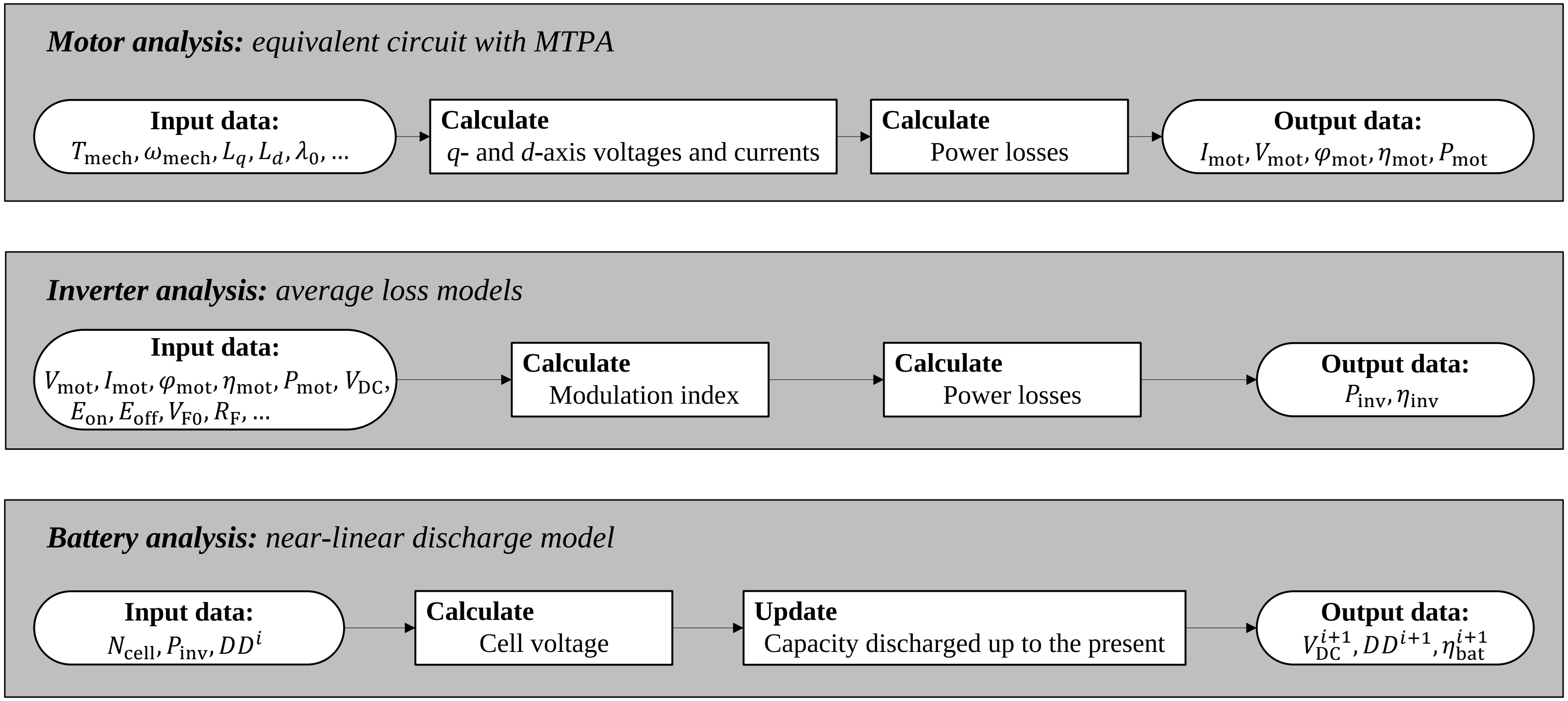

Fig. 2-13 Flowcharts for each electrical device (motor, inverter, and battery)

2.3.1 Modified propulsion-system-sizing module

The modified propulsion-system-sizing module scales the specifications of the motor, inverter, and gearbox (for an indirect drive system) that enable a given mission profile to be performed properly, and the results of this module are passed to the mission analysis and weight estimation modules.

A flowchart for the propulsion system sizing module is presented in Fig. 2-11. First, the continuous rated torque of the motor $\tau_{\mathrm{cr,mot}}$ is obtained by comparing the mechanical torque of the propeller τ_{mech} obtained from the flight analysis results for the main mission segments: VTOL, transition flight, and cruise. The calculation of $\tau_{\mathrm{cr,mot}}$ differs depending on the type of drive system (direct or indirect). In the case of a direct drive system, $\tau_{\mathrm{cr,mot}}$ equals the maximum mechanical shaft torque of the propeller. In an indirect drive system including a reduction gear, $\tau_{\mathrm{cr,mot}}$ is determined using not only τ_{mech} but also the gear ratio γ_{g} and reduction gear efficiency η_{g} for each mission segment.

$$
\begin{aligned}
\tau_{\mathrm{cr,mot}} &= \max\left(\tau_{\mathrm{mech@VTOL}}, \tau_{\mathrm{mech@transition}}, \tau_{\mathrm{mech@cruise}}\right) && \text{(direct)} \\
\tau_{\mathrm{cr,mot}} &= \frac{\max\left[\left(\frac{\tau_{\mathrm{mech}}}{\gamma_{\mathrm{g}}}\right)_{\mathrm{@VTOL}}, \left(\frac{\tau_{\mathrm{mech}}}{\gamma_{\mathrm{g}}}\right)_{\mathrm{@transition}}, \left(\frac{\tau_{\mathrm{mech}}}{\gamma_{\mathrm{g}}}\right)_{\mathrm{@cruise}}\right]}{\eta_{\mathrm{g}}} && \text{(indirect)}
\end{aligned}
\tag{2-33}
$$

Although η_{g} is affected by friction loss and the lubricant, it is herein assumed to be a constant value. As in Chapter 2.2.2, $\tau_{\mathrm{cr,mot}}$ should be obtained by substituting

$N_\mathrm{t}-2$ for N_t in the flight analysis module if the designer wants to consider one motor inoperative condition under a specific flight mode.

Subsequently, the motor specifications (maximum mechanical rotational speed $\omega_\mathrm{mech,max}$, maximum DC link voltage $V_\mathrm{DC,max}$, continuous rated current I_cr, d- and q-axis inductances L_d and L_q, permanent magnetic flux linkage λ_0, and resistance R) required to perform the motor analysis are derived using regression models based on $\tau_\mathrm{cr,mot}$ [Eq. (2-34)]. The continuous rated power of the motor $P_\mathrm{cr,mot}$ is calculated with $\omega_\mathrm{mech,max}$ obtained from $f_1(\tau_\mathrm{cr,mot})$, and the no-load power $P_\text{no-load}$ is obtained from a regression model based on $P_\mathrm{cr,mot}$ [Eqs. (2-35) and (2-36)].

$$y_i = f_i(\tau_\mathrm{cr,mot}), \qquad \boldsymbol{y} = [P_\mathrm{cr,mot}, \omega_\mathrm{mech,max}, V_\mathrm{DC,max}, I_\mathrm{cr}, L_d, L_q, \lambda_0, R] \tag{2-34}$$

$$P_\mathrm{cr,mot} = \tau_\mathrm{cr,mot} \times \omega_\mathrm{mech,max} \tag{2-35}$$

$$P_\text{no-load} = g(P_\mathrm{cr,mot}) \tag{2-36}$$

Here, $\boldsymbol{y}$ is the vector for the regression models of the motor specifications, y_i is the corresponding vector element, and g is the regression model of the no-load power of the motor, as detailed in Appendix A. In this study, the regression models for the motor were constructed using the datasheet information for EMRAX motors[xv],

[xv]Data available online at https://emrax.com/wpcontent/uploads/2020/03/manual_for_emrax_motors_version_5.4.pdf [retrieved 01 September 2021].

which is a representative axial-flux PMSM with high specific power for aircraft propulsion, as stated in an IDTechEx report[xvi]. The efficiencies of the sized motors are then derived using the parameters of the motor specifications.

In addition, the inverter specifications [insulated-gate bipolar transistor (IGBT) turn-on and turn-off energy losses E_{on} and E_{off}, diode reverse recovery energy E_{rec}, IGBT threshold voltage V_{ce0}, diode threshold voltage V_{F0}, IGBT on-state slope resistance R_{ce}, and diode on-state slope resistance R_{F}] required to perform inverter analysis are estimated using regression models. These were constructed using the datasheet information for Infineon dual inverter[xvii] with nominal continuous collector current I_{cn} ratings from 50 to 1,800 A. Moreover, the inverter collector-emitter voltage V_{ces} was set as 1,200 V considering $V_{\mathrm{DC,max}}$ of an electric vehicle [77] because V_{DC} being higher than V_{CES} can cause catastrophic failure of the inverter components[xviii]. In addition, because the scalable parameters of an inverter depend on the virtual junction temperature of the semiconductor T_{vj}, semi-empirical thermal modeling is implemented using a regression model for specific temperatures (25 and 125 °C) and interpolation [Eq. (2-37)]:

[xvi] Data available online at https://www.idtechex.com/airtaxi [retrieved 04 July 2022].

[xvii] Data available online at https://www.infineon.com [retrieved 02 January 2022].

[xviii] Data available online at https://www.dynexsemi.com/Portals/0/PDF/DNX_AN5947.pdf [retrieved 30 January 2022].

$$z_i = h_i(I_{\mathrm{cn}})_{25℃} + [h_i(I_{\mathrm{cn}})_{125℃} - h_i(I_{\mathrm{cn}})_{25℃}]\frac{T_{\mathrm{vj}} - 25℃}{(125℃ - 25℃)}$$

$$\boldsymbol{Z} = [E_{\mathrm{on}}, E_{\mathrm{off}}, E_{\mathrm{rec}}, V_{\mathrm{ce0}}, V_{\mathrm{F0}}, R_{\mathrm{ce}}, R_{\mathrm{F}}] \tag{2-37}$$

where $\boldsymbol{Z}$ is the vector for the regression models of the inverter specifications and z_i and h_i are the corresponding vector elements, as detailed in Appendix A. In addition, the reference parameter of the inverter regression model I_{cn} has a linear relationship with $\left(I_{\mathrm{cr,mot}}\right)_{\mathrm{RMS}}$ obtained from the motor regression model, which is expressed as

$$I_{\mathrm{cn}} = 1.092\left(I_{\mathrm{cr,mot}}\right)_{\mathrm{RMS}} - 6.05 \tag{2-38}$$

Because Eq. (2-38) is somewhat affected by the motor stack length and switching frequency f_{sw} [78, 79], the motor and inverter specifications should be verified during the design process. Finally, the maximum power and minimum efficiency of each electrical device in the main mission segments can be obtained using the motor and inverter analysis modules with the performance parameters. The motor and inverter analysis modules are described in detail in Chapters 2.3.3 and 2.3.4.

2.3.2 Modified mission-analysis module

The modified mission-analysis module couples the aeronautical and electrical fields by linking the flight analysis and analysis for each electrical device, as shown in Fig. 2-12. First, the mechanical torque τ_{mech} and mechanical rotational speed ω_{mech} are calculated using the flight analysis in Chapter 2.2.1. The motor efficiency η_{mot}, magnitude of PMSM current vector I_{mot}, magnitude of PMSM voltage vector V_{mot}, and power factor angle φ are derived using the motor analysis module. Subsequently, the inverter and battery analyses are performed in an iterative loop. This includes V_{DC} with the impact of voltage drop, used for inverter analysis for each mission segment i. This process is conducted throughout the mission, and the minimum number of battery cells is estimated to satisfy the following design constraints: maximum amplitude of the motor phase voltage $V_{\text{mot,CSTR}}$, DD_{CSTR} and $Cr_{\text{CSTR,discharge}}$. First, the number of cells in series $N_{\text{cell,series}}$ is calculated considering the cell voltage V_{cell} and amplitude of the motor phase voltage V_{mot} as

$$N_{\text{cell,series}} = \max\left[\text{ceil}\left(\frac{\sqrt{3}\times V_{\text{mot,CSTR}}}{V_{\text{cell,nominal}}}, \frac{\sqrt{3}\times V_{\text{mot},i}}{V_{\text{cell},i}}\right)\right]_{i=1,2,\ldots,n} \tag{2-39}$$

where i denotes the ith mission segment and $V_{\text{mot,CSTR}}$ equals $V_{\text{DC,max}}$ derived from $f_3(\tau_{\text{cr,mot}})$ in the modified propulsion system sizing module (Chapter 2.3.1). The number of battery cells in parallel $N_{\text{cell,parallel}}$ is then calculated such that the capacity discharged until the end of the mission Q_{end} is maximized, which is expressed as

$$N_{\mathrm{cell,parallel}}^{\mathrm{new}} = \mathrm{ceil}\left[\frac{N_{\mathrm{cell,parallel}}^{\mathrm{old}} \times Q_{\mathrm{end}}}{C_{\mathrm{cell}} \times DD_{\mathrm{CSTR}}}\right] \tag{2-40}$$

where the superscripts “old” and “new” denote the previous and present steps in the converging sizing process, respectively. DD_{CSTR} is usually assumed as 0.8 to consider the battery life. If the maximum discharge C-rate Cr_{max} calculated for the mission is greater than Cr_{CSTR}, the number of battery cells in parallel is calculated as

$$N_{\mathrm{cell,parallel}}^{\mathrm{new}} = \mathrm{ceil}\left[\frac{N_{\mathrm{cell,parallel}}^{\mathrm{old}} \times Q_{\mathrm{end}} \times Cr_{\mathrm{max}}}{C_{\mathrm{cell}} \times DD_{\mathrm{CSTR}} \times Cr_{\mathrm{CSTR}}}\right] \tag{2-41}$$

Through this process, it is possible to accurately estimate the number of cells in the battery pack required to perform the mission.

2.3.3 Electric motor analysis module

In eVTOL AAM vehicles, PMSMs are considered among the most suitable drive systems because of their advantages of high specific power, efficiency, thermal robustness, and low maintenance costs. There are two current components in a PMSM; one is the quadrature-axis current I_{q} in phase with the back-EMF voltages, while the other is the direct-axis current I_{d} 90 degrees out of phase with the back-EMF voltages. Since these phase current components generate magnetic and reluctance torque, there are an infinite number of current vectors that can provide the same amount of torque. An effective PMSM control strategy is required to minimize power losses and ensure optimal current vector selection. Representative PMSM control strategies are as follows [80]:

a) *MTPA control*: This concept determines the maximum torque-to-current ratio, thereby increasing the PMSM efficiency. It provides the current vector with the optimal phase angle β that can output the maximum torque under $I_{\mathrm{cr,mot}}$.

b) *Field weakening control or maximum torque per voltage control*: These concepts increase the rotational speed above the stipulated rating at the expense of reduced torque. In aircraft propulsion, field weakening and maximum torque per voltage control strategies that result in high speed at the expense of torque are ineffective because propulsive loads (fans, rotors, or propellers) reach high power and high speed simultaneously.

In this study, a motor analysis module is developed on the basis of an equivalent circuit model of the PMSM [80] and MTPA control strategy suitable for high-load conditions of aircraft propulsion, as depicted in Fig. 2-14.

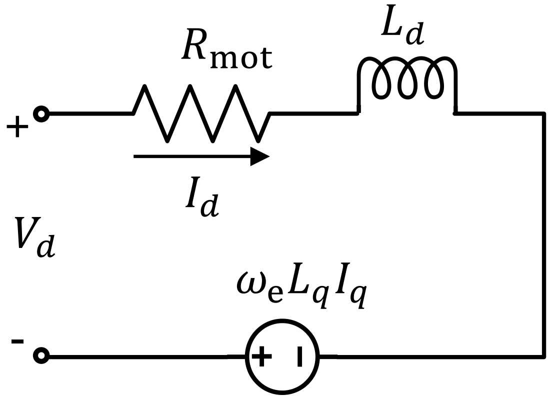

(a) *d* axis

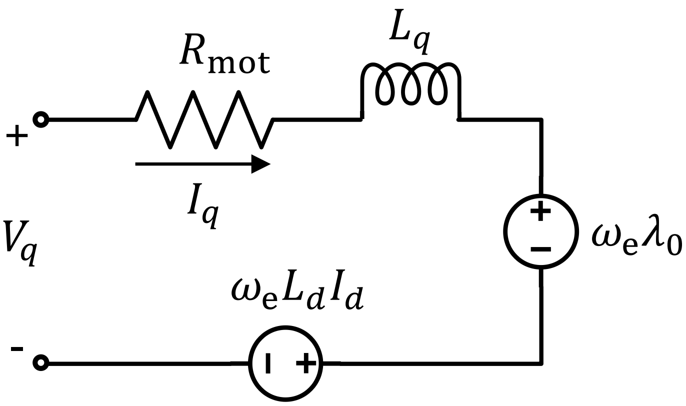

(b) *q* axis

Fig. 2-14 Equivalent circuit model of the PMSM.

This model provides the following simple equations to calculate the relationship between voltage and current at different speeds:

$$\begin{bmatrix} V_q \\ V_d \end{bmatrix} = \begin{bmatrix} R_{\mathrm{mot}} + L_q \dfrac{d}{dt} & \omega_{\mathrm{e}} L_d \\ -\omega_{\mathrm{e}} L_q & R_{\mathrm{mot}} + L_d \dfrac{d}{dt} \end{bmatrix} \begin{bmatrix} I_q \\ I_d \end{bmatrix} + \begin{bmatrix} \omega_{\mathrm{e}} \lambda_0 \\ 0 \end{bmatrix} \tag{2-42}$$

where R_{mot} is the internal resistance, L is the inductance, λ_0 is the permanent magnet flux linkage, and ω_{e} is the electrical rotational speed, which is calculated by multiplying ω_{mech} by the number of pole pairs N_{p}. Assuming a steady state at a constant speed and negligible order of R_{mot} values, the PMSM electromagnetic torque τ_{em} $\left(\text{direct system: } \tau_{\mathrm{mech}}\text{, indirect system: } \frac{\tau_{\mathrm{mech}}/\gamma_{\mathrm{gb}}}{\eta_{\mathrm{gb}}}\right)$ can be expressed as

$$\tau_{\mathrm{em}} = \frac{3}{2\omega_{\mathrm{mech}}} \begin{bmatrix} V_q & V_d \end{bmatrix} \begin{bmatrix} I_q \\ I_d \end{bmatrix} \cong \frac{3}{2} \frac{N_{\mathrm{p}}}{2} \left[\lambda_0 I_q + \left(L_d - L_q \right) \quad {}_d I_q \right] \tag{2-43}$$

where

$$I_d = I_{\mathrm{mot}} \cos \beta \tag{2-44}$$

$$I_q = I_{\mathrm{mot}} \sin \beta \tag{2-45}$$

In addition, φ required for the inverter analysis module is calculated as follows:

$$\varphi = \cos^{-1}\left(\frac{V_d I_d + V_q I_q}{V_{\mathrm{mot}} I_{\mathrm{mot}}}\right) \tag{2-46}$$

The PMSM with MTPA control operates at the maximum torque-to-current ratio, which can be obtained by differentiating Eq. (2-43) with respect to β to zero:

$$\frac{d\tau_{\mathrm{em}}}{d\beta} = \frac{3}{2}\frac{N_{\mathrm{p}}}{2}\left[\lambda_0 I_{\mathrm{mot}} \cos\beta + \left(L_d - L_q\right) I_{\mathrm{mot}}^2 \cos 2\beta\right] = 0 \tag{2-47}$$

which yields

$$I_{d,\mathrm{MTPA}} = \frac{\lambda_0}{2\left(L_q - L_d\right)} - \sqrt{\frac{\lambda_0^2}{4\left(L_q - L_d\right)^2} + I_{q,\mathrm{MTPA}}^2} \tag{2-48}$$

Subsequently, the current vectors of the motor operated by MTPA can be obtained by numerically solving the relationship between Eqs. (2-42) and (2-43) using the Newton–Raphson method [81]. It is assumed that $I_{q,\mathrm{MTPA}}^0$ is $2\tau_{\mathrm{em}}/3N_{\mathrm{p}}\lambda_0$:

$$I_{q,\mathrm{MTPA}}^{k+1} = I_{q,\mathrm{MTPA}}^{k} - \frac{f_{\mathrm{MTPA}}\left(I_q^k\right)}{f_{\mathrm{MTPA}}'\left(I_q^k\right)} \tag{2-49}$$

where

$$f_{\mathrm{MTPA}}(I_q) = (L_q - L_d)^2 I_q^4 + \frac{2\tau_{\mathrm{em}}}{3N_{\mathrm{p}}}\lambda_0 I_q - \left(\frac{2\tau_{\mathrm{em}}}{3N_{\mathrm{p}}}\right)^2 = 0 \tag{2-50}$$

$$f'_{\mathrm{MTPA}}(I_q) = 4(L_q - L_d)^2 I_q^3 + \frac{2\tau_{\mathrm{em}}}{3N_{\mathrm{p}}}\lambda_0 \tag{2-51}$$

Finally, the power losses of the PMSM $P_{\mathrm{loss,mot}}$, η_{mot}, and required power P_{mot} can be calculated using the current vectors obtained from the equivalent circuit with the control strategies as

$$\eta_{\mathrm{mot}} = \frac{P_{\mathrm{em}}}{P_{\mathrm{em}} + P_{\mathrm{loss,mot}}} = \frac{\tau_{\mathrm{em}}\omega_{\mathrm{mech}}}{\tau_{\mathrm{em}}\omega_{\mathrm{mech}} + P_{\mathrm{Cu}} + P_{\mathrm{Fe}} + P_{\text{no-load}}} \tag{2-52}$$

$$P_{\mathrm{mot}} = \frac{P_{\mathrm{em}}}{\eta_{\mathrm{mot}}} \tag{2-53}$$

where the copper loss P_{Cu} is calculated as $3I_{\mathrm{mot,RMS}}^2 R_{\mathrm{mot}}$. The iron loss P_{Fe} is the sum of the hysteresis and eddy current losses, and it is mainly modeled using the 2-D finite element solver as described in Ref. [82].

2.3.4 Inverter analysis module

In general, the PMSM is controlled using a space vector pulse-width modulation (SVPWM) inverter. An SVPWM inverter has two power loss types: switching and conduction. Switching loss occurs when the device transitions from the blocking state to the conducting state and vice versa. Conduction loss occurs if the device is fully conductive. These power losses are affected by the battery voltage as well as the voltage, current, and power factor angle of the motor. In this study, the inverter analysis module was developed using the average loss models for the switching and conduction losses to calculate these losses that vary with the inverter voltage and current [83, 84].

The average loss model of the switching loss for the IGBT and diode is given by

$$P_{\mathrm{sw}} = \frac{f_s}{\pi}\left(E_{\mathrm{on,IGBT}} + E_{\mathrm{off,IGBT}} + E_{\mathrm{off,diode}}\right)\frac{V_{\mathrm{DC}}}{V_{\mathrm{ref}}}\frac{I_{\mathrm{s}}}{I_{\mathrm{ref}}} \tag{2-54}$$

where $E_{\mathrm{on,IGBT}}$ and $E_{\mathrm{off,IGBT}}$ are the turn-on and turn-off energies of the IGBT, respectively; $E_{\mathrm{off,diode}}$ is the turn-off energy of the diode due to the reverse recovery charge current; and V_{ref} and I_{ref} are the reference voltage and current, respectively. The average loss model of the conduction loss for the IGBT and diode can be expressed as

$$P_{\text{cond,IGBT}} = \left(\frac{1}{2\pi} + \frac{1}{8} M \cos\varphi\right) V_{\text{ce0}} I_s + \left(\frac{1}{8} + \frac{1}{3\pi} M \cos\varphi\right) R_{\text{ce}} I_s^2 \tag{2-55}$$

$$P_{\text{cond,diode}} = \left(\frac{1}{2\pi} - \frac{1}{8} M \cos\varphi\right) V_F I_s + \left(\frac{1}{8} + \frac{1}{3\pi} M \cos\varphi\right) R_{\text{F}} I_s^2 \tag{2-56}$$

where V_{ce0} and R_{ce} are the threshold voltage and differential resistance of the IGBT, respectively; similarly, V_{F} and R_{F} are the corresponding parameters for the diode. The modulation index M is the ratio of the amplitude of the line-to-neutral inverter output voltage to the maximum voltage at two-level six-step operation [85]:

$$M = \frac{V_{\text{s}}}{2\,V_{\text{DC}}/\pi} \tag{2-57}$$

With the power losses calculated from the average loss models, the inverter efficiency η_{inv} and required power P_{inv} are obtained as

$$\eta_{\text{inv}} = \frac{P_{\text{em}}/\eta_{\text{mot}}}{P_{\text{em}}/\eta_{\text{mot}} - N_{\text{IGBT}}\left(P_{\text{sw}} + P_{\text{cond,IGBT}} + P_{\text{cond,diode}}\right)} \tag{2-58}$$

$$P_{\text{inv}} = \frac{P_{\text{mot}}}{\eta_{\text{inv}}} = \frac{P_{\text{em}}}{\eta_{\text{mot}}\eta_{\text{inv}}} \tag{2-59}$$

where N_{IGBT} denotes the number of IGBTs, which was assumed to be three because the regression models in this study are based on dual-type inverters (Chapter 2.3.1).

Additionally, the motor and inverter analysis modules were verified by comparing simulation results obtained from the electronic circuit simulation software package PSIM, as described in Chapter 3.3.

2.3.5 Battery analysis module

The resistance and polarization of the active material cause a voltage drop when the battery is discharged [86]. As a result of this voltage drop, the battery's efficiency η_{bat} decreases, resulting in an increase in energy consumption. To consider the voltage drop according to the DD, a battery analysis module is proposed with a simple near-linear discharge model [87] that can be fitted empirically to a battery discharge curve, as illustrated in Fig. 2-15. In this model, the cell voltage V_{cell} is a function of two parameters: the total capacity discharged until the present Q and the battery cell power P_{cell}. The discharge model is expressed as [87]

$$
\begin{aligned}
V_{\mathrm{cell}}^{i+1} = f\left(Q^{i}, P_{\mathrm{cell}}\right) = \frac{1}{2}\left(V_{\mathrm{cell,0}} - KQ^{i}\right) \\
+\frac{1}{2}\sqrt{\left(V_{\mathrm{cell,0}} - KQ^{i}\right)^{2} - 4(R_{\mathrm{cell}}P_{\mathrm{cell}} + GQ^{i}P_{\mathrm{cell}})}
\end{aligned}
\tag{2-60}
$$

where $V_{\mathrm{cell,0}}$ is the open-circuit cell voltage, K is the primary dependence of voltage on the discharged capacity, R_{cell} is the internal resistance, and G reflects the change in the slope of the discharge curve due to current. These parameters can be calculated from four least-squares fitting lines for each discharge curve as

$$\begin{bmatrix} -1 & -I_{12} \\ -1 & -I_{34} \end{bmatrix} \begin{bmatrix} K \\ G \end{bmatrix} = \begin{bmatrix} \left.\dfrac{\partial V_{\mathrm{cell}}}{\partial Q}\right|_{12} \\ \left.\dfrac{\partial V_{\mathrm{cell}}}{\partial Q}\right|_{34} \end{bmatrix} \tag{2-61}$$

$$\begin{bmatrix} 1 & -I_{12} \\ 1 & -I_{34} \end{bmatrix} \begin{bmatrix} V_{\mathrm{cell},0} \\ R_{\mathrm{cell}} \end{bmatrix} = \begin{bmatrix} V_{12,Q=0} \\ V_{34,Q=0} \end{bmatrix} \tag{2-62}$$

where the subscript "12" and "34" denotes the average of the values for discharge curves 1, 2 and 3, 4. $I_{12}, \left.\frac{\partial V_{\mathrm{cell}}}{\partial Q}\right|_{12}$, and $V_{12,Q=0}$ are calculated by obtaining the current, slope, and intercept for discharge curves 1 and 2. In addition, P_{cell} is calculated by dividing the output power of the battery pack by the number of battery cells as follows:

$$P_{\mathrm{cell}} = \frac{P_{\mathrm{inv}}}{N_{\mathrm{cell,parallel}} \times N_{\mathrm{cell,series}}} = \frac{P_{\mathrm{mech}}/(\eta_{\mathrm{mot}}\eta_{\mathrm{inv}})}{N_{\mathrm{cell,parallel}} \times N_{\mathrm{cell,series}}} \tag{2-63}$$

Subsequently, the cell current I_{cell} and η_{bat} are calculated as

$$I_{\mathrm{cell}} = \frac{P_{\mathrm{cell}}}{V_{\mathrm{cell}}} \tag{2-64}$$

$$\eta_{\mathrm{bat}} = \frac{P_{\mathrm{cell}}}{P_{\mathrm{cell}} + P_{\mathrm{loss,cell}}} = \frac{V_{\mathrm{cell}} I_{\mathrm{cell}}}{V_{\mathrm{cell}} I_{\mathrm{cell}} + I_{\mathrm{cell}}^2 R_{\mathrm{cell}}} \tag{2-65}$$

In the next time step, Q and DD are updated as

$$V_{\mathrm{DC}}^{i+1} = V_{\mathrm{cell}}^{i+1} \times N_{\mathrm{cell,series}} \tag{2-66}$$

$$Q^{i+1} = I_{\mathrm{cell}}^{i} \Delta t = \frac{P_{\mathrm{cell}}}{V_{\mathrm{cell}}^{i}} \Delta t \tag{2-67}$$

$$DD^{i+1} = \frac{Q^{i+1}}{C_{\mathrm{cell}} \times N_{\mathrm{cell,parallel}}} \tag{2-68}$$

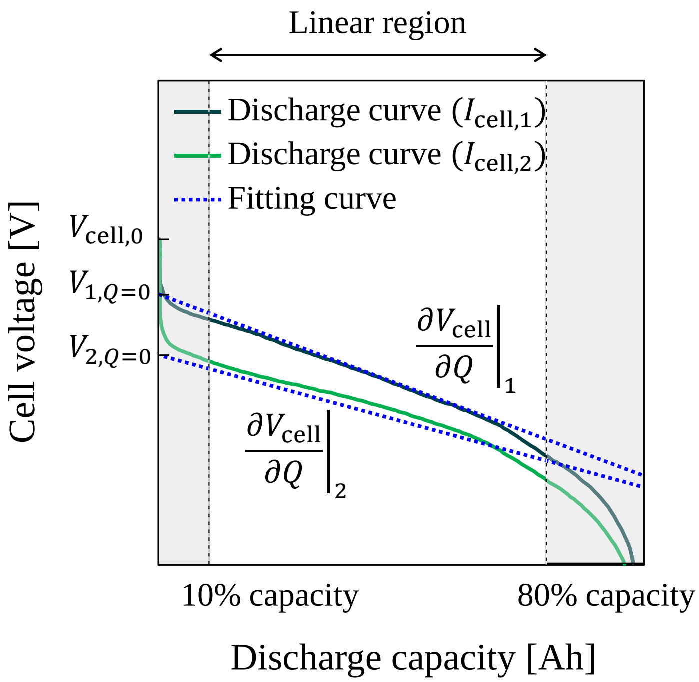

Fig. 2-15 Schematic plot of near-linear discharge model [87].

Chapter 3.

Verification of Numerical Methods

3.1 Flight-analysis module

The flight-analysis module was verified by comparing the experimental data and CFD analysis results for the XV-15 rotor [88–90]. The geometry data of Table 3-1 was used, and the geometric twist was implemented by curve fitting:

$$\theta_{\mathrm{tw}} = 0.5242\left(\frac{r}{R}\right)^2 - 1.2495\left(\frac{r}{R}\right) + 0.632 \tag{3-1}$$

Table 3-1 Geometry data for the XV-15 rotor [88–90]

Type	Value
Number of blades	3
Rotor radius	7.62 m
Rotor chord	0.1084 m in basic blade 0.1316 m in cuff root at 0.0875R Tapering to 0.1084 m at 0.25R
Solidity	0.089
Blade airfoil section	NACA 64-X35 at the root NACA 64-X08 at the tip
Blade lock number	3.83
Tip speed	225.6 m/s

As shown in Fig. 3-1, the flight-analysis module has a high accuracy of less than 9% for hover mode and tilt-rotor mode.

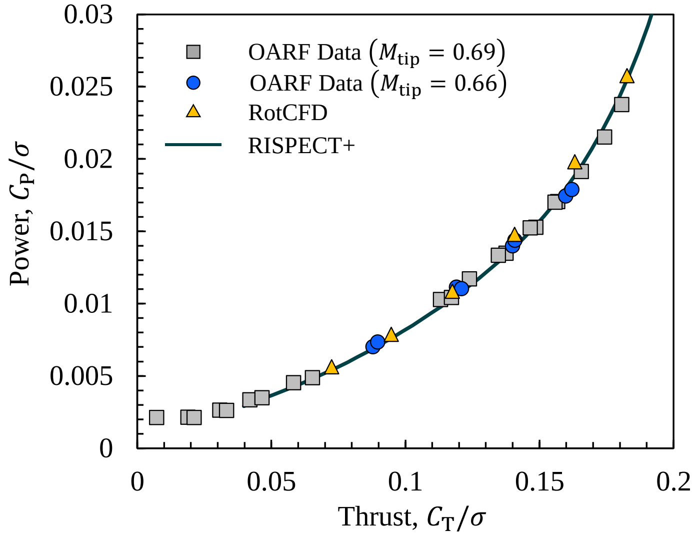

(a) Hover mode

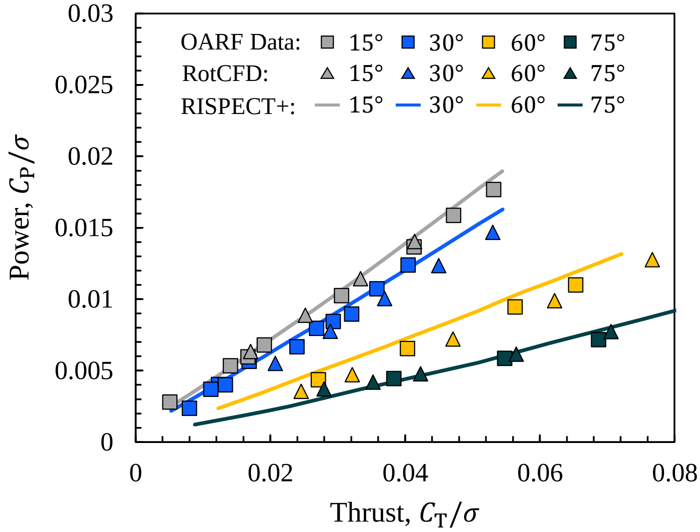

(b) Tilt-rotor mode

Fig. 3-1 Verification of flight-analysis module with XV-15 rotor performance data.

3.2 Weight-estimation module

Verification of the weight-estimation module was performed with the XV-15's weight data [55]. Verification results show that the proposed analysis method has a high accuracy of less than 5% error for the empty weight (w/o system group), as shown in Fig. 3-2.

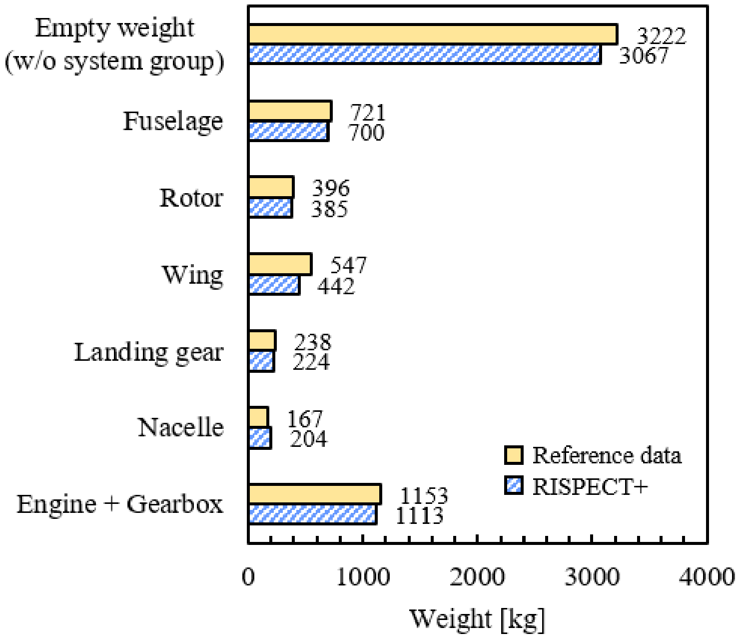

Fig. 3-2 Verification of weight-estimation module with XV-15 weight.

3.3 Motor and inverter analysis modules

The motor and inverter analysis modules were verified by comparison with simulation results obtained in PSIM, which is an electronic circuit simulation software package [91]. As shown in Fig. 3-3, the system used for verification consisted of a motor, inverter, and controller. The conditions used for the verification were as follows:

a) *Motor*: EMRAX 208

b) *Inverter type*: Infineon FF600R12ME4

c) *DC bus*: 470 V (dc)

d) *Speed reference*: 2,000 RPM

The verification results demonstrated the high accuracy of the proposed analysis methods, with an error of approximately 10% for the motor and inverter analysis, as listed in Table 3-2.

Table 3-2 Verification results for the motor and inverter analysis modules

Parameter	PSIM		RISPECT+		Error	
τ_{mech} [Nm]	I_d [A]	I_q [A]	I_d [A]	I_q [A]	I_d [%]	I_q [%]
20	−0.17	35.84	−0.15	33.93	11.8	5.3
40	−0.68	71.31	−0.59	67.85	13.2	4.8
60	−1.51	106.76	−1.32	101.76	12.6	4.7
75	−2.36	133.35	−2.06	127.19	12.7	4.6
f_{sw} [kHz]	P_{cond} [W]	P_{sw} [W]	P_{cond} [W]	P_{sw} [W]	P_{cond} [%]	P_{sw} [%]
10	63.6	145	73.4	140.8	15.4	2.8
20	63.3	299.9	73.8	286.1	16.6	4.6
30	66.4	480.3	74	432.8	11.4	9.8
40	66.3	659.6	74.2	582	11.9	11.7

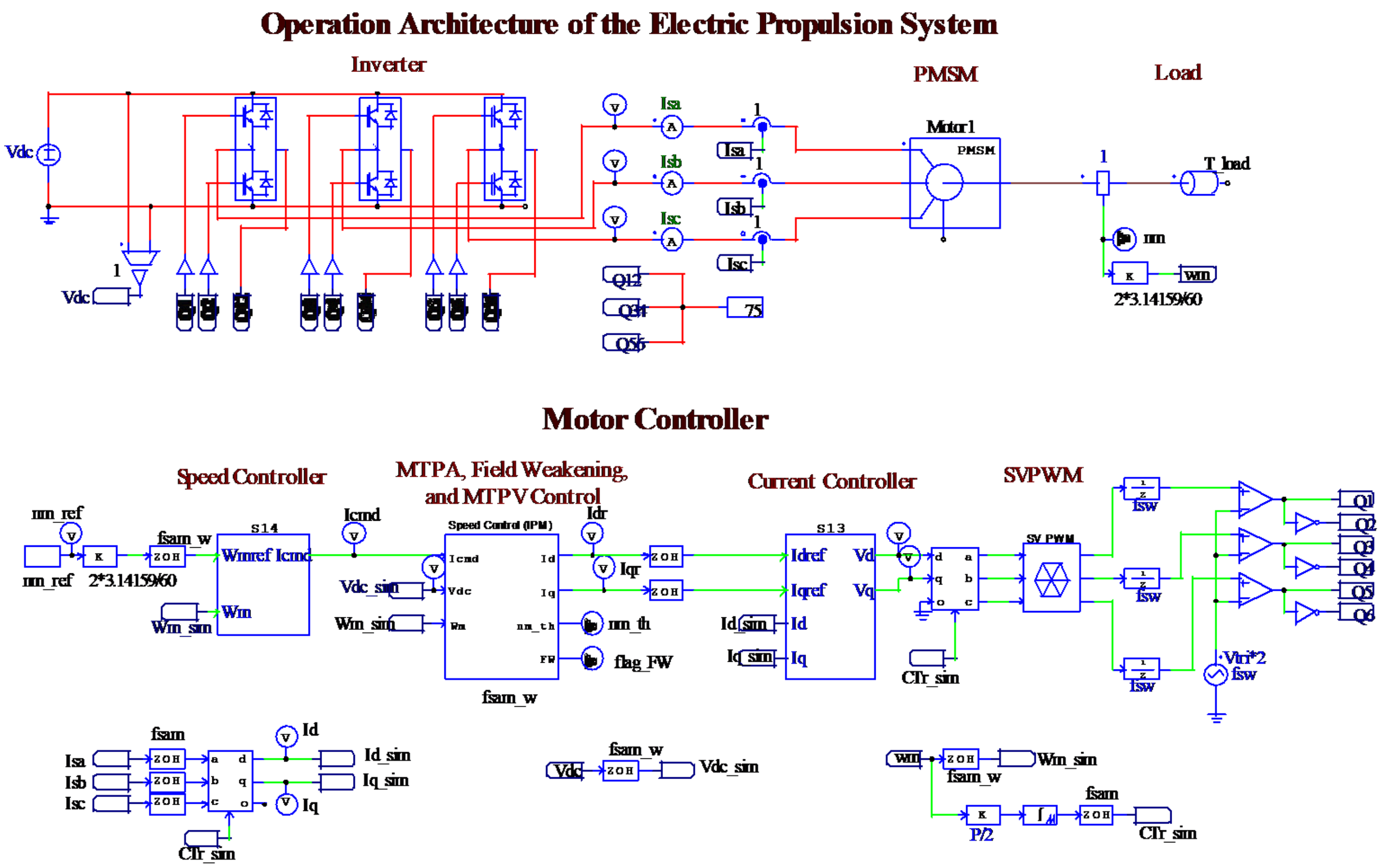

Fig. 3-3 Structural block diagram of the motor with SVPWM inverter in PSIM.

3.4 Conceptual design methodology

Since most AAM vehicles currently under development are FEPS-powered VTOL aircraft, little data is available for HEPS-powered VTOL aircraft. Therefore, indirect verification of the methodology was attempted based on the reasoning that this study's conceptual design methodology can also be applied to FEPS-powered VTOL aircraft. The EPS modeling in this verification was performed based on Approach 1 in Chapter 2.2.

The verification was performed by comparing sizing results obtained in this study with those reported by Vegh et al.[58] for the lift+cruise type with two types of propulsion devices (lift-DP and propeller), based on Wisk Cora Generation 4[xix]. Vegh et al. utilized two types of conceptual design tools, NDARC [53] and SUAVE [41]. Wisk Cora can be viewed visually using the 3D modeling results in Fig. 3-4. Its geometric data and design parameters are detailed in Table B-1.

[xix]Data available on line at https://wisk.aero/generations/ [retrieved 29 September 2022].

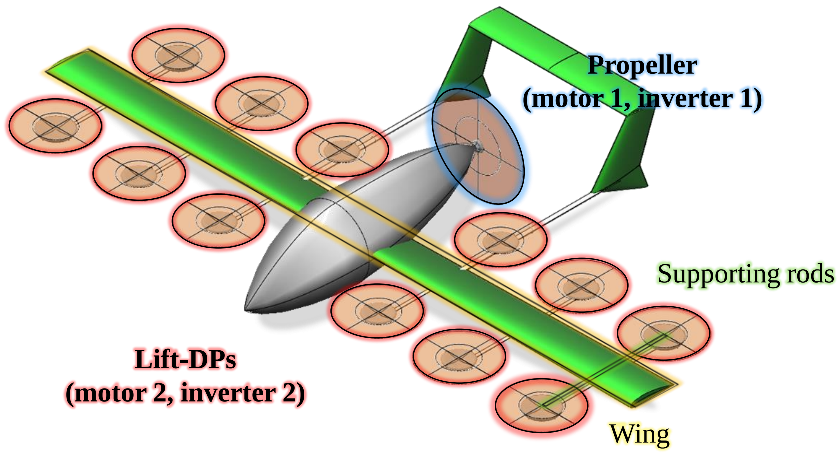

Fig. 3-4 Three-dimensional modeling of Wisk Cora.

The mission profile used for the verification was a simplified Uber Elevate mission profile (Fig. 8), in which the total endurance is 40 min, and the range is 114 km.

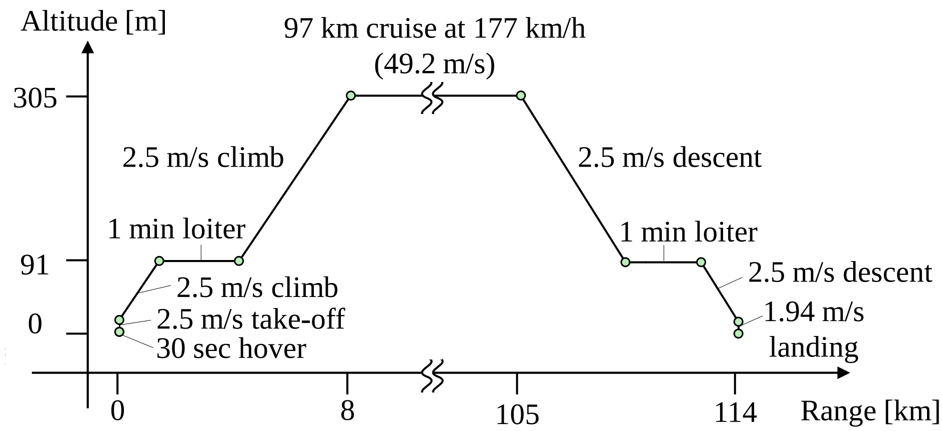

Fig. 3-5 Simplified Uber Elevate mission profile
(modified from Vegh et al. [47]).

Fig. 3-6 shows a weight breakdown chart for the sizing results from NDARC, SUAVE, and RISPECT+. When designed using RISPECT+, MTOW of 1004 kg was derived, thereby resulting in an error of 0.1–6% when compared with the values from NDARC and SUAVE [NDARC: 1005 kg (+0.1%), SUAVE: 944 kg (−6%)]. Component weights and weight fractions from all three conceptual design tools were similar. As such, this comparison demonstrates the validity of all four proposed modules.

Fig. 3-7 shows mission-analysis results based on the estimated MTOW values. The required power and energy trends obtained using RISPECT+ were consistent with those obtained using NDARC and SUAVE. The total energy incurred in all mission elements was 40 kW·h, which differs from the NDARC and SUAVE values by 0.1 kW·h and 7.6 kW·h, respectively. These differences result from the difference in the MTOW and the aerodynamic analytical model and are within a reasonable error-margin range.

The similarity of the results from RISPECT+ with those from NDARC and SUAVE, both of which are considered excellent conceptual design tools, confirms the validity of the conceptual design methodology presented in this study. Moreover, unlike the other two tools, RISPECT+ can handle various EPS types, including the series–parallel type. In addition, with RESPECT+, the electrical characteristics of each electric device can be reflected in the FEPS-powered aircraft conceptual design with reinforcement of EPS modeling, and the noise level can be predicted. Therefore, Chapter 4, Appendix C, and Appendix D present comparative studies and design optimization as examples of applications of RISPECT+. These studies were performed to emphasize solely RISPECT+'s own ability.

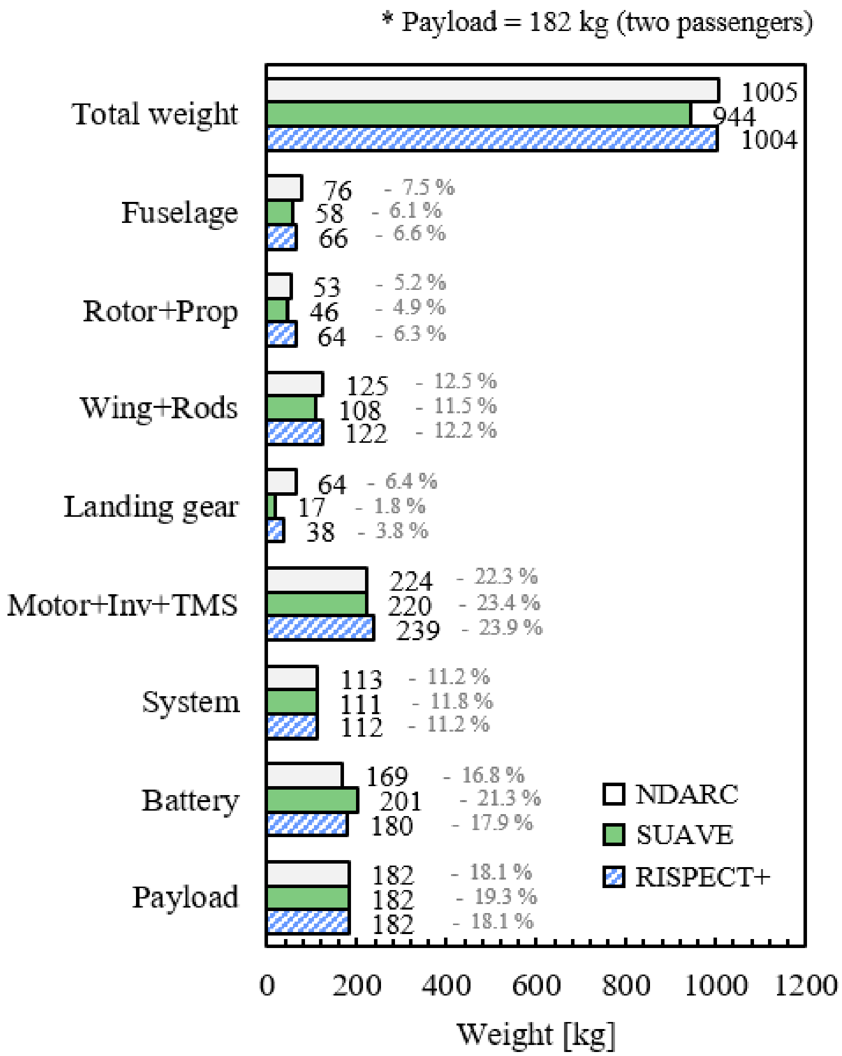

Fig. 3-6 Verification result: Weight breakdown.

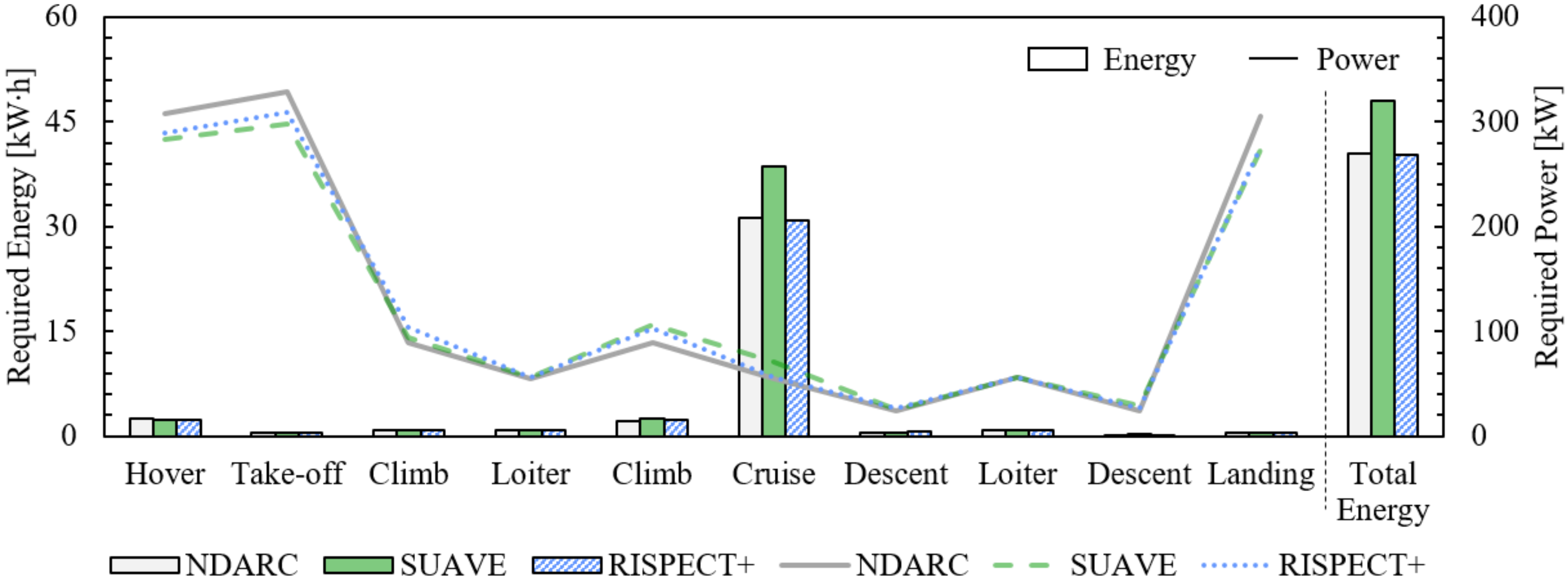

Fig. 3-7 Verification result: Mission-analysis results for simplified Uber Elevate mission profile.

Chapter 4.

Applications of Numerical Methods for eVTOL Aircraft Conceptual Design

4.1 Comparative study between FEPS- and HEPS-powered VTOL aircraft

4.1.1 Problem definition

To investigate the performance variation after replacing a FEPS with a HEPS, a comparative study is performed from two perspectives: payload capacity and the mission range. The baseline FEPS-powered VTOL aircraft is the basis of the sizing results from Chapter 3.4. The HEPS-powered VTOL aircraft is sized under the same design condition—MTOW (1004 kg), geometry, and design parameters—and the following additional design assumptions:

a) HEPS architecture is assumed to be series/parallel HEPS to implement two types of thrusters that generate lift and thrust independently.

b) HEPS-powered VTOL aircraft is sized by changing DOH value from 0 to 1.

c) The IC engine's power control ratio [Eq. (2-22)] is set to a constant value of 1 throughout the mission, except when the excess power exceeds the battery charging limit. Although this engine control strategy would not be optimal, this comparative study used this control strategy to focus on the effects of DOH variations.

4.1.2 Comparison results from the payload capacity perspective

The additional payload indicates the increased payload capacity of HEPS-powered aircraft. It is represented as the difference between the available payloads of the two propulsion systems with identical MTOW and mission range, which is expressed by Eq. (4-1)

$$\text{additional payload} = \left(W_{\text{payload,avail}}\right)_{\text{HEPS}} - \left(W_{\text{payload,avail}}\right)_{\text{FEPS}} \tag{4-1}$$

where the available payload is calculated by subtracting the sum of W_{empty}, W_{fuel}, and W_{bat} from MTOW, as mentioned in Chapter 2.1.

It can be seen in Fig. 4-1 (a), HEPS-powered VTOL aircraft could carry more payload compared to its FEPS-powered counterpart in areas where the DOH exceeds 0.5, and the maximum value is 40 kg. The gradient of the additional payload tends to change rapidly around DOH = 0.90. These results could be attributed to the weight change of energy sources and components—battery, hydrocarbon fuel, MG, rectifier, IC engine, and gearbox—according to the change of DOH, as shown in Fig. 4-1 (c). An increase in DOH corresponds to a reduction in power obtained from a hydrocarbon fuel, thereby resulting in the downsizing of propulsion-system components—IC engine, gearbox, MG, and rectifier—involved in generation and transfer for fuel-supplied power, increasing the available hydrocarbon fuel and battery capacity. This influence of the hybridization becomes a benefit after DOH = 0.50, and this benefit is maximized at DOH = 0.90. The upsurge in battery weight occurs beyond DOH = 0.90, thereby causing the hydrocarbon fuel capacity to be reduced. In addition, when DOH is 0.8, mechanical and electrical energy consumption rapidly changes, and total use emissions have a maximum value (14.8 kgCO_2-eq), as shown in Fig. 4-1 (a) and (c). The reason why DOH affects the mission analysis results and components weight at 0.8 and 0.9 is shown in Fig. 4-2.

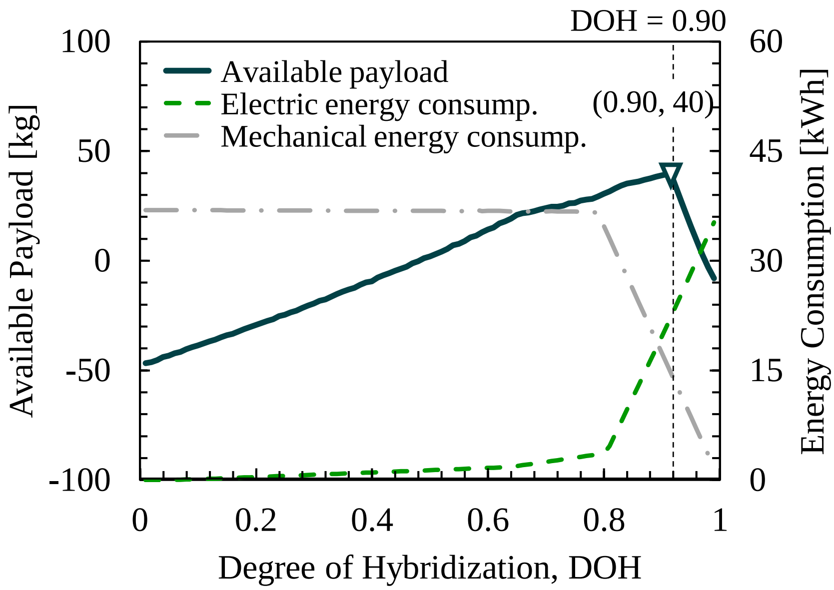

(a) Additional payload vs. DOH

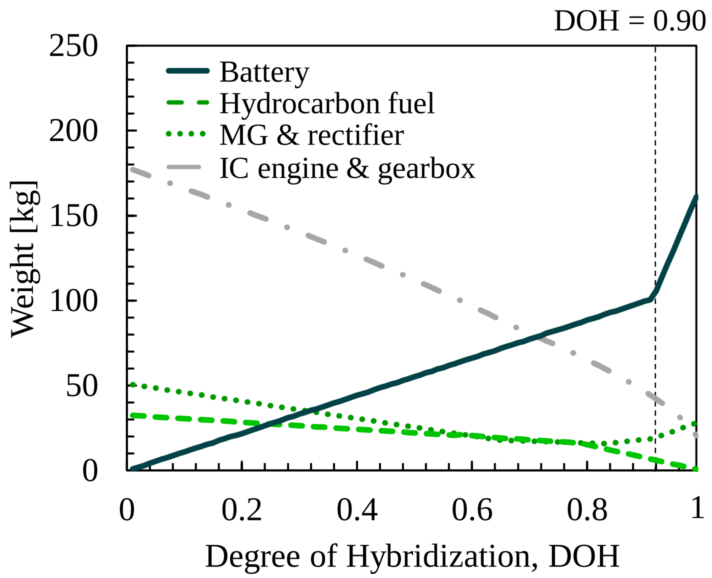

(b) Component weight vs. DOH

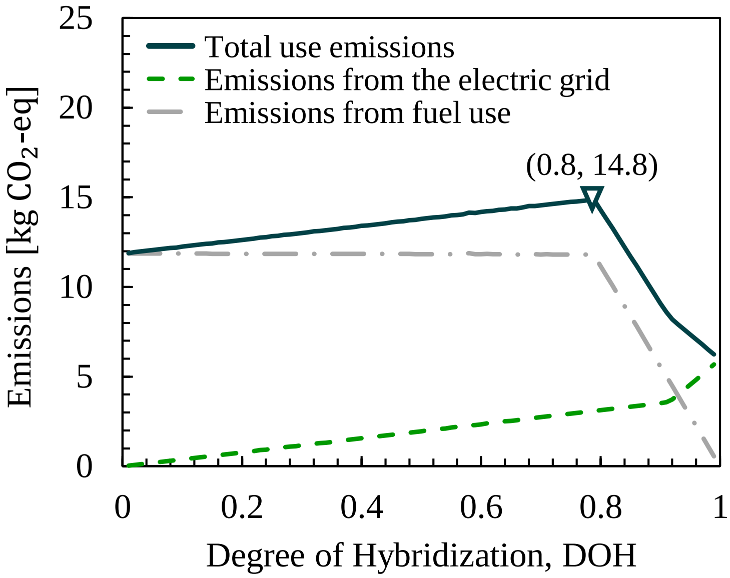

(c) Emission vs. DOH

Fig. 4-1 Sizing results of HEPS-powered VTOL aircraft vs. DOH variation (for fixed MTOW and mission range)

Fig. 4-2 shows the flight-analysis results for the simplified Uber mission for the required payload, 182 kg—two passengers. Here, the area of the graph is the energy required for the mission segment. The calculated area can be divided into the battery- and fuel-supplied energy based on $P_{\mathrm{HF,max}}$. When DOH = 0.8 is exceeded, battery-supplied energy is used to be carried out forward flight as well as axial flight (hovering and takeoff/landing), and the area of battery-supplied energy increases rapidly. Therefore, the trends of energy consumption and use emission change from DOH = 0.8 as a starting point. Also, $\mathrm{Capacity}_1$ [Eq. (2-27)] becomes larger than $\mathrm{Capacity}_2$ [Eq. (2-29)] after specific DOH. Furthermore, the payload capacity is improved by downsizing the propulsion system corresponding to the decrease in $P_{\mathrm{HF,max}}$, referred to as “maximum power-peak shaving.” That is, battery sizing is performed based on the total energy after DOH = 0.90 and the gradient of additional payload switches signs because a surge of battery weight results in a decrease in the weight of the hydrocarbon fuel. This is the reason why the maximum value of the additional payload, 40 kg, is found when DOH = 0.90.

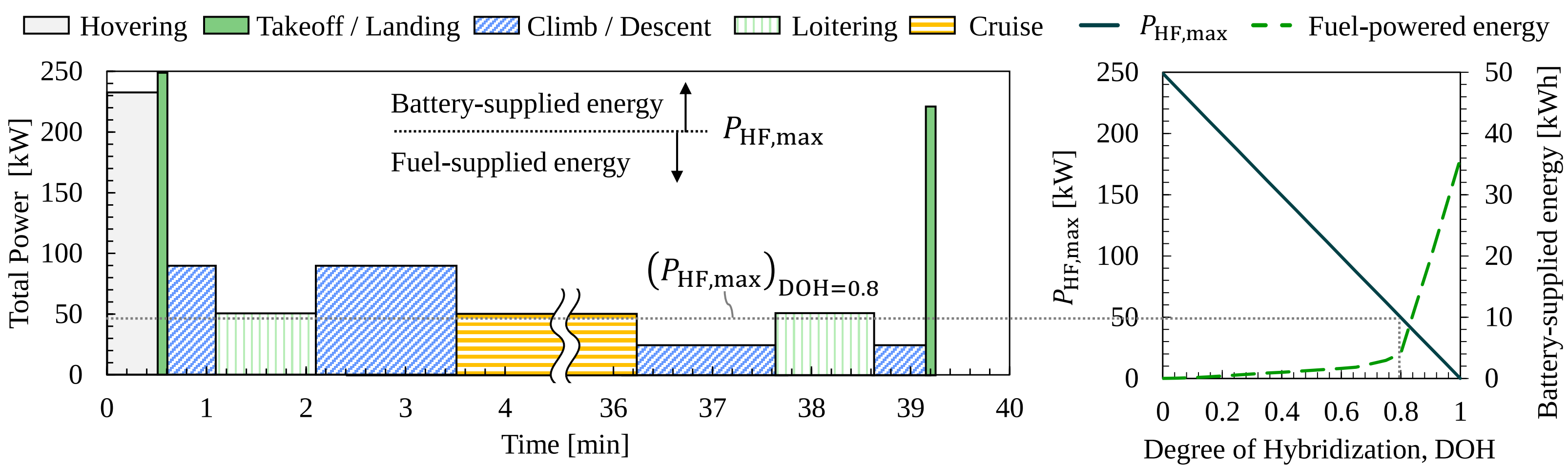

Fig. 4-2 Flight-analysis results: output power for the mission segment (fixed mission range: 114 km).

4.1.3 Comparison results from the mission range perspective

The mission range of the HEPS-powered VTOL aircraft is calculated under the assumption that the increased payload capacity is converted to additional energy sources (hydrocarbon fuel and battery). The extended range can be defined as the difference between the mission range of each propulsion system for the same MTOW (1004 kg) and payload (182 kg—two passengers):

$$\text{extended range} = \text{range}_{\text{HEPS}} - \text{range}_{\text{FEPS}} \tag{4.2}$$

Fig. 4-3 illustrates the extended range, weight change of components, and use emissions according to the change of the DOH. It can be seen in Fig. 4-3, HEPS-powered VTOL aircraft could not achieve the design requirement—182 kg payload—below DOH = 0.26. HEPS-powered VTOL aircraft have an extended mission range compared to FEPS-powered aircraft in areas where the DOH exceeds 0.5, and the maximum value is 286 km. The gradient of the extended mission range changes rapidly around DOH = 0.83. The point of DOH at which the maximum value is calculated and the trend of hydrocarbon fuel weight with DOH variation is slightly different from the result in Chapter 4.1.2. It is because the total endurance increases as the mission range prolongs, which affects the battery sizing criterion [Eqs. (2-27) and (2-29)] and the engine operation.

Based on the comparison results from the mission range perspective, the mission range of eVTOL aircraft is applied to major cities in the United States and Europe, as shown in Fig. 4-4. The radius of the circle represents the mission range of each concept. The FEPS-powered concept is limited to the intracity mission (green circle). The HEPS-powered concept demonstrates an extended flight operating area (blue circle), and the one-way intercity mission from Los Angeles to San Francisco or New York to Washington can be accomplished. In the case of Europe, the extended flight envelope of HEPS-powered VTOL aircraft covers the range from Paris to London. In this way, the HEPS-powered VTOL aircraft possess the potential to perform intercity missions, as well as international missions, until battery technology is enhanced enough.

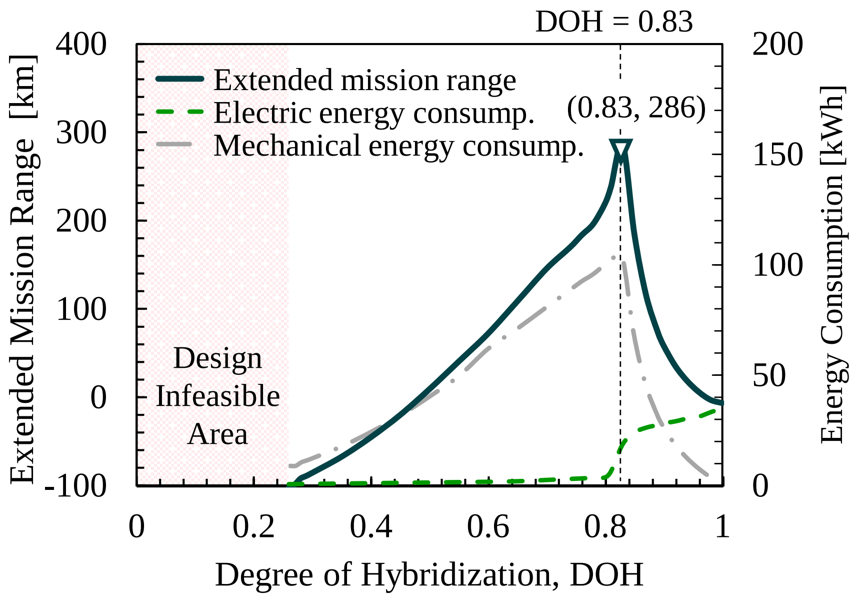

(a) Extended mission range vs. DOH

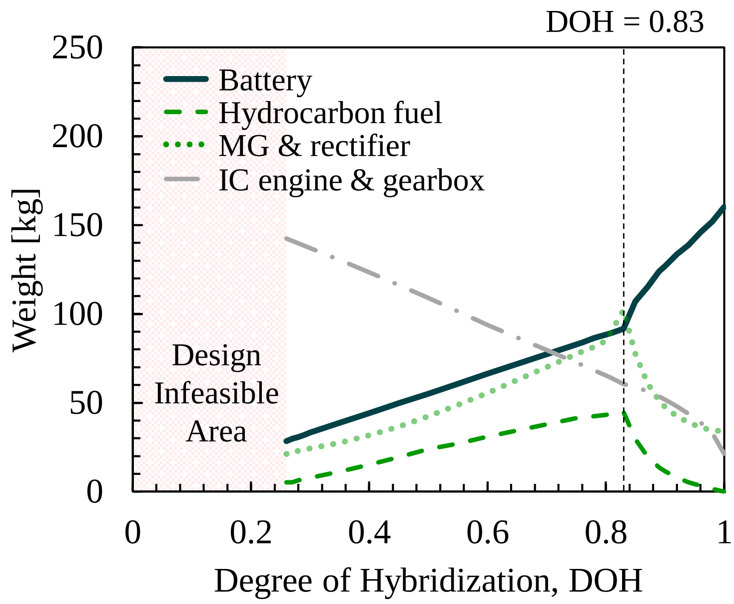

(b) Component weight vs. DOH

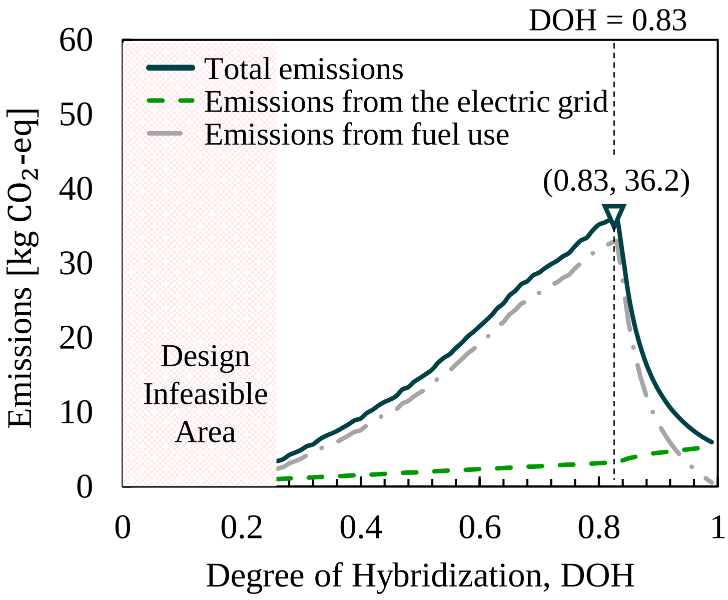

(c) Emission vs. DOH

Fig. 4-3 Sizing results of HEPS-powered VTOL aircraft vs. DOH variation (for fixed MTOW and payload)

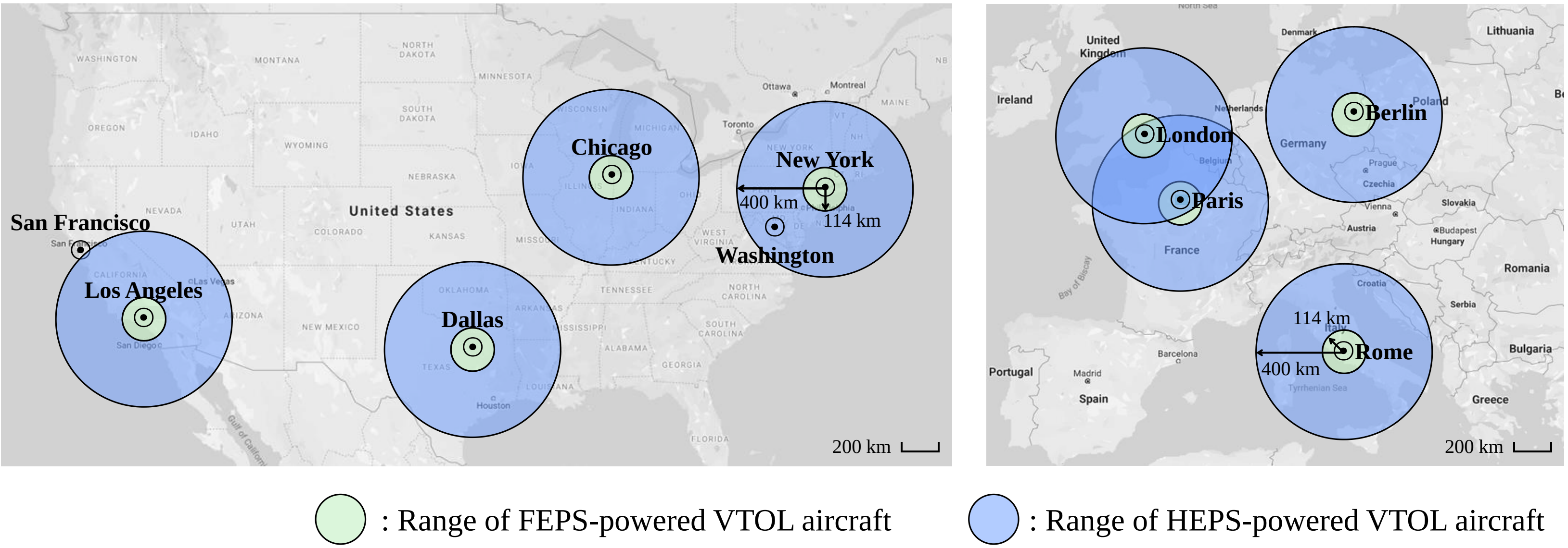

Fig. 4-4 Mission range between the FEPS- and HEPS-powered VTOL aircraft based on sizing results

4.2 Influence of EPS modeling approach types for eVTOL aircraft design

4.2.1 Problem definition

The design methodology using the enhanced EPS modeling approach in Chapter 2.3 can reliably consider the electrical characteristics of the involved electrical devices, including the PMSM operation control strategy, the battery voltage drops, and changes in the EPS efficiency depending on the operating conditions. From the perspectives of analysis and design, a comparative study was conducted to demonstrate the capabilities of the enhanced EPS modeling approach, referred to as Approach 2. The EPS modeling approaches used in the comparative study are as follows:

a) *Approach 1 (low-fidelity)*: This is the most straightforward approach used to analyze and design an EPS, involving little consideration of the electrical characteristics. It assumes that the efficiency coefficients of the electrical devices are constant throughout a given mission and cannot reflect the specifications of each component when sizing the EPS.

b) *Approach 2 (high-fidelity)*: This approach reflects the electrical characteristics in the analysis process using an equivalent circuit and semi-empirical models. Furthermore, additional modules, such as those for calculating the number of battery cells and regression models for a scalable EPS, are embedded in the design process. The battery weight is estimated from the total battery capacity to conduct a comparative study under the same design conditions as in Approach 1. Table 1 summarizes the design conditions for both approaches.

The additional design conditions used in the comparative study are summarized as follows:

a) eVTOL aircraft concept: The lift+cruise type with two types of propulsion devices (lift-DP and propeller) was selected as the eVTOL aircraft concept (Fig. 3-4). As part of this concept, 12 motor inverter pairs were used for the lift-DPs, and a single motor inverter pair was used for the pusher-type propeller. The objective of the comparative study was to investigate the response to changes in motor and inverter sizes while varying the drive system type (direct or indirect) and the gear ratio of the eVTOL aircraft. The geometric data and design parameters are detailed in Appendix B.

b) *Mission profile*: As in Chapter 4.1, a simplified Uber Elevate mission profile (Fig. 3-5) was adopted for the comparative study.

Table 4-1 Design conditions used for the two approaches in the comparative study

Type	Component	Design conditions (analysis/sizing)	
Approach 1 (low-fidelity)	Motor	Constant efficiency coefficient [58] ✓ 0.95 for the propeller, 0.88 for lift-DP	Specific power, 6 kW/kg [92] ✓ $P_{\mathrm{cr,mot}}$ calculated considering the most extreme mission
	Inverter	Constant efficiency coefficient [58] ✓ 0.98 for the propeller, 0.98 for lift-DP	Specific power, 12 kW/kg [92]
	Battery	Energy in a box	Specific energy, 300 Wh/kg [58]
Approach 2 (high-fidelity)	Motor	Equivalent circuit with control strategies ✓ Regression models based on datasheets for EMRAX motors ✓ Iron loss assumed to be 1.5% of the mechanical power [93]	Specific power, 6 kW/kg [92] ✓ $P_{\mathrm{cr,mot}}$ calculated considering PMSM specifications as well as the most extreme mission
	Inverter	Switching and conduction loss models ✓ f_{sw} = 10 kHz [78] and T_{vj} = 75 °C ✓ Regression models based on datasheets for Infineon dual inverters	Specific power, 12 kW/kg [92]
	Battery	Near-linear discharge model ✓ Battery type assumed to be Samsung INR18650-30Q	Specific energy, 300 Wh/kg [58]

4.2.2 Mission analysis results

For a given mission profile, the lift+cruise eVTOL aircraft performs hovering, takeoff, and landing in VTOL flight mode using the lift-DPs as well as other mission segments in cruising mode using the propellers. Fig. 4-5 shows the mission analysis results under the design condition of the direct drive type, with bars representing mechanical power $P_{\mathrm{mech}}(=\tau_{\mathrm{mech}}\times\omega_{\mathrm{mech}})$ and lines representing efficiency η. For Approach 1, although the calculated P_{mech} values varied with the mission segment, $\eta_{\mathrm{sys,Approach1}}$ remained constant at 0.87 in cruising mode and 0.80 in VTOL mode. By contrast, $\eta_{\mathrm{sys,Approach2}}$ displayed different values for each mission segment: 0.87–0.89 in cruising mode and 0.79–0.81 in VTOL mode.

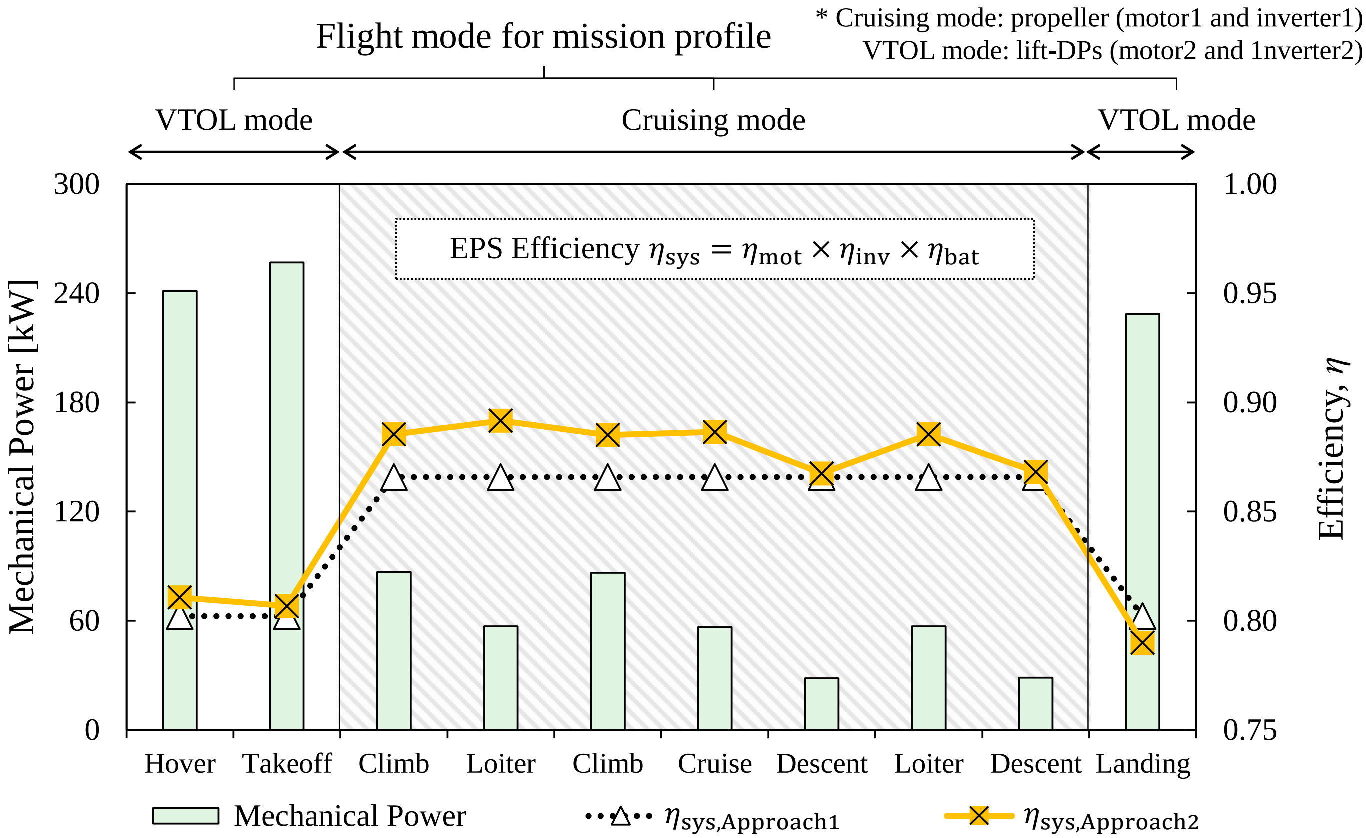

Fig. 4-5 Mission analysis results: mechanical power and EPS efficiency.

The mission analysis results were elaborated at the electrical device level to investigate their variation from the perspective of the EPS components, as shown in Fig. 4-6. Firstly, $\eta_{\mathrm{mot1,Approach2}}$ was varied from 0.898 to 0.936 and despite the smallest P_{mech}, the descent segment had the lowest efficiency in cruising mode. $\eta_{\mathrm{mot2,Approach2}}$ in the VTOL mode was estimated to be 0.950, approximately the best in class. As such, η_{mot} in a mission is determined by the location of the operating point on the efficiency map (Fig. 4-7).

From Fig. 4-7, sized motors (motor 1: 166 kW class, motor 2: 43 kW class) were operated with MTPA control. The optimal regions were $300 \leq \tau_{\mathrm{mot1}} \leq 376$ and $2200 \leq \omega_{\mathrm{mot1}} \leq 6188$ for motor 1 and $55 \leq \tau_{\mathrm{mot2}} \leq 65$ and $1740 \leq \omega_{\mathrm{mot2}} \leq 5130$ for motor 2. In the climb, cruise, and loiter mission segments, the operating points of motor 1 were near the optimal region. However, they were far from the optimal region in the descent mission segment due to the low motor torque (ca. 123 Nm). Therefore, $\eta_{\mathrm{mot1,Approach2}}$ in the descent mission segment was calculated as 0.898, which was the lowest value throughout the mission profile. The lift-DP motor performed hovering, takeoff, and landing with a maximum efficiency of 0.950 since all operating points were located within the optimal region.

Although $\eta_{\mathrm{inv,Approach2}}$ hardly changed for the mission segments, the difference in efficiency according to inverter size was remarkable ($\eta_{\mathrm{inv1,Approach2}}$ and $\eta_{\mathrm{inv2,Approach2}}$); $\eta_{\mathrm{inv2,Approach2}}$ was approximately 0.93, about 5% point lower than $\eta_{\mathrm{inv1,Approach2}}$. This result was attributable to the constraint used in inverter sizing that V_{CES} must be higher than V_{DC} to ensure inverter durability. A parallel connection to the battery pack provided V_{DC} equally to the inverters, so inverter 2 must be oversized in terms of voltage to satisfy the V_{CES}-related constraint, even if it is sized with a smaller I_{cn} than inverter 1. Due to this, inverter 2 was significantly less efficient than inverter 1. $\eta_{\mathrm{bat,Approach2}}$ tended to be inversely proportional to the shaft power because the copper loss of the battery is linearly related to the output current. In addition, the voltage drop due to incremental DD increases the cell current and accelerates battery consumption. This also caused $\eta_{\mathrm{bat,Approach2}}$ to be lowest in the landing mission segment, even if the shaft power during takeoff is lower than that during landing.

Furthermore, the electrical characteristics of each component (the operating condition of motors, oversizing of inverter 1, and acceleration of battery consumption) also affect the maximum power loss, as shown in Fig. 4-6 (b). $\left(P_{\mathrm{loss,total}}\right)_{\mathrm{max}}$ was obtained similar to Approaches 1 and 2; however, $\left(P_{\mathrm{loss,comp}}\right)_{\mathrm{max}}$ constituting $\left(P_{\mathrm{loss,total}}\right)_{\mathrm{max}}$ was calculated differently. This difference is expected to increase according to the design requirements, such as the assumptions used for each electrical device, aircraft concept, and mission profile.

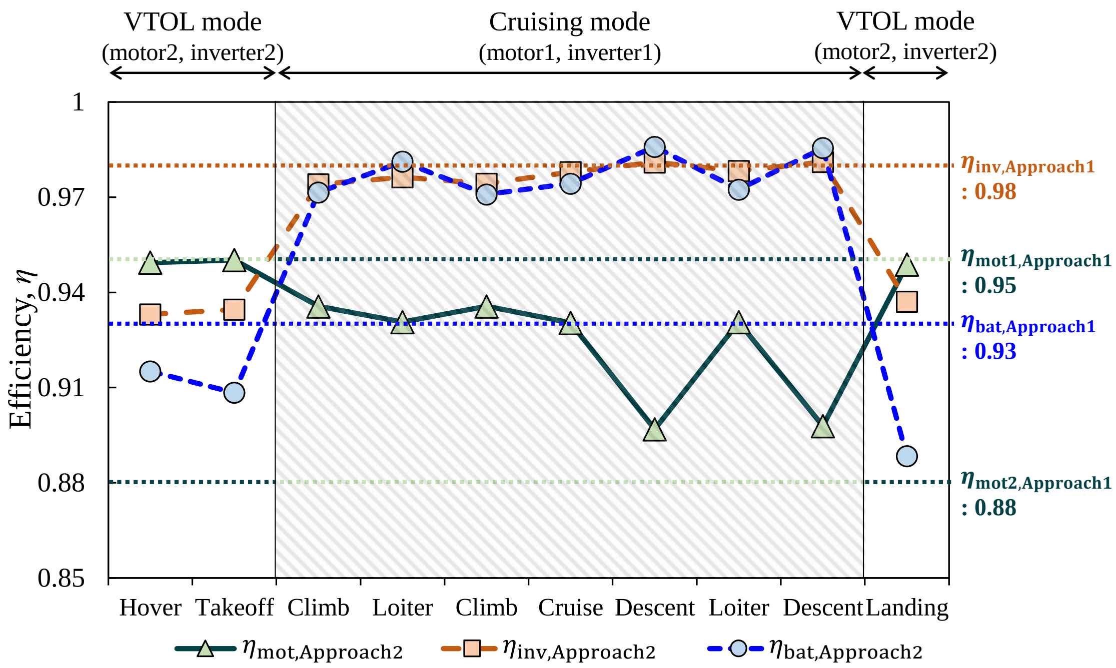

(a) Efficiency for electrical device level

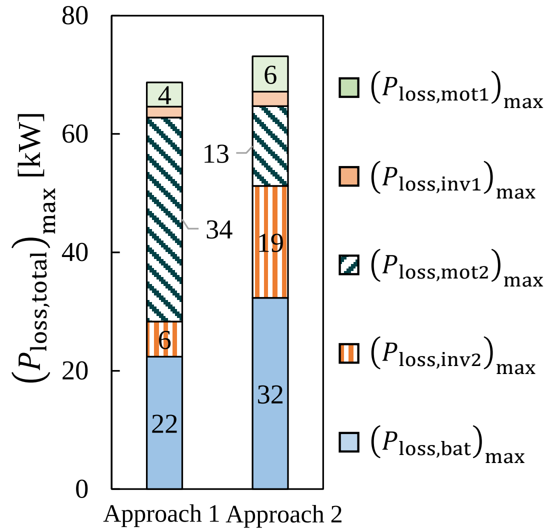

(b) Maximum power losses

Fig. 4-6 Mission analysis results: efficiency at the electrical device level.

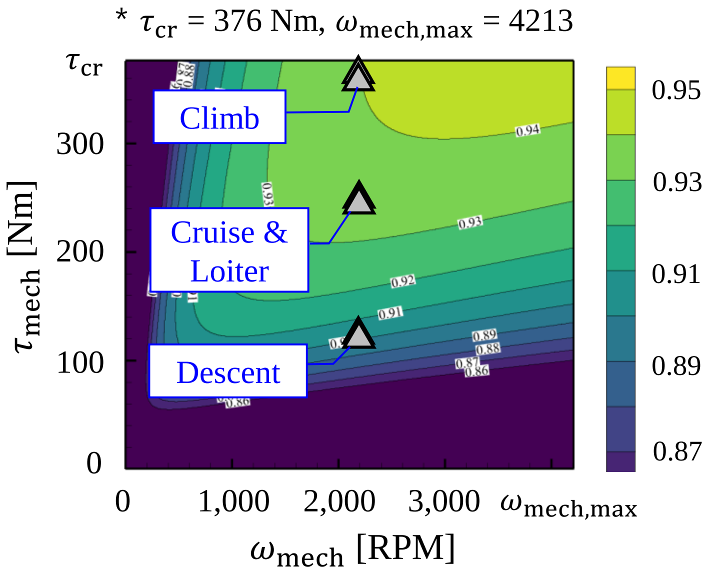

(a) Motor 1 (propeller)

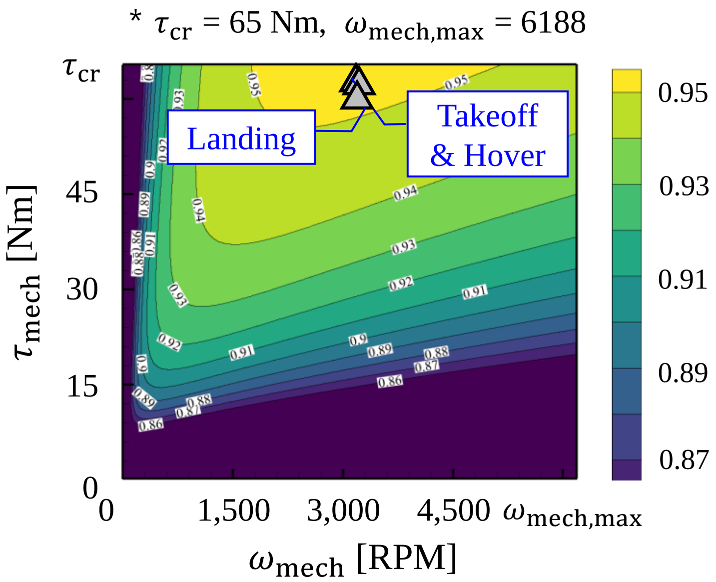

(b) Motor2 (12 lift-DPs)

Fig. 4-7 Efficiency maps for the sized motors.

Another comparative study of the mission analysis was performed while changing the drive system type (direct or indirect) and gear ratio, where an increase in the gear ratio is equivalent to a decrease in the size of the motor inverter pair [Eq. (2-33)]. Fig. 4-8 shows the changes in $\eta_{\mathrm{mot,Approach2}}$ and $\eta_{\mathrm{inv,Approach2}}$ for various drive system types, gear ratios, and motor inverter pair sizes. The size change of the motor according to the drive type and gear ratio did not significantly alter the motor efficiency map, although it did affect the motor operating point. Since a reduction gear serves as a torque amplifier, the motor must operate at a rotational speed increased by the gear ratio to obtain the thruster's required rotational speed. By increasing the gear ratio, the operating point on the motor efficiency map shifts to the right, resulting in a decrease in motor efficiency. This effect was observed in the descent mission segment, which requires the lowest mechanical torque among the mission segments in the motor efficiency map. Therefore, $\eta_{\mathrm{mot,Approach2}}$ tended to decrease with increasing gear ratio. For the inverter, $\eta_{\mathrm{inv2,Approach2}}$ tended to increase as inverter 2 was scaled up because this component was gradually sized to fit $V_{\mathrm{DC,max}}$. Therefore, the change in efficiency depending on the size of the motor inverter pair as well as the drive system type and gear ratio may be significant, and Approach 2 presented in this study can be applied to EPS analysis for obtaining more reliable results.

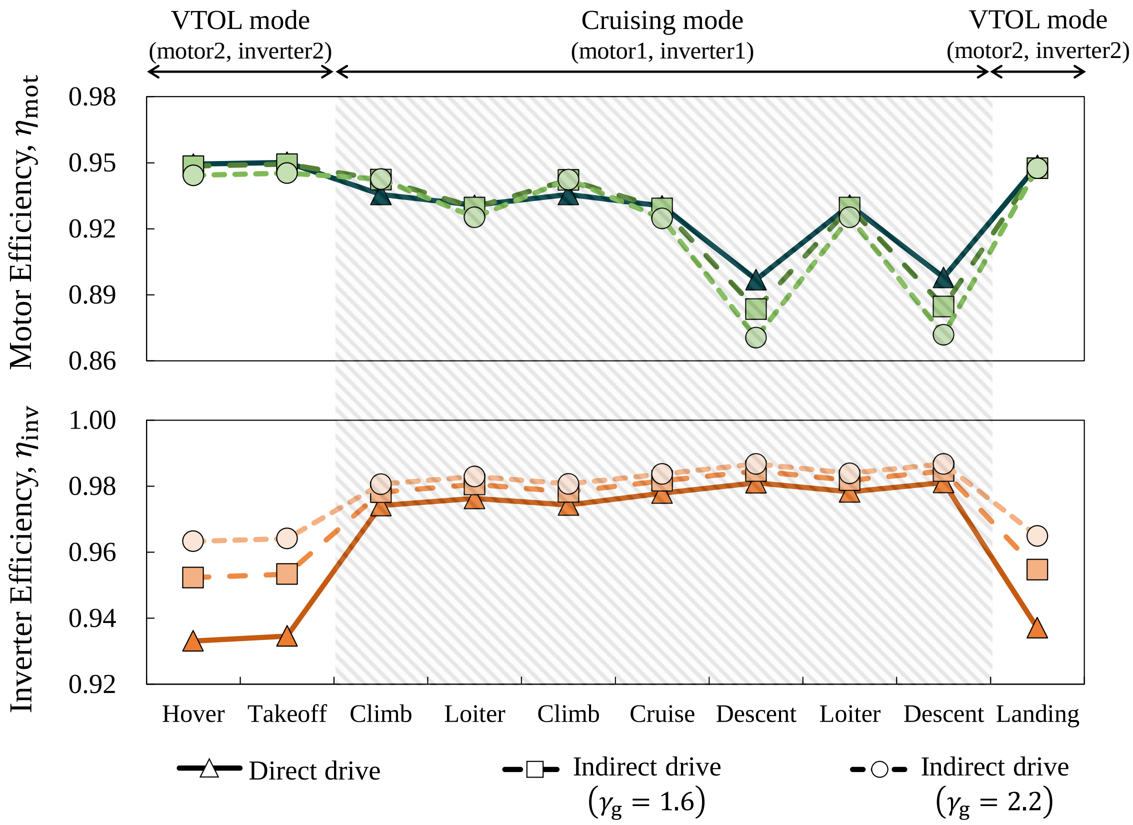

Fig. 4-8 Efficiencies of motors and inverters upon varying the drive system type and gear ratio.

4.2.3 eVTOL aircraft sizing results

A concept of available payload weight $W_{\mathrm{payload,av}}$ is introduced to compare the sizing results for Approaches 1 and 2. $W_{\mathrm{payload,av}}$ indicates the amount of payload available for loading in the following manner:

$$W_{\mathrm{payload,av}} = W_{\mathrm{MTOW,baseline}} - W_{\mathrm{empty}} - W_{\mathrm{bat}} \tag{4-2}$$

where $W_{\mathrm{MTOW,baseline}}$ is the maximum takeoff weight (MTOW) of the sized lift+cruise eVTOL aircraft for two passengers (payload weight: 182 kg) in Approach 1 and W_{empty} denotes the empty weight. The purpose of fixing the MTOW to $W_{\mathrm{MTOW,baseline}}$ is to conduct aerodynamic analysis under the same loads regardless of the design conditions (drive system type and gear ratio). Table 4-2 summarizes the sizing results based on a $W_{\mathrm{MTOW,baseline}}$ of 1004 kg obtained through eVTOL aircraft sizing and changes in design conditions.

Prominent differences are observed in the motor, inverter, and TMS when comparing the sizing results of Approaches 1 and 2. Although the weight of motor inverter pairs was estimated using $P_{\mathrm{cr,mot}}$ in both cases, there was a difference in the Approach used. For calculating $P_{\mathrm{cr,mot}}$ in Approach 1, the designer uses τ_{mech} and ω_{mech} for the most extreme mission. By contrast, in Approach 2, the designer calculates $P_{\mathrm{cr,mot}}$ considering $\omega_{\mathrm{mech,max}}$ from the regression model for the motor specification. The gap between $\omega_{\mathrm{mech,max}}$ obtained for the most extreme mission and that derived from the specification regression model narrows with increasing gear ratios (Fig. 4-9). That is, the reduction gear enables designers to select an appropriate motor by matching the torque with the mechanical rotational speed required for a particular mission profile. This result appears only in Approach 2, which obtains $\omega_{\mathrm{mech,max}}$ from the regression model. In view of the analysis results in Chapter 4.2.2, since each component in Approach 1 has a constant efficiency, the maximum power loss remains constant regardless of the size of the motor or inverter. By contrast, in Approach 2, η_{mot} and η_{inv} change with the motor and inverter size. Based on the sum of these power losses, Approaches 1 and 2 produce different results with respect to TMS sizing.

Based on the calculated available payload for Approach 2, the eVTOL aircraft designed with this approach must be scaled up to accommodate two passengers, which is a design requirement. Using the sizing loop mentioned in Sec. II, the calculated MTOW values for two passengers, were 1674 kg (direct) and 1058 kg (indirect with γ_{gb} = 2.2). This means that the MTOW and the aircraft dimensions based on the wingspan with equivalent wing loading decreased by 37% and 20%, respectively, upon finding the appropriate drive system and gear ratio. The differences in analysis and design results may decrease or increase depending on the assumptions and datasheets used; however, only Approach 2 allows for changes in EPS efficiency and a more realistic sizing result based on the drive system type and gear ratio, which could not be achieved with Approach 1.

Table 4-2 Summary of the sizing results

	EPS Modeling type	Approach 1 (low-fidelity)			Approach 2 (high-fidelity)					
	Drive system type	Direct	Indirect ($\gamma_{gb} = 1.6$)	Indirect ($\gamma_{gb} = 2.2$)	Direct	Indirect ($\gamma_{gb} = 1.6$)	Indirect ($\gamma_{gb} = 2.2$)	Direct	Indirect ($\gamma_{gb} = 1.6$)	Indirect ($\gamma_{gb} = 2.2$)
Weight [kg]	W_{MTOW}			1004			1004	1674	1221	1058
	W_{empty}	625	642	643	735	678	637	1207	1039	683
	W_{SG}	291	291	291	291	291	291	472	350	305
	W_{gb}	-	17	18	-	22	19	-	27	21
	W_{mot}	64	64	64	121	85	67	219	105	73
	W_{inv}	32	32	32	64	45	35	116	55	38
	W_{TMS}	101	101	101	108	92	89	184	120	97
	W_{other}	145	145	145	162	150	145	216	165	149
	W_{bat}	189	189	189	186	185	185	285	217	193
	$\boldsymbol{W_{payload,av}}$	**182** (2 pax)	**165**	**164**	**72**	**134**	**173**			**182** (2 pax)

Max. power losses [kW]	$P_{loss,m1}$	4	4	4	6	5	5	10	7	6
	$P_{loss,inv1}$	2	2	2	2	2	2	3	2	2
	$P_{loss,m2}$	34	34	34	13	13	14	27	17	14
	$P_{loss,inv2}$	6	6	6	19	11	9	30	16	10
	$P_{loss,bat}$	22	22	22	32	31	31	54	40	34
	$\boldsymbol{P_{loss,total}}$	**69**	**69**	**69**	**73**	**62**	**60**	**125**	**82**	**66**
Etc.	N_{series} / $N_{parallel}$	**-**	**-**	**-**	**93 / 54**	**67 / 75**	**54 / 93**	**142 / 54**	**76 / 78**	**56 / 93**
Aircraft dimension [m]		**11.0**	**11.0**	**11.0**	**11.0**	**11.0**	**11.0**	**14.2**	**12.1**	**11.3**

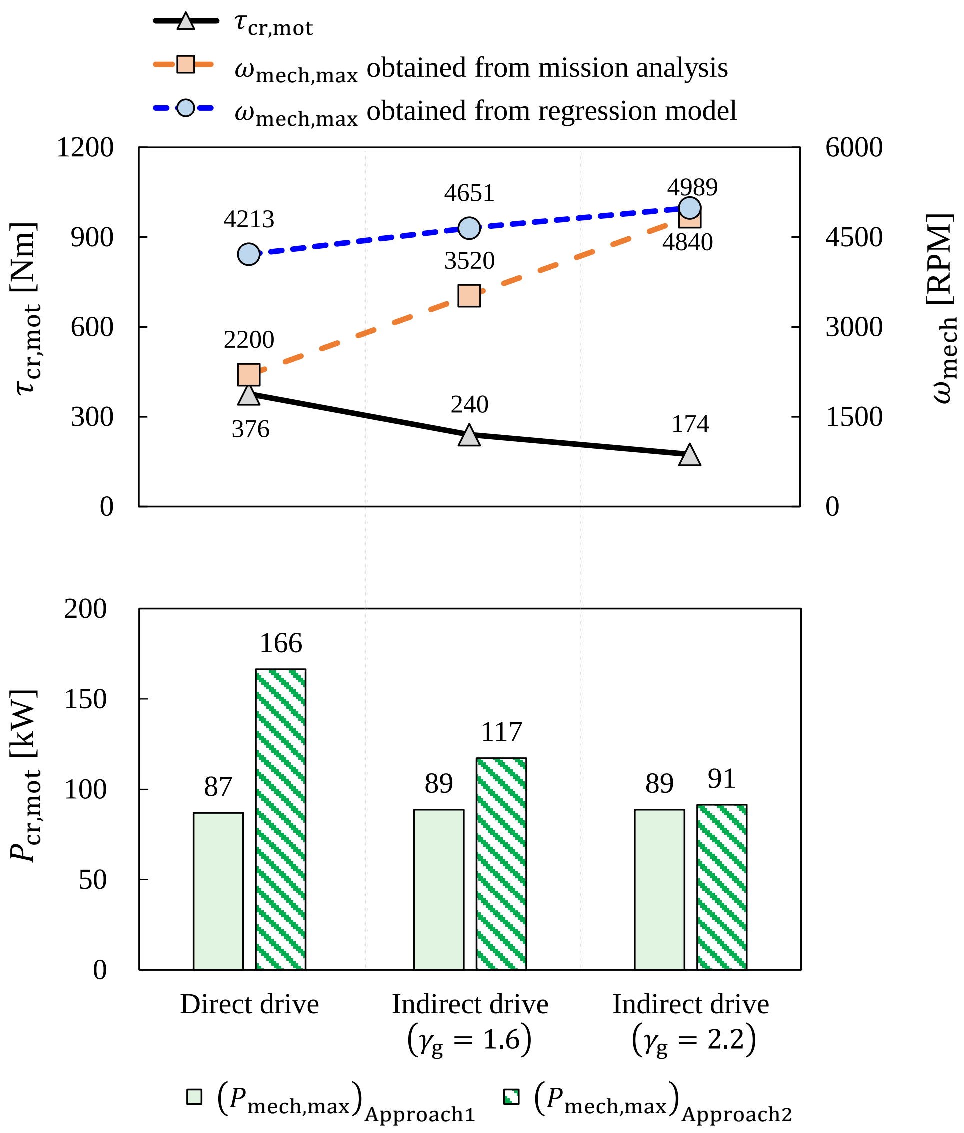

Fig. 4-9 Differences based on the EPS modeling approach type for obtaining the continuous rated power of the motor.

4.3 Design optimization considering noise mitigation

4.3.1 Problem definition

The comparative study in Chapter 4.2 revealed changes in the type of drive system (direct or indirect) and gear ratio significantly impacted EPSs' efficiency and size. This chapter details design optimization performed using enhanced EPS modeling and noise analysis based on the sizing results presented in Chapter 4.2.3. Baseline aircraft are indirect-driven eVTOL aircraft with a gear ratio of 1.6.

MTOW is a vital parameter for comparing the performance of aircraft. Therefore, minimizing MTOW was set as a single objective under the condition of the payload of 182 kg and the same mission profile (Fig. 3-5).

The optimization problem is as follows:

Objective (1):

Minimize Maximum takeoff weight (kg), MTOW

Constraints were imposed on noise mitigation, structural safety, and design feasibility to achieve realistic design results. The noise constraint was set as the quantitative criteria of $L_{\mathrm{A,max}}$ 62 dBA at 150 m, suggested in Uber Elevate[xiv]. The structural safety constraint was established on the supporting rod used for lift-DP. To consider design feasibility, the sizes of lift-DP, wing, and supporting rod were set as geometric constraints to secure space for lift-DP.

Constraints (3):

$L_{\mathrm{A,max}} \leq \left(L_{\mathrm{A,max}}\right)_{\mathrm{limit}}$ for the noise mitigation

$\sigma_{\mathrm{max}} \leq \sigma_{\mathrm{allow}}$ for the structural safety of supporting rods

$R \leq R_{\mathrm{limit}},\ b \leq b_{\mathrm{limit}},\ l \leq l_{\mathrm{limit}}$ for the design feasibility

Design variables related to the aircraft's configuration and performance, such as DPs' radius, chord length, and wingspan, were used for design optimization. These are summarized as follows:

Design variables (12):

$R, c, \theta_0, \theta_{\mathrm{tw}}$ for lift-DPs

b, θ_0, AR for the main wing

$R, c, \theta_{\mathrm{tw}}, RPM$ for the propeller

l_{rod} for the supporting rods

Table 4-3 Design spaces for each design variable

Design Variable		Upper bound	Baseline	Lower bound
Lift-DPs	R	0.87	0.67	0.50
	c	0.26	0.21	0.16
	θ_0	25.0	13.5	10.1
	θ_{tw}	0	0	-13.5
Main wing	b	15.1	12.1	9.1
	θ_0	15.5	12.4	9.3
	AR	14.3	11.4	8.6
Propeller	R	1.3	1.07	0.8
	c	0.14	0.11	0.08
	θ_{tw}	-11.3	-15.0	-18.8
	RPM	2750	2200	1650
Supporting rods	l_{rod}	3.45	2.76	2.07

Additionally, a non-gradient-based method, an evolutionary algorithm, was used as the optimal design technique. The optimization was terminated when the convergence tolerance of the objective function was calculated within a range of 1% during 1000 consecutive times, and the maximum number of evaluations was 5000.

4.3.2 Design optimization

According to the presence of noise constraint, two types of optimal design results were obtained—OPT1: without noise constraint, OPT2: with noise constraint. The optimization results are summarized in Fig. 4-10 and Table 4-4. In Fig. 4-10, both cases converged around run number 4000. It has been estimated that OPT2 is 1096 kg, which is 9% heavier than OPT1 without considering the noise constraint. However, the noise prediction result of OPT1 is 76.3 dBA, which is 14 dBA higher than $(L_{\mathrm{A,max}})_{\mathrm{limit}}$ and even about 5 dBA higher than $(L_{\mathrm{A,max}})_{\mathrm{baseline}}$. It means that MTOW minimization and noise mitigation are challenging to achieve together in eVTOL aircraft design.

As explained in Chapter 2.3.1, motor sizing is determined by the continuous rated torque. Since it is advantageous for the motor to design a lift-DP that operates at low torque and high rotational speed as the target, the lift-DPs' radius of OPT1 is 0.6m, smaller than that of the baseline. It should be noted, however, that because the lift-DPs' tip speed significantly impacts the noise generated by rotary-wing systems, the design of lift-DPs for noise mitigation tends to reduce the tip speed. Furthermore, since the lift-DPs' radius is increased to increase disc loading, the lift-DPs are designed from an aeronautical perspective to produce high torque at a low rotational speed. In addition, the wingspan, the wing's aspect ratio, and the support rod's length are increased to ensure a reduced clearance (i.e., the gap between the lift-DP and between the lift-DP and the wing) due to the increased rotor size. The supporting rod is designed to satisfy structural safety.

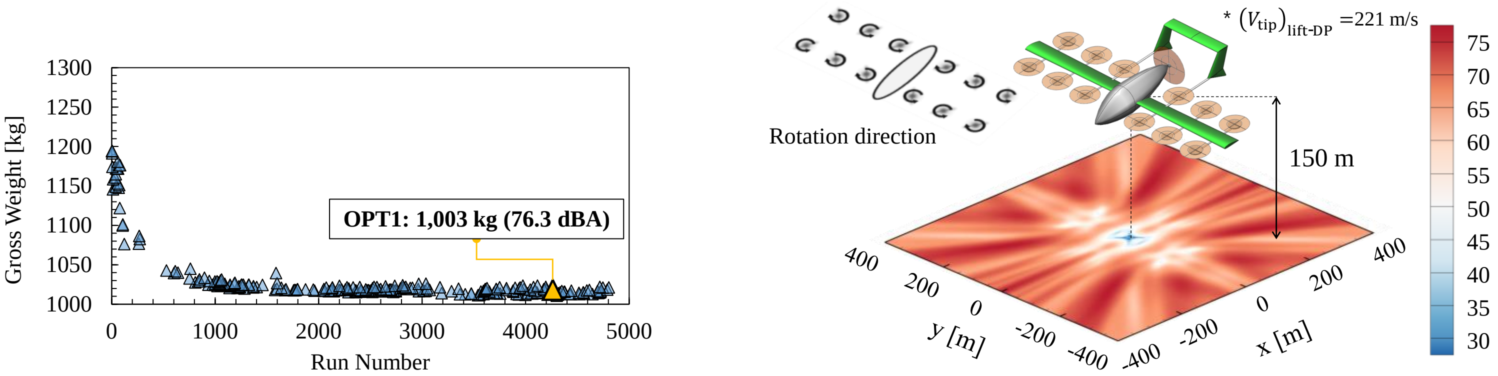

(a) Design optimization results without the noise constraint

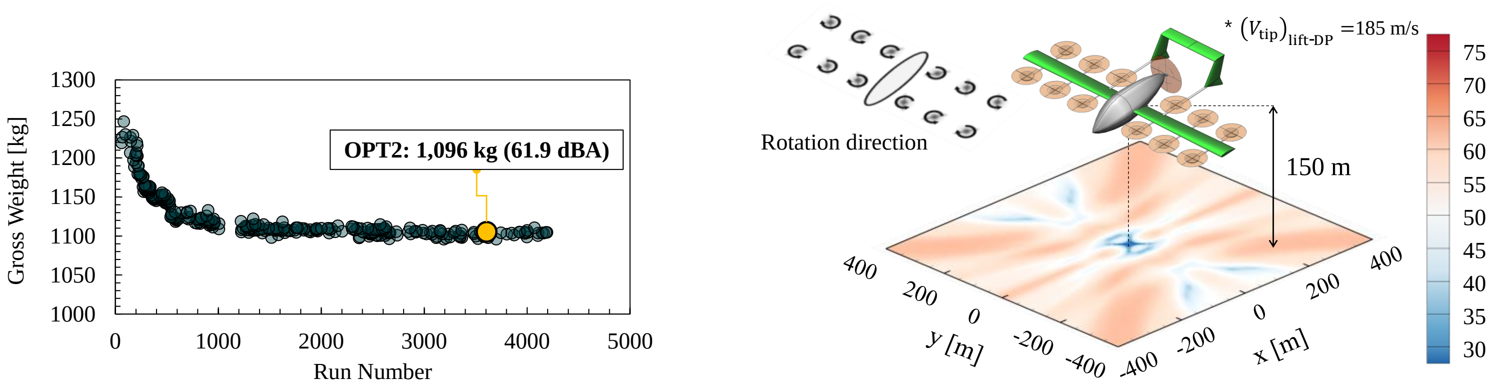

(b) Design optimization results with the noise constraint

Fig. 4-10 Design optimization results: Convergence history and noise contour.

Table 4-4 Design optimization results: Objective function, design variables, and noise prediction value.

	MTOW [kg]	Lift-DP				Wing			Thruster for cruise				Etc.	Max. SPL [dBA]
		R [m]	c [m]	θ_0 [°]	θ_{tw} [°]	b [m]	θ_0 [°]	AR	R [m]	c [m]	θ_{tw} [°]	V_{tip} [m/s]	l_{rod} [m]	
Baseline	1,221	0.67	0.21	13.5	0	12.1	12.4	11.4	1.07	0.11	-15.0	247.0	2.76	71.6
OPT1	1,003	0.60	0.17	20.8	-10.3	9.6	13.1	13.2	1.07	0.11	-16.0	260.3	2.18	76.3
OPT2	1,096	0.68	0.16	24.2	-10.6	10.6	11.7	13.6	1.13	0.11	-17.9	264.5	2.49	61.9

When analyzing the design results in Fig. 4-11 in terms of weight, the changes in the geometric configuration have little effect on the weight of the structure groups (e.g., fuselage and wing). Furthermore, the components that changed the most depending on the design conditions are those related to the EPS. It is confirmed that the motor sizing results dependent on the lift-DP's torque and rotational speed range had a significant influence on the overall design of the FEPS-powered VTOL aircraft. Due to the fact that optimal motor design and noise mitigation have a trade-off relationship, both fields should be considered jointly when designing new eVTOL AAM vehicles.

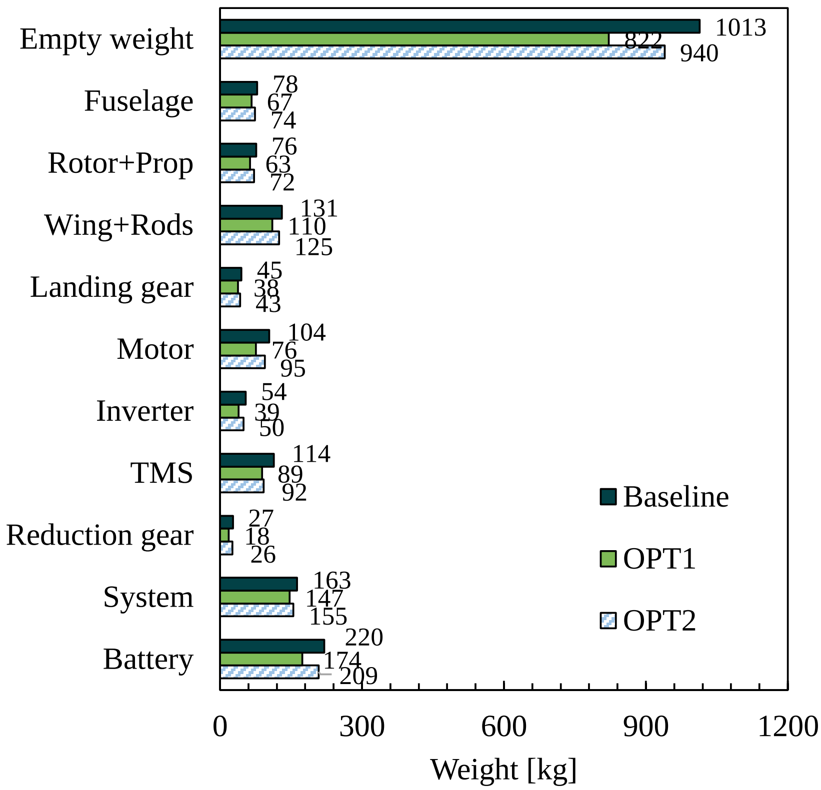

Fig. 4-11 Weight breakdown of design optimization results.

Chapter 5.

Conclusion

5.1 Summary

In this study, a generic design methodology that considers eVTOL AAM vehicles' characteristics is developed. This design methodology comprises five modules—flight analysis, propulsion system sizing, mission analysis, weight estimation, and noise prediction—that can consider the diversity of configurations, flight mechanisms, EPS architectures, and performance assessment, including noise prediction. First, the comprehensive flight-analysis module is created by assembling component-analysis methods, including the shrouded rotor and DP. The proposed flight analysis allows for analysis of the configurations and flight mechanisms of various types of VTOL aircraft—wingless, vectored-thrust, and lift+cruise. In addition, the scope of propulsion system sizing, mission analysis, and weight estimation has been expanded to include not only FEPS but also various HEPSs (series, parallel, and series-parallel). Using the Farassat 1A formulation with compact loading models, it is possible to predict the thickness and load noise of eVTOL aircraft at the conceptual design stage.

Also, this study proposes a novel EPS modeling for FEPS-powered VTOL aircraft conceptual design by considering the electrical characteristics of each electrical device in a more accurate manner. To this end, three modules are developed for motor, inverter, and battery analysis. These modules can manage multiple electrical characteristics, including the PMSM operation control strategy, battery voltage drops, and changes in the EPS efficiency depending on the operating conditions. First, the motor analysis module is developed using the PMSM equivalent circuit with the MTPA control strategy suitable for the high-load condition of aircraft propulsion. Second, the inverter analysis module is constructed by considering the switching and conduction losses, which vary depending on the inverter voltage and current. Third, the battery analysis module is established using a near-linear discharge model to consider the voltage drop. Furthermore, additional modules, such as those for calculating the battery stack in series and parallel, as well as regression models for the motor and inverter parameters and consideration of the drive system type (direct or indirect, including a reduction gear), are incorporated into the proposed design methodology for eVTOL aircraft.

In addition, three types of applications are performed to demonstrate the necessity and capability of the proposed numerical methods for eVTOL conceptual design. In the first application, a comparative study is performed to demonstrate performance variations after replacing a FEPS with a HEPS. The results show that an optimal DOH exists in the region where the battery-sizing standard changes from the discharge C-rate to the total energy. And If the IC engine is sized for cruise power, and batteries provide any power requirement beyond that, then HEPS operates under optimal conditions. Therefore, HEPS can extend the range of FEPS-powered aircraft more than four times with optimal conditions. This implies that HEPS-powered

VTOL aircraft possess the potential to perform intercity missions, as well as international missions until battery technology is enhanced enough.

In the second application, it is confirmed that the ability of the enhanced EPS analysis method to consider the electrical characteristics allows the efficiency to be estimated according to the operating conditions and drive system type. And an indirect drive system with a reduction gear optimally matches the required mechanical rotation speed and torque for a given mission profile, allowing designers to select a suitably sized motor. It means that the enhanced EPS analysis method significantly influences the MTOW and dimensions in eVTOL aircraft conceptual design, as well as selecting the appropriate drive system type.

Lastly, the final application is to investigate the influence of noise prediction on the design optimization of an eVTOL aircraft. It is identified that the motor sizing results dependent on the lift-DP's torque and rotational speed range had a significant influence on the overall design of the FEPS-powered VTOL aircraft. Since optimal motor design and noise mitigation have a trade-off relationship, both fields should be considered jointly when designing new eVTOL AAM vehicles.

5.2 Originality of the thesis

The originality contribution of the thesis can be summarized as follows:

a) The proposed design methodology has a generality that can handle various existing and future AAM vehicle concepts. Based on this advantage, it is possible to compare various eVTOL AAM vehicle concepts under the same design requirements, enabling the successful design of new eVTOL AAM vehicles to be explored in advance. Moreover, the algorithm for this method would still possess generality even if a higher fidelity analysis module replaces the existing counterpart. The designer can therefore combine existing analysis tools onto the proposed design method easily.

b) The enhanced EPS modeling complements the reliability of EPS design and analysis, which was relatively low in accuracy compared to other disciplines, allowing all fields considered in the concept design of eVTOL aircraft to have a similar level of fidelity. This advantage adds adequacy to the conceptual design results of eVTOL AAM vehicles. In addition, this enhanced EPS modeling approach allows designers to select a suitably sized motor according to the drive system type and gear ratio. Finally, both motor design and noise mitigation can be considered jointly when designing new eVTOL AAM vehicles.

5.3 Recommendations for future work

In this study, a design methodology with a high degree of generality and accuracy for eVTOL aircraft has been developed, but there is still room for further improvement in the following areas.

First, the TMS sizing in this study was conducted simply by calculating the sum of the power losses in each component. Since many industries and governments emphasize the importance of thermal constraint for eVTOL aircraft design [94–97], more accurate physics-based TMS modeling is required. To this end, the design methodology should be modified to incorporate improved thermal subsystem models, such as the heat sink model [98].

Second, fuel cell-based HEPS has received new attention as a potential propulsion system for eVTOL AAM aircraft. However, studies conducted so far have focused solely on incorporating fuel-cell-based HEPS architecture into aircraft designs without considering electrical characteristics [99–102]. Hence, it seems worthwhile to incorporate the enhanced EPS modeling approach presented in this study and additional electrical characteristics, such as the electrochemical reaction of the fuel cell stack and the power dissipation of the DC-DC converter, into the eVTOL aircraft conceptual design.

Lastly, for the industry to realize eVTOL aircraft, off-design scenarios, such as potential regulatory performance requirements, and methods to meet maintenance costs for the EPS must be considered. These requirements should be considered to design more realistic eVTOL AAM vehicles in the near future.

References

[1] Vv. Aa., “Aircraft Technology Roadmap to 2050,” *Tech. Rep.*, International Air Transport Association, 2019, pp. 1–51.

[2] M. Gill, “Aviation Benefits Beyond Borders,” *Tech. Rep.*, Air Transport Action Group, 2018, pp. 1–88.

[3] ICAO, Environmental Report 2016, Aviation and climate change, 2016.

[4] Rendón, M. A., Sánchez R., C. D., Gallo M., J., and Anzai, A. H., “Aircraft Hybrid-electric Propulsion: Development Trends, Challenges and Opportunities,” *Journal of Control, Automation and Electrical Systems*, Vol. 32, 2021, pp. 1244–1268.

[5] Bradley, M. K., and Droney, C. K., “Subsonic Ultra Green Aircraft Research Phase II: N 4 Advanced Concept Development,” NASA CR-2012-217556, Huntington Beach, CA, 2012.

[6] Goyal, R., Reiche, C., Fernando, C., and Cohen, A, “Advanced Air Mobility: Demand Analysis and Market Potential of the Airport Shuttle and Air Taxi Markets,” *Sustainability*, Vol. 13, No. 13, 2021, Paper 7421. https://doi.org/10.3390/su13137421

[7] Cohen, A., Shaheen, S., and Farrar, E., “Urban Air Mobility: History, Ecosystem, Market Potential, and Challenges,” *IEEE Transactions on Intelligent Transportation Systems*, Vol. 22, No. 9, 2021, pp. 6074–6087. https://doi.org/10.1109/TITS.2021.3082767

[8] Patterson, M. D., Antcliff, K. R., and Kohlman, L. W., “A Proposed Approach to Studying Urban Air Mobility Missions Including an Initial Exploration of Mission Requirements,” *AHS International 74th Annual Forum & Technology Display*, Phoenix, AZ, May 2018, pp. 1–19.

[9] Reiche, C., Goyal, R., Cohen, A., Serrao, J., Kimmel, S., Fernando, C., and Shaheen, S., “Urban Air Mobility Market Study,” NASA, Washington, DC, USA, Tech. Rep. HQ-E-DAA-TN63717, 2018. https://doi.org/10.7922/G2ZS2TRG

[10] Hirschberg, M. J., "The Electric VTOL Revolution," San Francisco, USA, SA Symposium 2018, May 2018.

[11] Misra, A. "Summary of 2017 NASA Workshop on Assessment of Advanced Battery Technologies for Aerospace Applications," NASA Glenn Research Center Report GRC-E-DAA-TN51429, Document ID: 20180001539, Cleveland, Ohio, Jan. 2018, pp. 1–18.

[12] Pornet, C., Gologan, C., Vratny, P. C., Seitz, A., Schmitz, O., Isikveren, A. T., and Hornung, M., "Methodology for Sizing and Performance Assessment of Hybrid Energy Aircraft," *Journal of Aircraft*, Vol. 52, No. 1, 2015, pp. 341–352.
https://doi.org/10.2514/1.C032716

[13] Sgueglia, A., Schmollgruber, P., Bartoli, N., Benard, E., Morlier, J., Jasa, J., Martins, J. R. R. A., Hwang, J. T., and Gray, J. S., "Multidisciplinary Design Optimization Framework with Coupled Derivative Computation for Hybrid Aircraft," *Journal of Aircraft*, Vol. 57, No. 4, 2020, pp. 715–219.
https://doi.org/10.2514/1.C035509

[14] Sgueglia, A., Schmollgruber, P., Bartoli, N., Atinault, O., Benard, N., and Morlier, J., "Exploration and Sizing of a Large Passenger Aircraft with Distributed Electric Ducted Fans," *2018 AIAA Aerospace Sciences Meeting*, AIAA Paper 2018–1745, 2018.
https://doi.org/10.2514/6.2018-1745

[15] Isikveren, A. T., Pornet, C., Vratny, P. C., and Schmidt, M., "Optimization of Commercial Aircraft Using Battery-Based Voltaic-Joule/Brayton Propulsion," *Journal of Aircraft*, Vol. 54, No. 1, 2017, pp. 246–261.
https://doi.org/10.2514/1.C033885

[16] Finger, D. F., Braun, C., and Bil, C., "Comparative Assessment of Parallel-Hybrid-Electric Propulsion Systems for Four Different Aircraft," *Journal of Aircraft, Vol.57, No. 5,* 2020, pp. 843–853.
https://doi.org/10.2514/1.C035897

[17] Rizzi, S. A., Huff, D. L., Boyd, D., Bent, P., Henderson, B., Pascioni, K. A., Sargent, C., Josephson, D. L., Marsen, M., He, H., and Snider, R., "Urban Air

Mobility Noise: Current Practice, Gaps, and Recommendations," NASA TP-2020-5007433, 2019.

[18] Maurice, L., Lee, D., "Assessing Current Scientific Knowledge, Uncertainties and Gaps in Quantifying Climate Change Noise and Air Quality Aviation Impacts," *Final Report of the International Civil Aviation Organization (ICAO) Committee on Aviation and Environmental Protection (CAEP) Workshop*, US Federal Aviation Administration and Manchester Metropolitan University, Washington DC and Manchester, 2009, pp. 1–53.

[19] Krishnan, R., Bharadwaj, A. S., "A Comparative Study of Various Motor Drive Systems for Aircraft Applications," *Proceedings of the IEEE Industry Applications Society Annual Meeting*, Dearborn, MI, USA, Sept. 28–Oct. 4, 1991.
https://doi.org/10.1109/IAS.1991.178163

[20] Dorn-Gomba, L., Ramoul, J., Reimers, J., and Emadi, A., "Power Electronic Converters in Electric Aircraft: Current Status, Challenges, and Emerging Technologies," *IEEE Transactions on Transportation Electrification,* Vol. 6, No. 4, Dec. 2020, pp. 1648–1664.
https://doi.org/10.1109/TTE.2020.3006045

[21] Henke, M., Narjes, G., Hoffmann, J., Wohlers, C., Urbanek, S., Heister, C., Steinbrink, J., Canders, W. R., and Ponick, B., "Challenges and Opportunities of Very Light High-Performance Electric Drives for Aviation," *Energies*, Vol. 11, No. 2, 2018, Paper 344.
https://doi.org/10.3390/en11020344

[22] Ferreira, F. J., and de Almeida, A. T., "Overview on Energy Saving Opportunities in Electric Motor Driven Systems - Part 1: System Efficiency Improvement," *2016 IEEE/IAS 52nd Industrial and Commercial Power Systems Technical Conference (I&CPS),* Detroit, USA, May 17–20, 2016.

[23] van der Geest, M., Polinder, H., Ferreira, J. A., and Christmann, M., "Power Density Limits and Design Trends of High-Speed Permanent Magnet Synchronous Machines," *IEEE Transactions on Transportation*

Electrification, Vol. 1, No. 3, 2015, pp. 266–276.
https://doi.org/10.1109/TTE.2015.2475751

[24] Massey, S., “Modeling, Simulation and Control of Hybrid Electric Vehicle Drive while Minimizing Energy Input Requirements Using Optimized Gear Ratios,” M.S. Dissertation, Michigan Technological University, 2016.

[25] Finger, D. F., “Methodology for Multidisciplinary Aircraft Design under Consideration of Hybrid-Electric Propulsion Technology,” Ph.D. Dissertation, RMIT University, 2020.

[26] Friedrich. C., and Robertson, P.A., “Hybrid-Electric Propulsion for Aircraft,” *Journal of Aircraft*, Vol. 52, No. 1, 2015, pp. 176–189.
https://doi.org/10.2514/1.C032660

[27] Schmollgruber, P., Bedouet, J., Sgueglia, A., Defoort, S., Lafage, R., Bartoli, N., Gourinat, Y., and Benard, E., “Use of a Certification Constraints Module for Aircraft Design Activities,” *17th AIAA Aviation Technology, Integration, and Operations Conference*, AIAA Paper 2017-3762, 2017.
https://doi.org/10.2514/6.2017-3762

[28] Nakka, S. K. S., and Alexander-Ramos, M. J., “Simultaneous Combined Optimal Design and Control Formulation for Aircraft Hybrid-Electric Propulsion Systems,” *Journal of Aircraft*, Vol. 58, No. 1, 2021, pp. 53–62.
https://doi.org/10.2514/1.C035678

[29] Isikveren, A. T., “Method of Quadrant-Based Algorithmic Nomographs for Hybrid/Electric Aircraft Predesign,” *Journal of Aircraft*, Vol. 55, No. 1, 2018, pp. 396–405.
https://doi.org/10.2514/1.C034355

[30] de Vries, R., Brown, M., and Vos, R., “Preliminary Sizing Method for Hybrid-Electric Distributed-Propulsion Aircraft,” *Journal of Aircraft*, Vol. 56, No. 6, 2019, pp. 2172–2188.
https://doi.org/10.2514/1.C035388

[31] de Vries, R. D., Hoogreef, M. F. M., and Vos, R., “Range Equation for Hybrid-Electric Aircraft with Constant Power Split,” *Journal of Aircraft*, Vol. 57, No.

3, 2020, pp. 552–557.
https://doi.org/10.2514/1.C035734

[32] de Vries, R. D., Hoogreef, M. F. M., and Vos, R., “Aeropropulsive Efficiency Requirements for Turboelectric Transport Aircraft,” *AIAA Scitech 2020 Forum*, AIAA Paper 2020-0502, 2020.
https://doi.org/10.2514/6.2020-0502

[33] Cakin, U., Kacan, Z., Aydogan, Z., and Kuvvetli, Ipek., “Initial Sizing of Hybrid Electric VTOL Aircraft for Intercity Urban Air Mobility,” *AIAA Aviation 2020 Forum*, AIAA Paper 2020-3173, 2020.
https://doi.org/10.2514/6.2020-3173

[34] Hartmann, J., and Strack, M., Nagel, B., “Conceptual Assessment of Different Hybrid Electric Air Vehicle Options for a Commuter with 19 Passengers,” *2018 AIAA Aerospace Sciences Meeting*, AIAA Paper 2018-2025, 2018.
https://doi.org/10.2514/6.2018-2025

[35] Finger, D. F., Bil, C., and Braun, C., “Initial Sizing Methodology for Hybrid-Electric General Aviation Aircraft,” *Journal of Aircraft*, Vol. 57, No. 2, 2020, pp. 245–255.
https://doi.org/10.2514/1.C035428

[36] Finger, D. F., Braun, C., and Bil, C., “Impact of Engine Failure Constraints on the Initial Sizing of Hybrid-Electric GA Aircraft,” *AIAA Scitech 2019 Forum*, AIAA Paper 2019-1812, 2019.
https://doi.org/10.2514/6.2019-1812

[37] Finger, D. F., Goetten, F., Braun, C., and Bil, C., “Initial Sizing for a Family of Hybrid-Electric VTOL General Aviation Aircraft,” *67. Deutscher Luft- und Raumfahrtkongress DLRK2018*, DGLR, Bonn, Germany, 2018, Paper 0102.
https://doi.org/10.25967/480102

[38] McDonald, R. A., “Electric Motor Modeling for Conceptual Aircraft Design,” 51st AIAA Aerospace Sciences Meeting including the New Horizons Forum and Aerospace Exposition, AIAA Paper 2013-0941, Jan. 2013.
https://doi.org/10.2514/6.2013-941

[39] McDonald, R. A., “Electric Propulsion Modeling for Conceptual Aircraft Design,” *52nd Aerospace Sciences Meeting, AIAA SciTech Forum*, AIAA Paper 2014-0536, Jan. 2014.
https://doi.org/10.2514/6.2014-0536

[40] Sziroczak, D., Jankovics, I., Gal, I., and Rohacs, D., “Conceptual Design of Small Aircraft with Hybrid-Electric Propulsion Systems,” *Energy*, Vol. 204, No. 1, 2020, Paper 117937.
https://doi.org/10.1016/j.energy.2020.117937

[41] Lukaczyk, T. W., Wendorff, A. D., Colonno, M., Economon, T. D., Alonso, J. J., Orra, T. H., and Ilario da Silva, C., “SUAVE: An Open-Source Environment for Multi-Fidelity Conceptual Vehicle Design,” *16th AIAA/ISSMO Multidisciplinary Analysis and Optimization Conference*, AIAA Paper 2015-3087, 2015.
https://doi.org/10.2514/6.2015-3087

[42] Mills, B. T., and Datta, A., “Analysis of a Permanent Magnet Synchronous Motor Coupled to a Flexible Rotor for Electric VTOL,” *74th Annual Forum & Technology Display,* Phoenix, Arizona, USA, May 14–17, 2018.

[43] Malpica, C., and Withrow-Maser, S., “Handling Qualities Analysis of Blade Pitch and Rotor Speed Controlled eVTOL Quadrotor Concepts for Urban Air Mobility,” *VFS International Powered Lift Conference 2020,* San Jose, CA, Jan. 21–23, 2020.

[44] Lin, D., Zhou, P., and Cendes, Z. J., “In-Depth Study of the Torque Constant for Permanent-Magnet Machines,” *IEEE Transactions on Magnetics,* Vol. 45, No. 12, 2009, pp. 5383–5387.
https://doi.org/10.1109/TMAG.2009.2026043

[45] Lee, D., Jeong, S., and Yee, K., “Development of a Conceptual Design Tool for Various Compound Helicopters,” *Proceedings of the 44th European Rotorcraft Forum*, Delft, Netherlands, Sep. 18–20, 2018.

[46] Jeong, S., Lee, D., and Yee, K., “Development of Conceptual Design Method of Compound Rotorcraft using Lift Fan,” *Proceedings of the 7th Asian/Australian Rotorcraft Forum*, Jeju, Korea, Oct. 30–Nov. 1, 2018.

[47] Lee, D., Kang, S., and Yee, K., “A Comparison Study of Rotorcraft with Hybrid Electric Propulsion System,” *Proceedings of the 45th European Rotorcraft Forum*, Warsaw, Poland, Sep. 17–20, 2018.

[48] Kang, S., Lee, D., Jeong, S., and Yee, K., “Sizing Methodology and Performance Assessment of Hybrid Electric Propulsion Aircraft,” *Proceedings of the 7th Asian/Australian Rotorcraft Forum*, Jeju, Korea, Oct. 30–Nov. 1, 2018.

[49] Kang, S., Lee, D., Kim, H., Lim, D., Lee, D., Yoon, T., Hong, Y., Jeong, S., Park, O., Lee, S., and Kang, S., “Extreme Altitude Mountain Rescue Vehicle,” *Design Report*, submitted to the American Helicopter Society, 2nd Place and Best New Entry of 36th Annual AHS Student Design Competition, Jun. 2019. pp. 1–112.

[50] Lee, D., and Yee, K., “Advanced Analysis Method of Electric Propulsion System for UAM Vehicles,” *Proceedings of the 47th European Rotorcraft Forum*, Sept. 7–9, 2021, Virtual.

[51] Kim, H., Lee, D., Seo, J., Hong, Y., and Yee, K., “Design Methodology of Urban Air Mobility for Noise Mitigation at Conceptual Design Stage,” *Proceedings of the 48th European Rotorcraft Forum*, Winterthur, Switzerland, Sep. 6–8, 2022.

[52] Lee, D., Lim, D., and Yee, K., “Generic Design Methodology for Vertical Takeoff and Landing Aircraft with Hybrid-Electric Propulsion,” *Journal of Aircraft*, Vol. 59, No. 2, 2022, pp. 278–292. https://doi.org/10.2514/1.C036214

[53] Johnson, W., “NDARC – NASA Design and Analysis of Rotorcraft,” NASA TP-2015-218751, April 2015.

[54] Raymer, D. P., Aircraft Design: A Conceptual Approach, AIAA Education Series, AIAA, Reston, Virginia, 2002. https://doi.org/10.2514/4.869112

[55] Roskam, J., *Airplane Design, Part 5: Component Weight Estimation*, 5th ed., Design, Analysis and Research Corporation, Lawrence, Kansas, 2018.

[56] Schwartzberg, M. A., Smith, R. L., Means, J. L., Law, H. Y. H., and Chappell, D.P., "Single-rotor Helicopter Design and Performance Estimation Programs," Vol. 1, Methodology, SRIO Report Number 77-1, Jun. 1977.

[57] Brown, G.V., Kascak, A. F., Ebihara, B., Johnson, D., Choi, B., Siebert, M., and Buccieri, C., "NASA Glenn Research Center Program in High Power Density Motors for Aeropropulsion," NASA/TM—2005-213800, 2005.

[58] Vegh, J. M., Botero, E., Clarke, M., Trent, J., and Alonso, J., "Current Capabilities and Challenges of NDARC and SUAVE for eVTOL Aircraft Design and Analysis," *AIAA Propulsion and Energy 2019 Forum*, AIAA Paper 2019-4505, Aug. 2019.
https://doi.org/10.2514/6.2019-4505

[59] Nita, M., and Scholz, D., "Estimating the Oswald Factor from Basic Geometrical Parameters," *Proceedings of the German Aerospace Congress*, Berlin, Germany, Sep. 10–12, 2012.

[60] Vu, N. A., Lee, Y. J., Lee, J. W., Kim, S., and Chung, I. J., "Configuration Design and Optimisation Study of a Compound Gyroplane," *Aircraft Engineering and Aerospace Technology*, Vol. 83, 2011, pp. 420–428. https://doi.org/10.1108/00022661111173298

[61] Alvarez, E. J., and Ning, A., "Modeling Multirotor Aerodynamic Interactions Through the Vortex Particle Method," *AIAA Aviation 2019 Forum*, AIAA Paper 2019-2827, 2019.
https://doi.org/10.2514/6.2019-2827

[62] Leishman, J. G., *Principles of Helicopter Aerodynamics*, 2nd ed., Cambridge University Press, New York, 2006, pp. 115–170.

[63] Pereira, J., "Hover and Wind-tunnel Testing of Shrouded Rotors for Improved Micro Air Vehicle Design," Ph.D. Dissertation, University of Maryland, College Park, Maryland, 2008.

[64] Du, Z., and Selig, M., "A 3-D Stall-Delay Model for Horizontal Axis Wind Turbine Performance Prediction," *1998 ASME Wind Energy Symposium*, AIAA Paper 1998-21, 1998.
https://doi.org/10.2514/6.1998-21

[65] Lee, H., Prasad, R., and Choi, S., "Aerodynamic Analysis for Conceptual Design of a Lift-Fan type Aircraft," *34th AIAA Applied Aerodynamics Conference*, AIAA Paper 2016-3408, 2016. https://doi.org/10.2514/6.2016-3408

[66] Patterson, M. D., "Conceptual Design of High-Lift Propeller Systems for Small Electric Aircraft," Ph.D. Dissertation, Georgia Institute of Technology, Atlanta, Georgia, 2016.

[67] Goodno, B. J., and Gere, J. M., *Mechanics of Materials*, 8th ed., Cengage Learning, Pacific Grove, 2013, pp. 372–463.

[68] Schwartzberg, M. A., Smith, R. L., Means, J. L., Law, H. Y. H., and Chappell, D.P., "Single-rotor Helicopter Design and Performance Estimation Programs," Vol. 1, Methodology, SRIO Report Number 77-1, Jun. 1977.

[69] Sliwinski, J., Gardi, A., Marino, M., and Sabatini, R., "Hybrid-Electric Propulsion Integration in Unmanned Aircraft," *Energy*, Vol. 140, Dec. 2017, pp. 1407–1416. https://doi.org/10.1016/j.energy.2017.05.183

[70] Lents, C., "Aircraft Electrified Propulsion Systems and Component Design: Prime Movers and Propulsors," *AIAA Propulsion and Energy 2019 Forum*, Indianapolis, USA, Aug. 19–22, 2019.

[71] Afonso, F., Ferreira, A., Ribeiro, I., Lau, F., and Suleman, A., "On the Design of Environmentally Sustainable Aircraft for Urban Air Mobility," *Transportation Research Part D: Transport and Environment*, Vol. 91, 2021, p. 102688. https://doi.org/10.1016/j.trd.2020.102688

[72] Straton, R. W., Wong, H. M. and Hileman, J. I., "Life Cycle Greenhouse Gas Emissions from Alternative Jet Fuels," PARTNER Project 28 Report, Version 1.2, June 2010.

[73] Farassat, F., and Brentner, K., "The Acoustic Analogy and the Prediction of the Noise of Rotating Blades," *Theoretical and Computational Fluid Dynamics*, Vol. 10, 1997, pp. 155-170. https://doi.org/10.1007/s001620050056

[74] Brentner, K. S., and Jones, H. E., “Noise Prediction for Maneuvering Rotorcraft,” *6th AIAA/CEAS Aeroacoustics Conference*, AIAA Paper 2000-2031, 2000.

[75] Yang, T., Brentner, K., and Walsh, G., “A Dual Compact Model for Rotor Thickness Noise Prediction”, *Journal of the American Helicopter Society*, Vol. 63, No. 2, 2018, pp. 12-23. https://doi.org/10.4050/JAHS.63.022007

[76] Brentner, K., and Farassat, F., “Modeling Aerodynamically Generated Sound of Helicopter Rotors, ” *Progress in Aerospace Science*, Vol. 39, No. 2–3, 2003, pp. 83-120. https://doi.org/10.1016/S0376-0421(02)00068-4

[77] Grunditz, E. A., and Thiringer, T., “Performance Analysis of Current BEVs Based on a Comprehensive Review of Specifications,” *IEEE Transactions on Transportation Electrification*, Vol. 2, No. 3, 2016, pp. 270–289. https://doi.org/10.1109/TTE.2016.2571783

[78] Grunditz, E. A, and Thiringer, T., “Electric Vehicle IGBT Power Module Sizing and Drive Cycle Energy Efficiency for Various Switching Frequencies-Based on a Scalable Module Model,” *Proceedings of 2018 20th European Conference on Power Electronics and Applications*, Riga, Latvia, Sept. 17–20, 2018.

[79] Grunditz, E. A, and Thiringer, T., “Acceleration, Drive Cycle Efficiency, and Cost Tradeoffs for Scaled Electric Vehicle Drive System,” *IEEE Transactions on Industry Applications*, Vol. 56, No. 3, 2020, pp. 3020–3033. https://doi.org/10.1109/TIA.2020.2976861

[80] Liu Q., “Analysis, Design, and Control of Permanent Magnet Synchronous Motors for Wide-Speed Operation,” Ph.D. Dissertation, National University of Singapore, 2005.

[81] Hoang, K. D., Wang, J., Cyriacks, M., Melkonyan, A., and Kriegel, K., “Feed-Forward Torque Control of Interior Permanent Magnet Brushless AC Drive for Traction Applications,” *Proceedings of 2013 International Electric*

Machines & Drives Conference, Chicago, USA, May 12–15, 2013. https://doi.org/10.1109/iemdc.2013.6556247

[82] Goss, J., Mellor, P. H., Wrobel, R., Staton, D. A., and Popescu, M., “The Design of AC Permanent Magnet Motors for Electric Vehicles: A Computationally Efficient Model of the Operational Envelope,” *Proceedings of 6th IET International Conference on Power Electronics*, Machines and Drives, Bristol, England, March 27–29, 2012. https://doi.org/10.1049/cp.2012.0251

[83] Ding, X., Guo, H., Xiong, R., Chen, F., Zhang, D., and Gerada, C., “A New Strategy of Efficiency Enhancement for Traction Systems in Electric Vehicles,” *Applied Energy*, Vol. 205, 2017, pp. 880–891. https://doi.org/10.1016/j.apenergy.2017.08.051

[84] Mestha L. K, Evans P. D., “Analysis of On-State Losses in PWM Inverters. Electric Power Applications,” *Electric Power Applications*, Vol. 136, No. 4, 1989, pp. 189–195.

[85] Garcia, R. C., and Pinto, J. O., “A New Simplified SVPWM Algorithm Based on Modified Carrier Signal,” *Sba: Controle & Automação Sociedade Brasileira de Automatica*, Vol. 22, No. 5, 2011, pp. 545–557. https://doi.org/10.1590/s0103-17592011000500009

[86] Linden. D., and Reddy, T. B., *Handbook of Batteries*, 3rd ed., McGraw-Hill, New York, 2011, pp. 36–72.

[87] German, B. J., “Introduction to Batteries and Cell Discharge Modeling for Electric Aircraft Design,” *Short Course: Design of Electric and Hybrid-Electric Aircraft at 2018 AIAA Aviation Conference*, Atlanta, Georgia, June 23–24, 2018.

[88] Bell Helicopters, “Advancement of Proprotor Technology. Task 2 - Wind-Tunnel Test Results,” NASA CR 114363, 1971.

[89] Koning, W. J. F., Acree, C. W., and Rajagopalan, G., “Using RotCFD to Predict Isolated XV-15 Rotor Performance,” *2016 AHS Technical Meeting on Aeromechanics Design for Vertical Lift*, San Francisco, USA, Jan. 20–22, 2016.

[90] Helf, S., et al, "Full-Scale Hover Test of a 25-Foot Tilt Rotor", BHT Report 300-099-010, NASA CR 114626, May 1973.

[91] Armata J. M, Besrest, B., Pauly R., “PSIM/MATLAB Cosimulation for Electrical Architectures Global Models,” AES 2005.

[92] Jansen, R., Bowman, C., and Jankovsky, A., “Sizing Power Components of an Electrically Driven Tail Cone Thruster and a Range Extender,” *16th AIAA Aviation Technology, Integration, and Operations Conference*, AIAA Paper 2016-3766, 2016.
https://doi.org/10.2514/6.2016-3766

[93] Regas, B. I., “Analysis of Different Powertrain Configurations for a Formula Style Electric Racecar,” M.S. Dissertation, Universitat Politècnica de Catalunya, 2019.

[94] Freeman, J., Osterkamp, P., Green,M.W., Gibson, A.R., and Schiltgen,B. T., “Challenges and Opportunities for Electric Aircraft Thermal Management,” *Aircraft Engineering and Aerospace Technology*, Vol. 86, No. 6, 2014, pp. 519–524.
https://doi.org/10.1108/AEAT-04-2014-0042

[95] Falck, R. D., Chin, J., Schnulo, S. L., Burt, J. M., and Gray, J. S., “Trajectory Optimization of Electric Aircraft Subject to Subsystem Thermal Constraints,” *18th AIAA/ISSMO Multidisciplinary Analysis and Optimization Conference*, AIAA Paper 2017-4002, 2017. https://doi.org/10.2514/6.2017-4002

[96] Trawick, D., Perullo, C., Armstrong, M., Snyder, D., Tai, J. C., and Mavris, D. N., “Development and Application of GT-HEAT for the Electrically Variable Engine Design,” *55th AIAA Aerospace Sciences Meeting*, AIAA Paper 2017-1922, 2017.
https://doi.org/10.2514/6.2017-1922.

[97] Lents, C., Hardin, L., Rheaume, J., and Kohlman, L., “Parallel Hybrid Gas-Electric Geared Turbofan Engine Conceptual Design and Benefits Analysis,” *52nd AIAA/SAE/ASEE Joint Propulsion Conference*, AIAA Paper 2016-4610, 2016.
https://doi.org/10.2514/6.2016-4610

[98] Brelje, B. “Multidisciplinary Design Optimization of Electric Aircraft Considering Systems Modeling and Packaging,” Ph.D. Dissertation, University of Michigan, Ann Arbor, MI, 2021.

[99] Datta A. “PEM Fuel Cell Model for Conceptual Design of Hydrogen eVTOL Aircraft, NASA CR 20210000284, 2021.

[100] Ng W, Datta A, “An Examination of Hydrogen Fuel Cells and Lithium-ion Batteries for Electric Vertical Take-off and Landing Aircraft,” *Proceedings of the 44th European Rotorcraft Forum*, Delft, Netherlands, Sep. 18–20, 2018.

[101] Park, J., Lee, D., and Yee, K., "Development of Fuel Cell/Battery Hybrid System Sizing Methodology for eVTOL Aircraft," *AIAA AVIATION 2022 Forum*, AIAA Paper 2022-3514, 2022.

[102] Park, J., Lee, D., Lim, D., and Yee, K., “A Refined Sizing Method of Fuel Cell-battery Hybrid System for eVTOL Aircraft,” *Applied Energy*, Vol. 328, 2022, p. 120160.
https://doi.org/10.1016/j.apenergy.2022.120160

[103] Bacchini, A., and Cestino, E., “Electric VTOL Configurations Comparison,” *Aerospace*, Vol. 6, No. 3, 2016, pp. 26
https://doi.org/10.3390/aerospace6030026

[104] Kang, Y., “Smart UAV Conceptual Design Report,” SUDC-DRB1-04-002-R0, 2005.

Appendix A.

Regression Models for Motors and Inverters

The regression models for the motor parameters were developed using datasheet information from EMRAX[xx], which manufactures axial-flux PMSMs with high specific power for aviation propulsion. These motors are classified into three types (high, medium, and low) according to the operating voltage, and the maximum voltage is limited to $V_{\mathrm{DC,max}} = 800\ \mathrm{V}$ because most controllers with a high performance-to-price ratio have a voltage limit of 800 V. The regression models for the inverter parameters were constructed using datasheet information for dual inverters from Infineon with I_{cn} ratings from 50 to 1800 A and a V_{ces} of 1200 V[xxi]. If designers wish to use datasheet information from other companies, they may create new regression models in the same manner.

[xx]Data available online at https://www.emrax.com [retrieved 29 September 2022].

[xxi]Data available online at https://www.infineon.com [retrieved 29 September 2022].

Table A-1 Regression models for motor and inverter parameters

Device	Parameter	Estimation formula	
Motor	Maximum mechanical rotational speed $\omega_{\text{mech,max}}$ [RPM]	$f_1 = 64462\tau_{\text{cr,mot}}^{-0.547}$	(High)
		$f_1 = 28003\tau_{\text{cr,mot}}^{-0.353}$	(Medium)
		$f_1 = 15530\tau_{\text{cr,mot}}^{-0.22}$	(Low)
	Maximum DC link voltage $V_{\text{DC,max}}$ [V]	$f_2 = 232.4\ln\tau_{\text{cr,mot}} - 465.7$	(High)
		$f_2 = 225.8\ln\tau_{\text{cr,mot}} - 600.5$	(Medium)
		$f_2 = 0.698\tau_{\text{cr,mot}} + 720.0$	(Low)
	Continuous rated current I_{cr} [ARMS]	$f_3 = 70.0\ln\tau_{\text{cr,mot}} + 112.5$	(High)
		$f_3 = 26.8\ln\tau_{\text{cr,mot}} + 40.99$	(Medium)
		$f_3 = 0.089\tau_{\text{cr,mot}} + 98.3$	(Low)
	d-Axis inductance L_d [μH]	$f_4 = 0.708\tau_{\text{cr,mot}} + 75.48$	(High)
		$f_4 = 0.306\tau_{\text{cr,mot}} + 31.96$	(Medium)
		$f_4 = 0.041\tau_{\text{cr,mot}} + 4.39$	(Low)
	q-Axis inductance L_q [μH]	$f_5 = 0.771\tau_{\text{cr,mot}} + 77.7$	(High)
		$f_5 = 0.333\tau_{\text{cr,mot}} + 33.5$	(Medium)
		$f_5 = 0.045\tau_{\text{cr,mot}} + 4.51$	(Low)
	Magnetic flux λ_0 [Wb]	$f_6 = 4\text{e-}05\tau_{\text{cr,mot}} + 0.013$	(High)
		$f_6 = 2\text{e-}05\tau_{\text{cr,mot}} + 0.009$	(Medium)
		$f_6 = 8\text{e-}05\tau_{\text{cr,mot}} + 0.003$	(Low)
	Resistance R [mΩ]	$f_7 = 8.29\ln\tau_{\text{cr,mot}} - 22.4$	(High)
		$f_7 = 3.54\ln\tau_{\text{cr,mot}} - 9.59$	(Medium)
		$f_7 = 0.008\tau_{\text{cr,mot}} + 0.189$	(Low)

	No-load power $P_{\text{no-load}}$ [kW]	$g = 2.5\text{e-}9 \times P_{\text{cr,mot}}^{1.224} \times \omega_{\text{mech}}^{1.816}$	-
Inverter	IGBT turn-on energy loss E_{on} [mJ]	$h_1 = 6\text{e-}6 I_{\text{cn}}^2 + 0.1 I_{\text{cn}}$ $h_1 = -2\text{e-}6 I_{\text{cn}}^2 + 0.077 I_{\text{cn}}$	(125 °C) (25 °C)
	IGBT turn-off energy loss E_{off} [mJ]	$h_2 = 2\text{e-}5 I_{\text{cn}}^2 + 0.112 I_{\text{cn}}$ $h_2 = 2\text{e-}5 I_{\text{cn}}^2 + 0.085 I_{\text{cn}}$	(125 °C) (25 °C)
	Diode reverse recovery energy E_{rec} [mJ]	$h_3 = 4\text{e-}6 I_{\text{cn}}^2 + 0.076 I_{\text{cn}}$ $h_3 = 6\text{e-}6 I_{\text{cn}}^2 + 0.036 I_{\text{cn}}$	(125 °C) (25 °C)
	IGBT threshold voltage V_{ce0} [V]	$h_4 = 1.007$ $h_4 = 1.105$	(125 °C) (25 °C)
	Diode threshold voltage V_{F0} [V]	$h_5 = 0.841$ $h_5 = 0.971$	(125 °C) (25 °C)
	IGBT on-state slope resistance R_{ce} [mΩ]	$h_6 = 1484.4 I_{\text{cn}}^{-1.05}$ $h_6 = 1012.6 I_{\text{cn}}^{-1.05}$	(125 °C) (25 °C)
	Diode on-state slope resistance R_{F} [mΩ]	$h_7 = 554.9 I_{\text{cn}}^{-0.965}$ $h_7 = 383.2 I_{\text{cn}}^{-0.931}$	(125 °C) (25 °C)

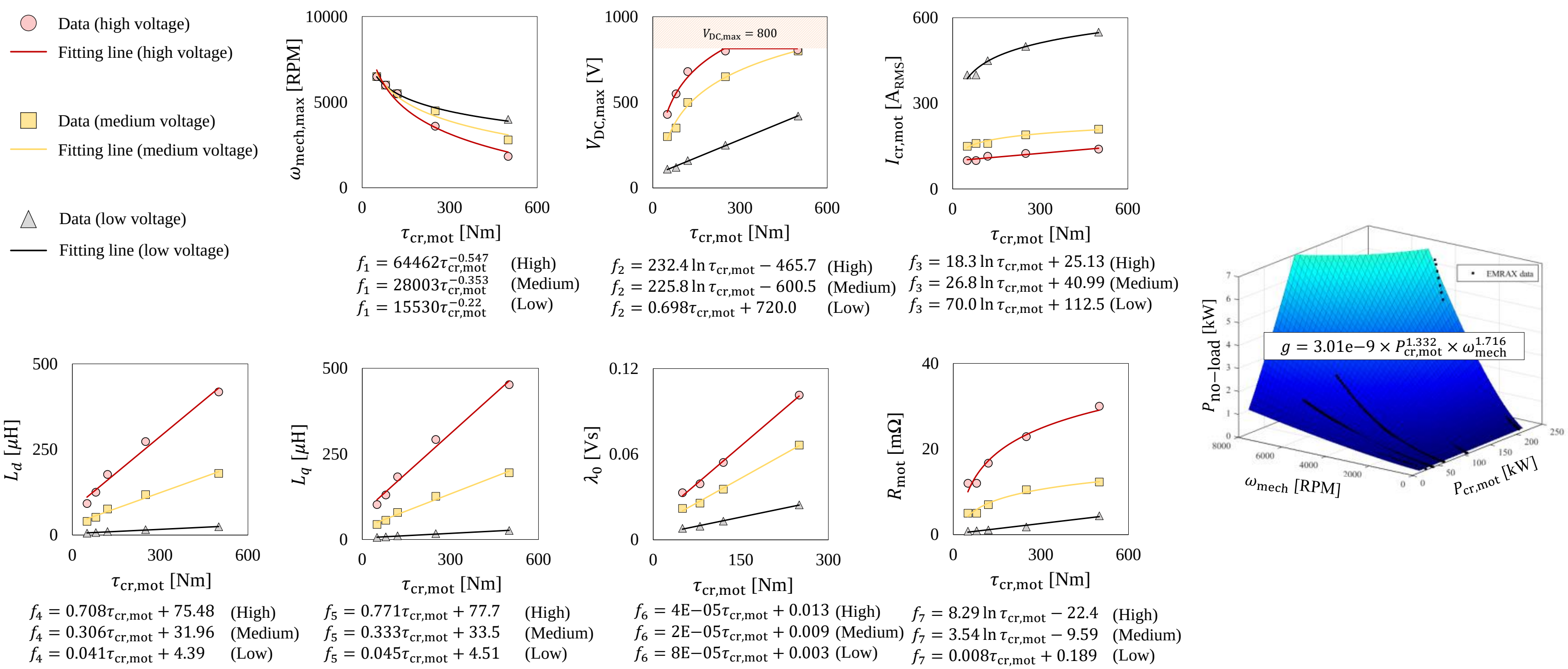

Fig. A-1 Regression models based on datasheet information for EMRAX motors.

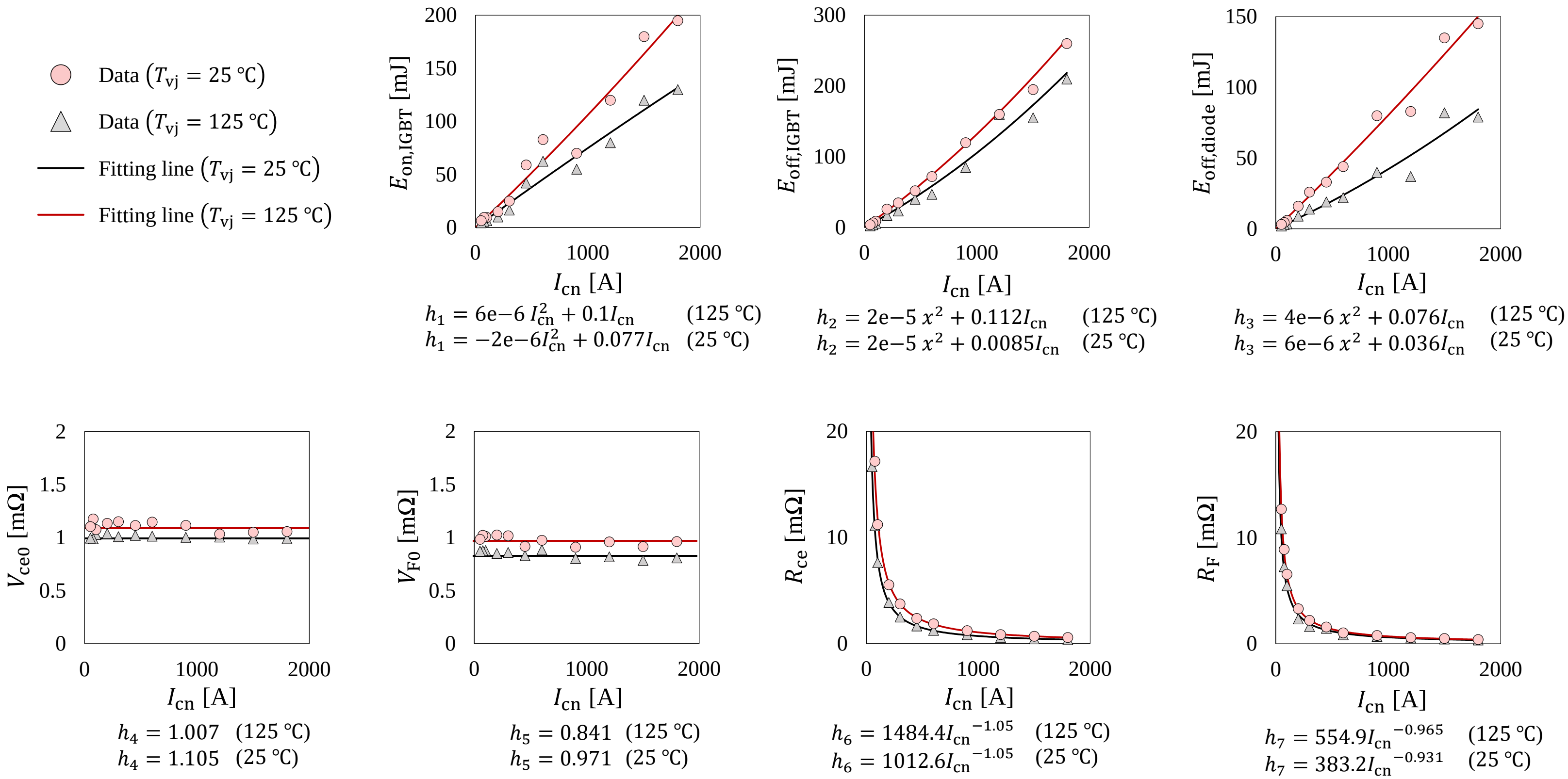

Fig. A-2 Regression models based on datasheet information for Infineon inverters.

Appendix B.

Geometric data and Parameters for Lift+cruise Aircraft

Table B-1 Geometric data and design parameters for verification of results.

Geometry data	
Lift DP [58]	Radius: 0.61 m Solidity: 0.2 Taper: 0.75 Collective pitch: 0.236 rad
Wing [58, 103]	Area: 10.59 m^2 Aspect ratio: 11.4 Taper: 1.0 Incidence angle: 0.216 rad
Thruster for cruise [58]	Radius: 1.07 m Solidity: 0.1
Horizontal stabilizer [58]	Area: 1.77 m^2 Aspect ratio: 4.78 Taper: 1.0
Vertical stabilizer [58]	Area: 1.18 m^2 Aspect ratio: 1.41

Design parameters	
Lift-DP [58]	Airfoil: NACA0012 Material: aluminum 6061-T6 Parasitic drag (D/q): 0.11 m2 Technical factor: 0.65
Wing [58]	Airfoil: NACA0018 Material: aluminum 6061-T6 Technical factor: 0.65
Thruster for cruise [58]	Airfoil: NACA0012 Material: aluminum 6061-T6 Technical factor: 0.65
Supporting rod [58]	Material: aluminum 2024 Parasitic drag (D/q): 0.091 m2
Fuselage [58]	Material: Composite Parasitic drag (D/q): 0.058 m2 Technical factor: 0.76
Vertical stabilizer [58]	Airfoil: NACA0012 Parasitic drag (D/q): 0.019 m2

Taper: 0.5

	Technical factor: 0.76
Horizontal stabilizer [58]	Airfoil: NACA0012 Technical factor: 0.76
Landing gear [58]	Parasitic drag (D/q): 0.035 m2
Motor [58, 92]	SP: 6.0 kW/kg Efficiency: 95% (cruise), 88% (hover)
Inverter [92]	SP: 12 kW/kg Efficiency: 98%
TMS [92]	SP: 0.68 kW/kg
Battery [58, 92]	SE: 300 W·h/kg Efficiency: 0.93 Maximum DOD: 0.8 Maximum C-rate: 10 (discharge), 5 (charge)

Appendix C.

Urban Air Mobility eVTOL Aircraft Design Results

The FEPS-powered VTOL aircraft design for urban air mobility (UAM) service was conducted using the proposed generic system design methodology. For UAM service, two types of eVTOL aircraft have been selected, and the characteristics of each are summarized below:

Vectored-thrust concept
(selected model: Joby – S4)

- 6 tilting rotors with 5 blades
- Tilting rotors provide both lift and thrust
- Collective pitch control with rotational speed schedule
- Retractable wheeled-type landing gear

Wingless concept
(selected model: Volocopter – 2X)

- 18 rotors with 2 blades
- Multiple rotors provide both lift and thrust
- Rotational speed control
- Skid-type landing gear

As mentioned in Table 1-1, there is a preferred use case for each UAM eVTOL aircraft concept. Therefore, the mission profiles of the vectored-thrust concept and the wingless concept are configured differently for long- and short-distance, as shown in Fig. C-1 and Table C-1.

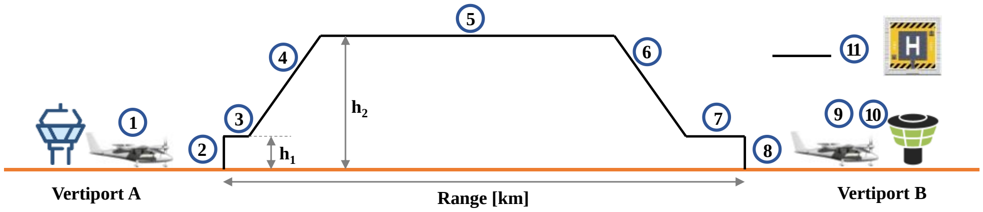

Fig. C-1 Mission profile for the UAM service.

In this study, the characteristic values of the EPS have been determined at the current technological level to derive realistic design results. First, the battery's specific energy was assumed to be 200 Wh/kg, and the maximum C-rate was 10C (discharge) and 3C (charge), according to the EPiC series specifications. The specific power value was set for the electric motor at 4.1 kW/kg based on Magni250 and Magni500 motors from MagniX. By referring to NASA's research paper [92], the specific power of the inverter was assumed to be 13 kW/kg.

In addition, EPS modeling of Approach 1 was used; $\eta_{\mathrm{mot}} = 0.9548$, $\eta_{\mathrm{inv}} = 0.98$, and $\eta_{\mathrm{bat}} = 0.97$.

Table C-1 Mission profile for the UAM service.

	Mission Segment	Vectored-thrust concept (payload: 440 kg)				Wingless concept (payload: 200 kg)			
		Vertical speed [km/h]	Cruise speed [km/h]	Altitude [m]	Time [min]	Vertical speed [km/h]	Cruise speed [km/h]	Altitude [m]	Time [min]
1	Taxiing	0	10	0	0.3	0	10	0	0.3
2	Takeoff	9	0	30	0.2	9	0	30	0.2
3	Transition		$0 \rightarrow 1.2V_{\text{stall}}$	-	1		$0.3V_{\text{cruise}}$	-	1
4	Cruise-climb	18	$\text{Avg}(V_{\text{stall}}, V_{\text{cruise}})$	610	1.3	9	$0.8V_{\text{cruise}}$	610	5.15
5	Cruise	0	$V_{\text{cruise}} = 250$	610	21.03	0	$V_{\text{cruise}} = 100$	610	15
6	Cruise-descent	-18	$\text{Avg}(V_{\text{stall}}, V_{\text{cruise}})$	30	1.3	-9	$0.8V_{\text{cruise}}$	30	5.15
7	Transition		$1.2V_{\text{stall}} \rightarrow 0$	-	1		$0.3V_{\text{Cruise}}$	-	1
8	Landing	-7.4	0	0	0.24	-7.4	0	0	0.24
9	Taxiing	0	10	0	0.3	0	10	0	0.3

The design optimization problem for UAM eVTOL aircraft is defined as follows:

Objective (1):

Minimize Maximum takeoff weight (kg), MTOW

Constraints (2):

$Cr_{\mathrm{max}} \leq Cr_{\mathrm{CSTR}}$ for the battery life

$R \leq R_{\mathrm{limit}},\ b_{\mathrm{w}} \leq b_{\mathrm{w,limit}}$ for the design feasibility

Design variables:

Composition	Vectored-thrust (9)	Wingless (4)
Rotor	$R,\ c,\ \theta_{\mathrm{tw}},\ V_{\mathrm{tip}}$	$R,\ c,\ \theta_{\mathrm{tw}}, \theta_{\mathrm{i}}$
Main wing	$b, \theta_{\mathrm{i}},\ AR$	-
Tail wing	b, AR	-

As can be seen in the design optimization results (Fig. C-2), the vectored-thrust concept's payload to total weight ratio of about 20%, the optimization result was suitable for the design requirements. When performing a transitional flight, the vectored-thrust concept requires as much power as a VTOL flight. The reason is that additional drag is generated in the rotor and nacelle having a specific tilt angle. In addition, the vectored-thrust concept has wings, with flight efficiency in descending missions far superior to the wingless concept. Lastly, the maximum discharge C-rate of the vectored-thrust concept during flight is approximately 4.3C in a vertical takeoff mission, which is a level that can be handled sufficiently by current battery technology.

In the case of the wingless concept, the payload to total weight ratio was also about 20%, resulting in a suitable design outcome. Based on the results of the mission analysis, the wingless concept appeared to have flight characteristics similar to that of a conventional helicopter. The wingless concept required the most power for a vertical takeoff mission. When the wingless concept began to fly forward, the rotor inflow reduced the induced power of the rotor, resulting in a decrease in the overall required rotor power. Finally, the maximum discharge C-rate of the wingless concept while performing the mission was 3.3C, which is a level that is currently feasible with current battery technology.

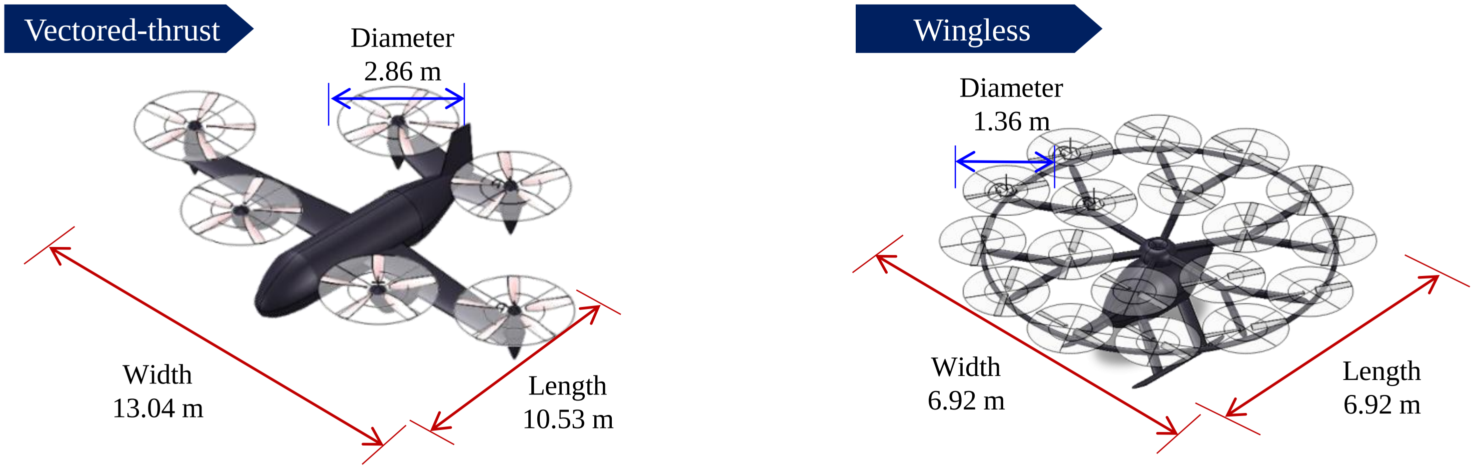

(a) 3D modeling of UAM eVTOL aircraft

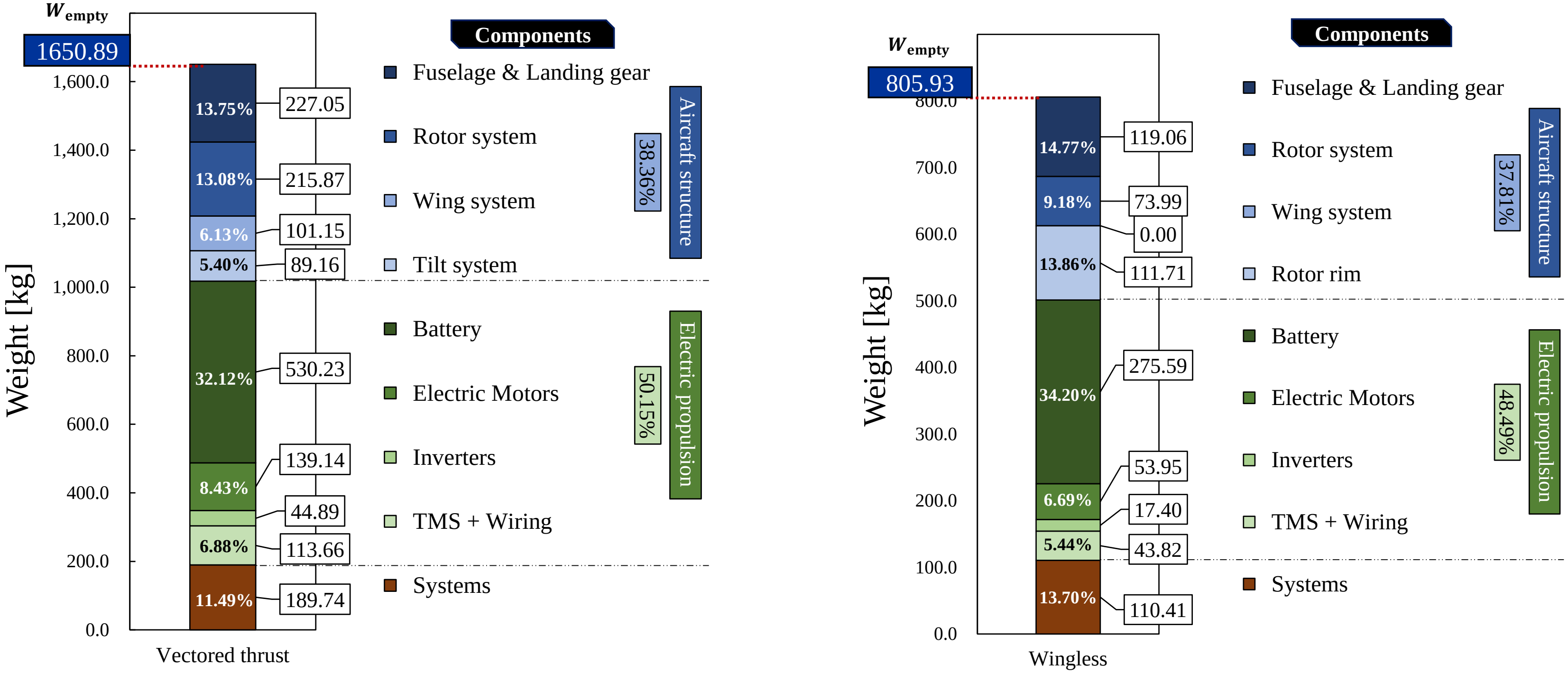

(b) Weight breakdown of UAM eVTOL aircraft

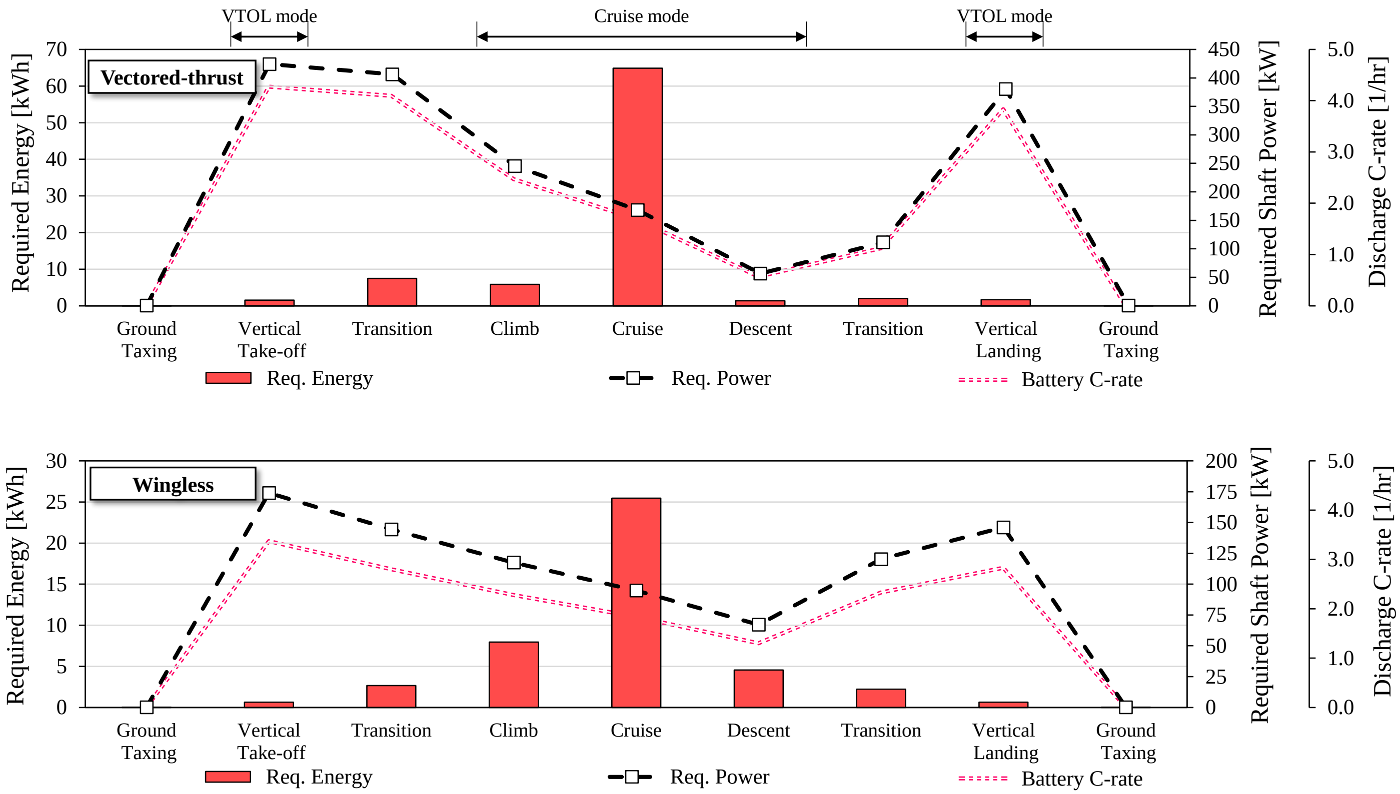

(c) Mission analysis results of UAM eVTOL aircraft

Fig. C-2 Summary of UAM eVTOL aircraft design results.

Appendix D.

Delivery eVTOL Aircraft Design Results

The eVTOL aircraft design for the delivery service was performed using the proposed generic system design methodology. Here, four types of FEPS-powered VTOL aircraft were selected for the delivery service. Following is a summary of the characteristics of each eVTOL aircraft concept.

Single rotor concept
- Nominal rotor rpm is fixed
- Swashplate is used for the pitch control
- Tail rotor offsets the anti-torque with the rotor

Multi-rotor with long body concept
- Nominal rotor rpm is fixed
- Variable collective pitch system is used
- Each rotor offsets the anti-torque of each other

Tilt-rotor concept
- Rotor slows down when converting from hovering to cruising
- Tilting rotors provide both lift and thrust
- Variable collective pitch system is used

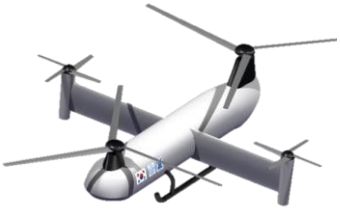

Compound concept
(Tandem rotor combined with tilt-wing)
- Nominal rotor rpm is fixed
- Rotors and propellers generate lift in hover
- Only propellers generate thrust in forward flight
- Swashplate is used for the pitch control

The mission profile used for the delivery eVTOL aircraft design is shown in Fig. D-1, in which the total endurance is 65 min, and the range is 50 km.

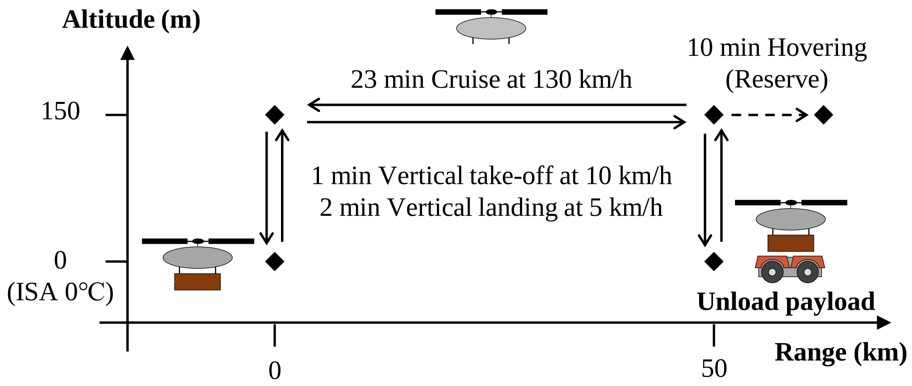

Fig. D-1 Mission profile for the delivery service.

The components of each eVTOL aircraft are listed in Table D-1. In this design case, the battery's specific energy was set at 522 Wh/kg [11], and the specific power of the motor and inverter were set at 5.4 kW/kg and 13 kW/kg [92], respectively. The wiring, communication, and electric sensors were set to account for 7.8%, 3.32%, and 4.81% of the gross weight [104], respectively. The payload system was assumed at 14% of the payload weight.[xxii] In addition, EPS modeling of Approach 1 was used; $\eta_{\mathrm{mot}} = 0.96$, $\eta_{\mathrm{inv}} = 0.98$, and $\eta_{\mathrm{bat}} = 0.94$.

[xxii]Data available online at https://www.jenoptik.com/ [retrieved 13 October 2022].

Table D-1 UAV component breakdown

Composition		Single rotor	Multi-rotor	Tilt-rotor	Compound
Electric Propulsion	Motor Battery Inverter Wiring	Common equipment			
Structure	Rotor	O	-	O	O
	Tail rotor	O	-	-	-
	Propeller	-	O	-	O
	Fuselage	O	O	O	O
	Wing	-	-	O	O
	Tail Wing	O	-	O	-
	Tilt system	-	-	O	O
	Landing gear	Skid type			
	Payload system	O	O	O	O
	Tail wing	O	-	O	-
Communication	RF LTE D2D	Common equipment			
Electric sensor	EO/IR Camera LiDAR GPS Acceleration	Common equipment			
Payload		30 kg			

The design optimization problem for delivery eVTOL aircraft is defined as follows:

Objective (1):

Minimize Maximum takeoff weight (kg), MTOW

Constraints (2):

$\sigma_{\mathrm{max}} \leq \sigma_{\mathrm{allow}}$ for the structural safety of supporting rods

$R \leq R_{\mathrm{limit}}$, $b_{\mathrm{w}} \leq b_{\mathrm{w,limit}}$ for the design feasibility

Design variables:

Composition	Single rotor (7)	Multirotor (6)	Tiltrotor (9)	Compound (10)
Rotor	$R,\ c,\ \theta_{\mathrm{tw}},\ V_{\mathrm{tip}}$	$R,\ c,\ \theta_{\mathrm{tw}}, V_{\mathrm{tip}}$	$R,\ c,\ \theta_{\mathrm{tw}}, V_{\mathrm{tip}}$	$R,\ c,\ \theta_{\mathrm{tw}}, V_{\mathrm{tip}}$
Tail Rotor	$R,\ c, V_{\mathrm{tip}}$	-	-	-
Main Wing	-	-	$b, \theta_{\mathrm{i}},\ AR$	$b,\ AR$
Propeller	-	-	-	$R,\ c, V_{\mathrm{tip}}$
Etc.	-	$D_{\mathrm{rod}},\ L_{\mathrm{rod}}$	$b_{\mathrm{ht}},\ AR_{\mathrm{ht}}$	*$\mathrm{LS}_{\mathrm{rotor-prop}}$

*$\mathrm{LS}_{\mathrm{rotor-prop}}$: Lift sharing ratio between rotor and propeller at hovering

As can be seen in the design results (Fig. D-2), in contrast to other concepts, the single rotor concept did not consider additional components such as supporting rods, main wings, and auxiliary propellers, making it the lightest empty weight and having the lowest power requirements of the four concepts (takeoff 13 kW, forward flight 9 kW).

In the multi-rotor concept, there was an additional drag generated by the four supporting rods, which accounts for 32% of the total drag. Also, the multi-rotor concept had a limitation in rotor radius due to the geometric constraint imposed by the support rods. Therefore, this concept did not perform as efficiently as the single-rotor counterpart.

The tilt-rotor concept was designed with large wings to obtain the majority of lift from the wings, resulting in rotor-wing interference in hovering flight. This interference effect accounts for about 5% of the total power required; the tiltrotor concept, therefore, performed less efficiently than a single-rotor concept.

The compound concept has additional drag due to the tandem hubs and wings and requires a large fuselage for tandem rotors. In this regard, the compound concept was found to have the heaviest empty weight and the lowest flight efficiency of the four concepts studied.

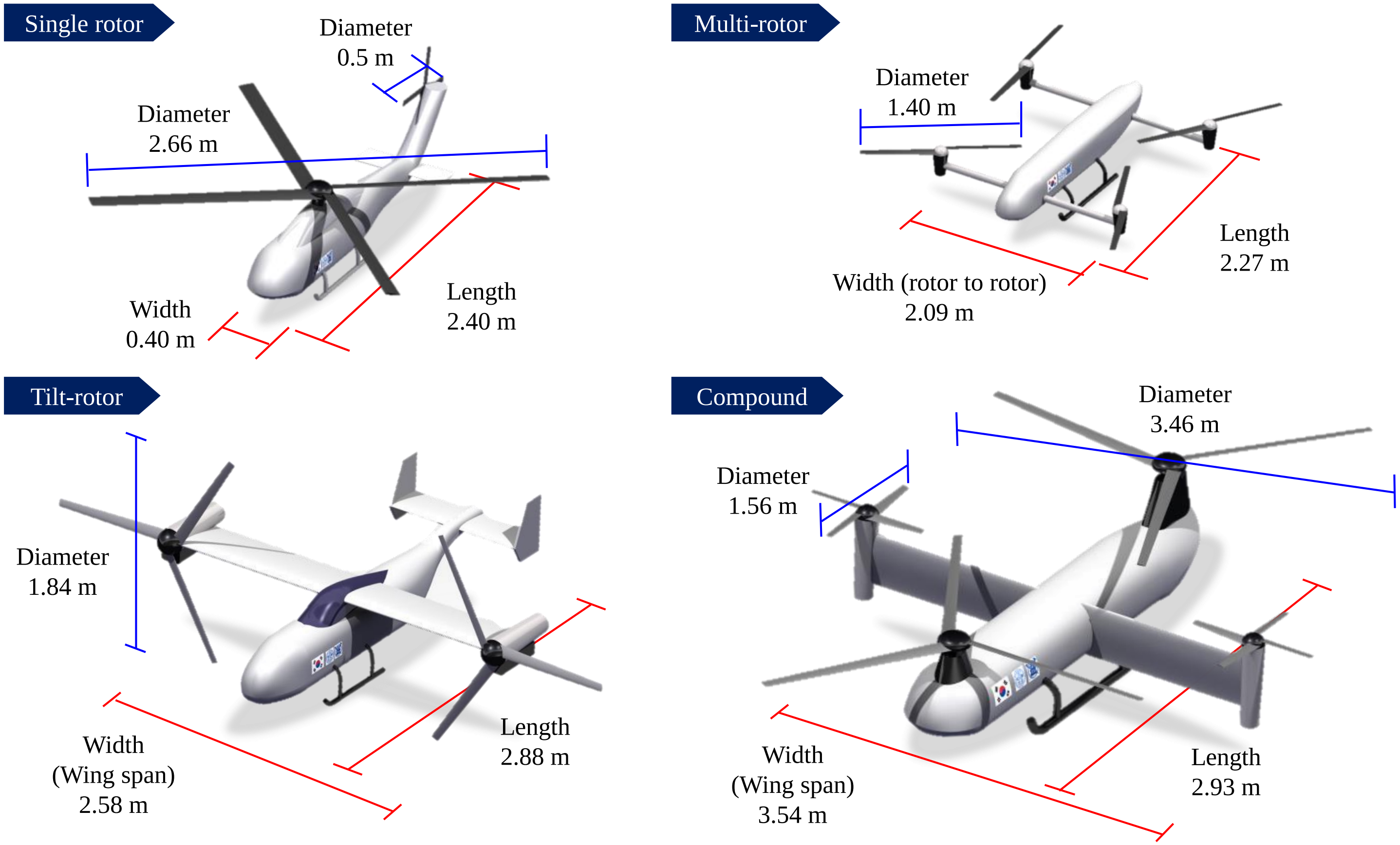

(a) 3D modeling of delivery eVTOL aircraft

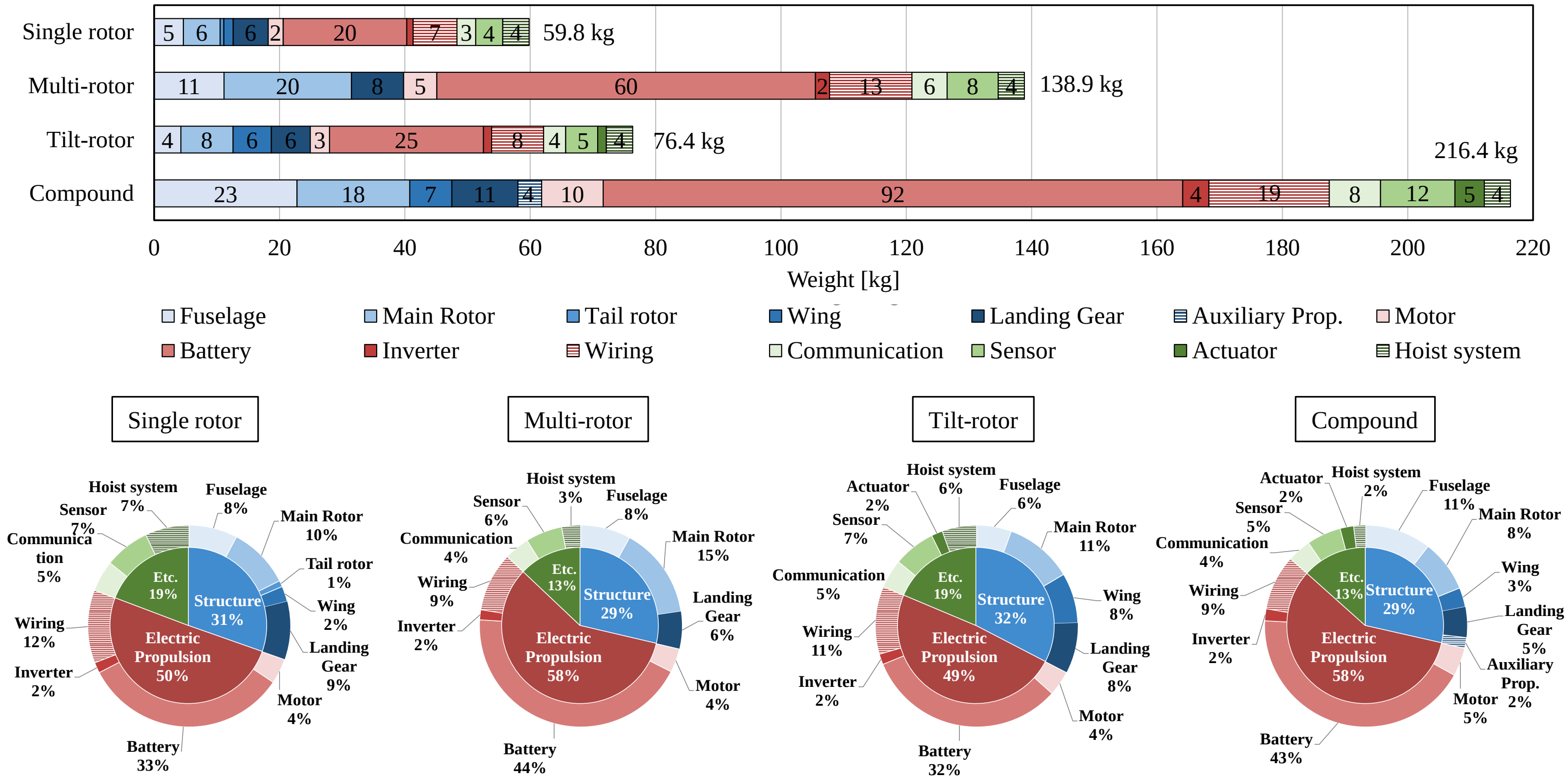

(b) Weight breakdown of delivery eVTOL aircraft

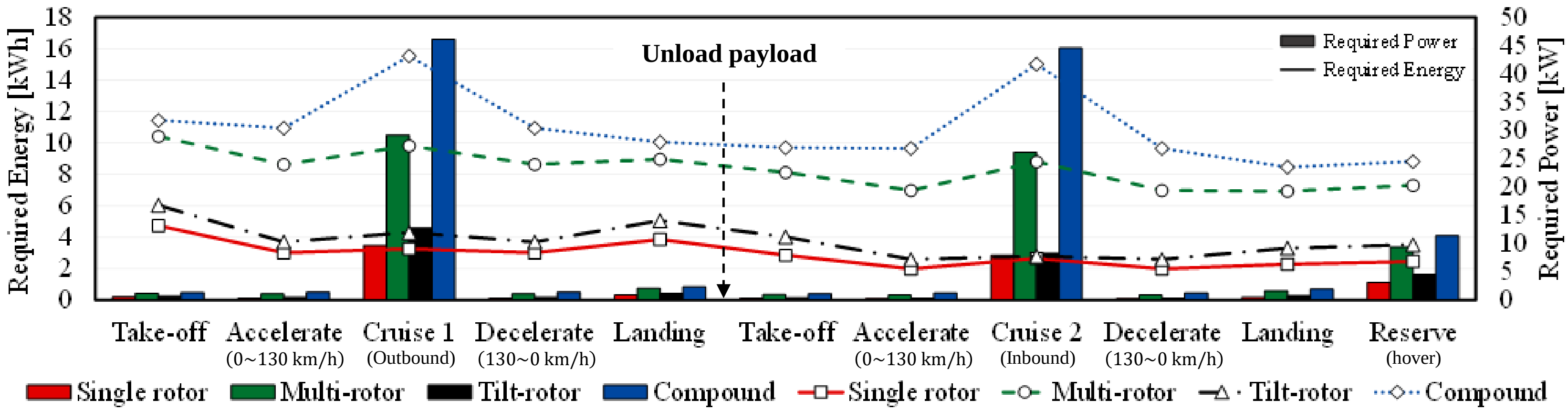

(c) Mission analysis results of delivery eVTOL aircraft

Fig. D-2 Summary of the delivery eVTOL aircraft design results.

국문 초록

항공기 전동화와 더불어, 항법 시스템 및 수직이착륙 기술의 발전은 새로운 항공 운송시스템인 차세대 항공교통(Advanced Air Mobility)이라고 하는 항공 운송 시스템의 혁신을 가능케 하였다. 현재 700 여종 이상의 차세대 항공교통용 전기동력 수직이착륙 항공기가 개발 중인 것으로 알려지고 있으며, 이들은 전기동력 기반 추진시스템을 이용함에 따라 얻어지는 높은 설계 자유도에 의해 다양한 수직이착륙 항공기 형상, 비행 메커니즘을 가진다. 즉, 차세대 항공용 수직이착륙 항공기를 설계하기 위해선 특정 컨셉에 국한되지 않는 범용성을 갖춰야 한다. 또한 도심을 비롯해 지역 거점 간 비행하기 때문에 회전익 시스템으로부터 발생하는 소음 또한 설계의 성능 지표로 활용되어야 한다.

한편, 현재 배터리 기술이 갖는 한계에 의해, 차세대 항공교통용 전기동력 수직이착륙 항공기는 도심 주변 비행 용도로 완전 전기추진방식을, 지역 거점 간 비행 용도로 하이브리드 전기추진방식을 채택하고 있다. 향후 배터리 기술이 충분히 발전한다면, 모든 차세대 항공교통용 수직이착륙 항공기는 탄소중립을 지키기 위해 완전 전기추진방식을 따를 것으로 예측되며, 이에 따라 개념설계 단계에서부터 모터의 위상각 제어, 배터리 전압 강하와 같은 전기적 특성을 고려할 수 있는 모델링에 대한 필요성이 대두되고 있다.

본 연구에서는 차세대 항공교통용 전기동력 수직이착륙 항공기만의 특징들을 고려할 수 있는 범용적인 설계 기법을 제안하였다. 제시된 설계 기법은 항공기 형상, 비행 메커니즘 및 전기추진시스템의 다양성과 소음 예측을 포함한 성능 평가를 고려할 수 있는 5 개의 새로운 모듈(비행 분석, 추진 시스템 사이징, 임무 해석, 중량 추정, 소음 예측)로 구성된다. 먼저, 기존의 고정익 및 회전익 연구들에서 제시한 날개, 틸팅시스템, 덕티드 로터 및 분산추진장치등에 대한 해석 기법들을 하나의 비행 해석 모듈로 결합하여, 해석 대상의 범용성을 높였다. 또한, 추진 시스템 사이징, 임무 해석 및 중량 추정 대상의 범위를 완전 전기추진방식뿐만 아니라 하이브리드 전기추진방식(직렬, 병렬, 그리고 직병렬)까지 포함할 수 있도록 확장하였다. 그리고 음향상사식 Farassat 1A formulation 을 이용하여 특정 고도에서의 두께 및 하중 소음을 예측할 수 있도록 하였다.

또한 본 연구에서는 완전 전기추진방식을 이루는 각 전기장치(전기모터, 인버터, 배터리)의 전기적 특성을 보다 정확하게 고려할 수 있는 새로운 전기추진시스템 모델링 방법을 제안한다. 제시된 전기추진시스템 모델링 방법은 영구자석 전기모터의 MTPA (Maximum Torque Per Ampere) 제어 전략이 접목된 등가회로 모델, 인버터의 스위칭 및 전도 손실 모델, 상용 배터리 방전 그래프의 선형화 모델 등으로 구성된다. 그리고 모터 및 인버터 매개변수에 대한 회귀 모델을 추가적으로 구축하여, 새로운 전기추진시스템 모델링 방법을 개념 설계 기법에 적용 가능하게 하였다.

차세대 항공교통용 전기동력 수직이착륙 항공기 개념 설계를 위해, 본 연구에서 제안된 수치 기법들의 필요성과 기능을 입증하기 위해 세 가지 유형의 응용 연구를 수행하였다. 첫 번째 응용 연구는 완전 전기추진방식과 하이브리드 전기추진방식과의 비교 연구로, 최적의 하이브리드화 비율을 구현한다면 비행 거리를 완전 전기추진방식 대비 3 배 가량 확장시킬 수 있음을 보였다. 두 번째 응용 연구는 전기추진시스템 모델링 방법 간의 차이점과 완전 전기추진방식의 모터 구동 시스템(직접 혹은 간접) 및 기어비의 변화가 전기추진시스템의 효율 및 사이즈에 미치는 영향을 확인하였다. 마지막 응용 연구로, 소음 저감이라는 설계 요구조건이 전기동력 수직이착륙 항공기 설계에 미치는 영향에 대해 알아보았으며, 소음과 항공기 총 중량은 서로 명확한 반비례 관계를 가지는 것을 확인하였다.

주요어: 차세대 항공교통, 전기동력 수직이착륙 항공기, 항공기 개념설계, 전기동력장치 해석, 설계 최적화

학번: 2019-34016

성명: 이동욱